Western University
Scholarship@Western

Digitized Theses | Digitized Special Collections

1973

Solar Surges: Magnetic Properties, Dynamics And Structure

Jean-rene Roy

Follow this and additional works at: https://ir.lib.uwo.ca/digitizedtheses

Recommended Citation
Roy, Jean-rene, "Solar Surges: Magnetic Properties, Dynamics And Structure" (1973). *Digitized Theses*. 651.
https://ir.lib.uwo.ca/digitizedtheses/651

This Dissertation is brought to you for free and open access by the Digitized Special Collections at Scholarship@Western. It has been accepted for inclusion in Digitized Theses by an authorized administrator of Scholarship@Western. For more information, please contact tadam@uwo.ca, wlswadmin@uwo.ca.

The author of this thesis has granted The University of Western Ontario a non-exclusive license to reproduce and distribute copies of this thesis to users of Western Libraries. Copyright remains with the author.

Electronic theses and dissertations available in The University of Western Ontario's institutional repository (Scholarship@Western) are solely for the purpose of private study and research. They may not be copied or reproduced, except as permitted by copyright laws, without written authority of the copyright owner. Any commercial use or publication is strictly prohibited.

The original copyright license attesting to these terms and signed by the author of this thesis may be found in the original print version of the thesis, held by Western Libraries.

The thesis approval page signed by the examining committee may also be found in the original print version of the thesis held in Western Libraries.

Please contact Western Libraries for further information:
E-mail: libadmin@uwo.ca
Telephone: (519) 661-2111 Ext. 84796
Web site: http://www.lib.uwo.ca/

SOLAR SURGES:
MAGNETIC PROPERTIES, DYNAMICS AND STRUCTURE

by

Jean-René Roy

Department of Astronomy

Submitted in partial fulfillment
of the requirements for the degree of
Doctor of Philosophy

Faculty of Graduate Studies
The University of Western Ontario
London Canada

February 1973

© J.-René Roy 1973

ABSTRACT

This investigation is an attempt to determine the conditions under which sporadic mass ejections, called solar surges, occur in sunspot regions of the solar atmosphere. High resolution (~0.3 arcsec) on- and off-band Hα filtergrams (passband of $\frac{1}{4}$ Å) of disk solar surges obtained with the Vacuum Tower Telescope of Sacramento Peak Observatory have been compared to magnetic data. The main results are:

1. Of 182 surges observed in eight active centers over 16 different days, 171 extend from Ellerman bombs or clusters of bombs with sizes of a few hundreds to 5000 km. The surge appears within minutes of the bomb brightness maximum, and follows the bomb evolution in a way suggesting that its material is squeezed out from the bomb. Eleven surges originate at the bright kernels of flares or subflares.
2. Surges constitute clusters of very fine dark (sometimes bright) filaments about one arcsec or less connecting to Ellerman bomb brightenings.
3. One hundred seventy-eight Ellerman bombs were identified and studied in one region near disk center (Mt Wilson 18468) and another near the east limb (Mt Wilson 18522). The mean durations of bombs at Hα-2 Å were about 13 min near disk center and 11 min near the limb; these times increase slightly when we observe closer to the core of

Hα. Eighty-six percent of the bombs in the near-limb region and 56% in the disk-center region were seen to be accompanied by ejections of dark material; the ejections were 3-30 arcsec long. The ejection length appears to be proportional to bomb size times bomb lifetime: 34 sets of observations in MW 18522 gave a significant coefficient of correlation of 0.35, consistent with the model suggested in 1.

4. Analysis of bomb activity along the edge of the light bridge in MW 18511 did not reveal systematic displacement with time of the area producing the bombs.

5. Surges tend to occur very near the boundaries of photospheric magnetic field concentrations; within 7 arcsec of penumbra-photosphere boundaries, within 3 arcsec of the edges of pores, within 5 arcsec of photospheric bright network and along light bridge.

6. Although spot groups of magnetic class βγ constitute only 3% of all sunspots, 38% of the 16 surge producing regions were βγ.

7. In two cases where the magnetic maps of the longitudinal field reveal a satellite polarity, the surge-generating bomb lies over it; in one other case, it is within 10 arcsec.

8. The presence of a visible satellite spot is not necessary for surges to occur. Many satellites remain without bomb and surge activity.

9. A more essential condition is that the satellite polarity evolves. Three surge producing regions with evolving magnetic flux were characterized by dimensions of the order

of 10^4 km and flux changes by a factor of 10 over a period of less than 24 hours. The average change rate of flux amounted to about 3×10^{15} Mx/s. A fourth region showed drastic change in the size of pores located within four arcsec of the surge base.

10. When one evaluates the emf arising from such a flux change rate, the obtained value of 10^7 volts is not sufficient to give rise to any proton event at one A.U., if one accepts the criterion given by Zvereva and Severny (1970).

11. The trajectories of surge threads above 5000 km are matched by magnetic lines of force calculated in the current-free approximation. Local currents may be present, but must have a very small effect on the field geometry.

12. Velocities of four surges with well-known geometry show an initial accelerating phase up to 10 000-30 000 km above the surface, followed by a deceleration phase and return. The deceleration is faster than if gravity alone is acting; during the falling back phase, the surge velocity is less than free-fall. A force, possibly of electromagnetic nature, opposing the motion is at work.

13. Theoretical models explaining the Ellerman bomb based on the existence of a neutral point in the magnetic configuration of evolving satellite polarity have an observational basis. Dynamic dissipation of magnetic energy in the vicinity of a neutral magnetic line proposed

by Syrovatsky (1966, 1970) appears as the model most consistent with observations. The behavior of surge velocity as a function of height favors the model of diamagnetic ejection for the acceleration of surge material (Livshits and Pikel'ner, 1964). A model including both the energy source and plasma flow at a magnetic neutral line followed by diamagnetic acceleration after ejection from the Ellerman bomb area appears the best approach to explain fully the bomb-surge phenomenon.

Livshits, M. A. and Pikel'ner, S. B.: 1964, Sov. Astron. AJ 8, 368

Syrovatsky, S. I.: 1966, Sov. Astron. AJ 10, 270

Syrovatsky, S. I.: 1970, in Dyer (ed.), 'Solar Terrestrial Physics', p. 119

Zvereva, A. M. and Severny, A. B.: 1970, Izv. Krymsk. Astrofiz. Obs. 41-42, 97

ACKNOWLEDGEMENTS

The results reported in this thesis are due in large part to the generous assistance and support by many people.

Dr. David M. Rust of Sacramento Peak Observatory suggested the topic. His patience as well as his numerous comments and suggestions were most helpful. His guidance throughout the many phases of this exploratory study kept me close to the critical aspects of the main problem amidst a prodigious quantity of good data.

I am grateful to Dr. John W. Evans for kindly inviting me at Sacramento Peak Observatory, and at the same time, providing me with generous financial assistance. His warm hospitality during six months made my stay in New Mexico most enjoyable. Thanks to Dr. Jacques M. Beckers for putting great care in providing me with all the observing time I needed.

The Québec-Ontario Permanent Commission and the National Research Council of Canada provided also financial aid in the form of fellowship and scholarship.

Observers and technicians at Sacramento Peak Observatory who assisted me were: H. Mauter, R. Mann, F. Hegwer, T. Bauer, L. Dickson, L. Gilliam, E. Coleman, E. Johansen and W. Davis. The careful photographic work of R. Faller

in reducing some of the 35 mm originals into cinematographic 16 mm copies and accomplishing a large amount of printing is appreciated. The magnetograms were obtained with the Doppler-Zeeman Analyzer at Sac Peak by Dr. Rust and by Ramesh Sinha (U of Maryland).

I completed my observing material with some of the excellent filtergrams of Dr. R. B. Dunn and Mr. L. B. Gilliam of Sacramento Peak. Mr. J. M. Adkins of Hale Observatories supplied me with many Mt Wilson sunspot drawings and large scale magnetograms.

Several people provided enlighting discussions and comments on many aspects raised in this thesis. Thanks are especially due to Drs. H. U. Schmidt (Max-Planck-Institut für Physik und Astrophysik, Munich), R. B. Dunn (Sacramento Peak Obs.), C. L. Hyder (U of New Mexico), W. Wagner (Sacramento Peak Obs.), R. Canfield (Sacramento Peak Obs.), J. B. Zirker (U of Hawai), T. Hirayama (Tokyo Astronomical Obs.) and Y. Uchida (Tokyo Astronomical Obs.).

Mr. H. Leparskas (U of Western Ontario) closely collaborated with me in analyzing some of the observations on Ellerman bombs. Drs. J. D. Landstreet, W. Wehlau and J. M. Marlborough (U of Western Ontario) kindly read the manuscript and helped to clarify many parts of the text. Dr. Joan Vorpahl (Sacramento City College) gave helpful comments on properties of Ellerman bombs.

TABLE OF CONTENTS

LIST OF TABLES

LIST OF FIGURES

CHAPTER I

INTRODUCTION

This dissertation describes an investigation of localized flows of material called solar surges, originating in solar active regions. Significant improvements in resolution and techniques of observation in the last decade, in particular the beginning of operation of the Sacramento Peak Vacuum Tower Telescope and use of the tunable Hα Zeiss monochromator, have allowed chromospheric features about 200 km in size to be resolved. Helped by these new aids, this investigation should bring more light onto the problem of interaction between dense plasmas and magnetic field and give some clue about the onset of magnetic instabilities in the solar atmosphere. The purpose of this work is essentially to establish the necessary conditions for surges to occur in solar active centers and outline a phenomenological model of the surge event.

1.1 PLAN OF THE DISSERTATION

Chapter I provides the basic observational and theoretical background on solar surges. Chapter II describes the instrumentation used to obtain the data: Vacuum Tower Telescope, birefringent filter and Doppler-

Zeeman Analyzer. Chapter III deals more directly with the observational procedure of obtaining on- and off-band Hα filtergrams and magnetic maps of specific active centers with surge activity; problems encountered in the data reduction are also surveyed in the same chapter. Chapter IV lists the solar active regions where the main surge events occured. Chapter V presents results about the surge magnetic environment. Chapter VI covers the aspect of the dynamics of surges. Finally, Chapter VII attempts a general interpretation of the bomb-surge phenomenon and singles out the theoretical model most consistent with the observations. Gaussian units are used throughout this dissertation.

1.2 AN OVERVIEW OF THE SURGE PHENOMENON

The problem of ejection of material in astrophysics has become a major research area lately. Except for the case of the solar wind, we can only guess about the nature of the mechanisms propelling significant portions of stellar surface plasma into space. The importance of steady flow relative to sporadic ejections is not known. Investigations of the solar chromosphere have brought us to realize that the whole solar surface is bubbling continuously and that jets of chromospheric material in the form of spicules are always present. Under favorable conditions such as low gravity and strong electromagnetic activity, ejective flows could be a major contributor to mass loss from stars.

The various mass motions above the photosphere are part of the general solar prominence activity. Falling material is observed in loop prominences, arch filaments, coronal

rain and quiescent prominences; whole prominences are hurled away three or four times a month as in the sudden eruption of quiescent prominences. Finally, an important class of ejections from the surface occurs. Different types of ejections occur in solar active regions and are distinguished in Table I. The spray and fast ejection are separated from the surge due to their much higher velocities indicating a more powerful generating process, the degeneration of their initial continuous shape into numerous clumps, and the small amount of descending material. An extensive review of mass motions in the solar atmosphere has been edited by Ohman (1968).

1.3 OBSERVATIONAL BACKGROUND

The main studies of surges are due to Newton (1942), Ellison (1949), Giovanelli and McCabe (1958), Gopasyuk *et al.* (1963), Bruzek (1969) and Westin (1969). Other studies dealing with phenomena related to surges, like Ellerman bombs (Ellerman, 1917) or moustaches have been done by McMath *et al.* (1960), Koval (1964, 1965a, b, 1967) and Severny and Koval (1961).

Conventionally, a surge is the straight or arch-shaped collimated streamer of material stretching out from a sunspot region; surges show as organized threads or knots of ejected gas and are often followed by an apparently gravity-induced return to the surface along the same trajectory. Surges (and sprays) as a class possess the highest velocities of all prominences, attaining several hundred km/s and even escape velocity. On the disk, surges (also termed

Table I

Types of ejections from solar active regions

	Surge	Spray	Fast ejection
Extent above surface	10^4-10^5 km	10^5-interplanetary medium	Interplanetary medium
Max. velocity	100-200 km/s	$>$ 600 km/s	$\sim$ 1500 km/s
Mass*	10^{14}-10^{16} g	10^{15}-10^{16} g	10^{15}-10^{16} g
Morphology	collimated, stream-like flow	spray like, turbulent	clouds of bright knots
Structure	fine threads (one arcsec) of dark material	clumps and knots of flare material a a few 10 000 km across	compact portions of the flare
Origin at surface	Ellerman bombs	flare	flare
Reference	Bruzek, 1969	Smith, 1968	Bruzek, 1969

(*) Those values rely on uncertain values for the density ranging from 10^{11} to 10^{13} cm^{-3}. Surge densities are simply not known. The only values have been proposed by Becker (1959), who claims to have found out surges as dark formations with 3 to 5% contrast in white light in the first 10 min. If the absorption is due to scattering on

free electrons, this would require $n_e \gtrsim 10^{13}$ cm^{-3}. Through an analysis of Balmer series, Teryava (1960) found a population for $n_2 \approx 2 \times 10^4$ cm^{-3}, which, if one assumes equilibrium and use Boltzman formula (T = 6000 K) leads to $n_1 = n_H = 10^{12}$ cm^{-3}. The fact that E. Coleman (1971, unpublished) of Sacramento Peak Observatory succeeded in recording a surge on the limb in the continuum light points to the possibility of rather high density in surges.

'active dark flocculi'), appear in general dark; at their initial stage, close to the bright Ellerman bomb at the base, they may appear bright in Hα. At limb, the surge is bright; typical features are of high intensity and narrow shape and move rapidly outward from the solar surface, and later reverse their direction or fade away. Surges have been classified by importance, based on their apparent length as shown in Table II.

Table II

Sizes of solar surges

Importance	Apparent length	
	$R_\odot$	km (x 10^3)
S	5%	35
1	5-10%	35-70
2	10-20%	70-140
3	20-40%	140-280
3^+	40%	280

The spike of material tends to grow out rapidly from a small roundish luminous knot, or Ellerman bomb, with a diameter of a few seconds of arc having flare brightness (1 sec of arc $\approx$ 725 km). The spectrum of bombs is characterized by very thin and elongated emission wings emerging from normal Fraunhofer lines. The phenomenon apparently takes place in the low chromosphere at depths in the range $0 \lesssim \tau_0 \lesssim 0.4$ (Severny, 1964; Bruzek, 1972). Bomb and flare light curves are similar, with Ellerman bombs resembling the bright kernels of well developed flares seen in off-

band Hα films (Severny, 1968). These knots, whose spectral properties have been investigated by Koval and Severny (Koval, 1964 and 1965; Koval and Severny, 1970; Severny, 1956, 1964 and 1968) and by Bruzek (1972) form the base, possibly even the source of the surge (Bruzek, 1969). As we will see in chapter V, those bombs generally appear quite close to large sunspots (generally at the edge of the penumbra) a few minutes before the surge becomes visible. Apart from the bomb brightening at its base, the surge is rather independent of the flare. Because almost all flares have surges associated with them, there may be some cases of related events; if contemporary to a flare, the surge may occur before, during or after the 'main' flare.

Surges originate in region of sunspots, i.e. in places with strong magnetic field, and flow out from the spots in a radial direction. Harvey (1969) has observed that magnetic field intensities in limb surges range between a few to 150 G. Surges present a general appearance of being channeled and contained by the field. The fact that the highest surges contain the weakest fields (Harvey, 1969) emphasizes that they are probably under magnetic control. Harvey found also that surges with large line-of-sight velocities tend to show weaker field strengths than surges with small line-of-sight velocities. Low importance surges have a strong recurrence tendency on a time scale of about one hour or less (Bruzek, 1969).

The optical spectrum of surges resembles the flare spectrum rather than the spectrum of normal prominences

(Tandberg-Hanssen, 1963). The emission fades rapidly with height as to be expected if material is shot up from the chromosphere and derives its energy from below. The co-existence of low excitation emission lines and coronal lines in surges (Tandberg-Hanssen, 1959) indicates that physical conditions are very inhomogeneous; therefore, quantities such as $\overset{\text{mean}}{\wedge}$ temperature and density have limited meaning. Moreover, the presence of a magnetic field in surges can be expected to introduce significant anisotropies. Although complex temperature regimes exist in surges (Tandberg-Hanssen 1963), the electron temperature is assumed to be around 10^4 K. The fading of emission features indicates that the surge is 'less active' in its upper part than at its base, as if the plasma relaxed after being shot out (Tandberg-Hanssen, 1967).

Kirshner and Noyes (1971) have observed a surge at the limb in CIII 977 Å with the Harvard OSO-6 spectroheliograph. The kinematic behavior of the surge is the same in CIII as in Hα. The amount of CIII emission is consistent with a model in which the CIII ions occupy sheets with thickness of about 100 km surrounding the cooler Hα emitting threads. The surge remained visible in the CIII records long after it disappeared entirely from the Hα film.

Type II and III radio bursts are more likely (by a factor of two) to occur if the associated flare is accompanied by a surge (Swarup et al., 1960). This suggests that the explosion responsible for the surge may generate the much

faster disturbance which produces the radio bursts (Swarup et al., 1960; Malville, 1962; McCabe, 1971; Martres et al., 1972). There are a few occurences where soft X-ray emission has been correlated in time with the appearance of surges on the sun (Kleczek and Krivsky, 1960; Westin, 1969; Teske, 1971). However, because of poor resolution, the association of X-rays with bomb-surge events has not yet been demonstrated. More definite results should come out from W. Neupert experiment aboard the OSO-7; it provides X-ray observations in the wavelength ranges of 1.8-7 Å and 8.3-15 Å with a resolution of 20".

1.4 THEORETICAL BACKGROUND

1.4.1 PHYSICAL STATE OF THE SURGE MATERIAL

The physics of solar prominences in general is poorly known; results of theoretical considerations are subject to much discussion still (Tandberg-Hanssen, 1967; Harvey, 1969; Poland and Anzer, 1971; the Capri Symposium reviewed by Bruzek and Kuperus, 1972; Noyes et al., 1972).

1.4.2 THEORIES OF SURGES

The close association between Ellerman bombs and surges was not known to be so universal before this investigation. Therefore, models attempting to explain surges ignored the energy source of the bomb and theoretical investigation dealt mainly with the acceleration mechanism.

The Ellerman bomb, found at the initial phase of a surge, is the manifestation of sudden energy release presenting many of the properties of solar flares (which are 10^4 to 10^6 times more powerful); however, there is no reason to equate

Ellerman bombs and flare kernels seen in off-band Hα films. It is helpful to keep in mind the mechanisms of energy dissipation used to explain flares and investigate their relevance to bomb-surge events; models aimed at explaining flares generally consider material ejection only as a secondary effect or not at all. To explain the sudden energy release of flares or bombs, many processes have been proposed which use the sudden transformation of electromagnetic energy into thermal and mechanical energy of the gas; see Parker (1963), Sweet (1969), Schmidt (1969) and Syrovatsky (1970) for reviews of the theoretical aspects and applications to flares.

In attacking the surge phenomenon, two aspects should be considered: (1) Because the velocity of surges increases with height, acceleration out of the solar surface is required; a few models have been proposed and will be considered in the next paragraphs. (2) The origin and possibly the source of the surge material at the Ellerman bomb has to be accounted for and the energy release in the bomb explained; models must be borrowed from the flare mechanisms and will be discussed in Chapter VII. A full theoretical approach describing the whole bomb-surge event is non-existent at present.

Before venturing into the description of the models of surge acceleration, I shall describe a crucial aspect of magnetic field configurations present in the solar atmosphere and fundamental to many dissipative processes. This is the magnetic neutral line (or point) configuration illustrated in Figure 1.1 in Chapter I. Neutral lines or

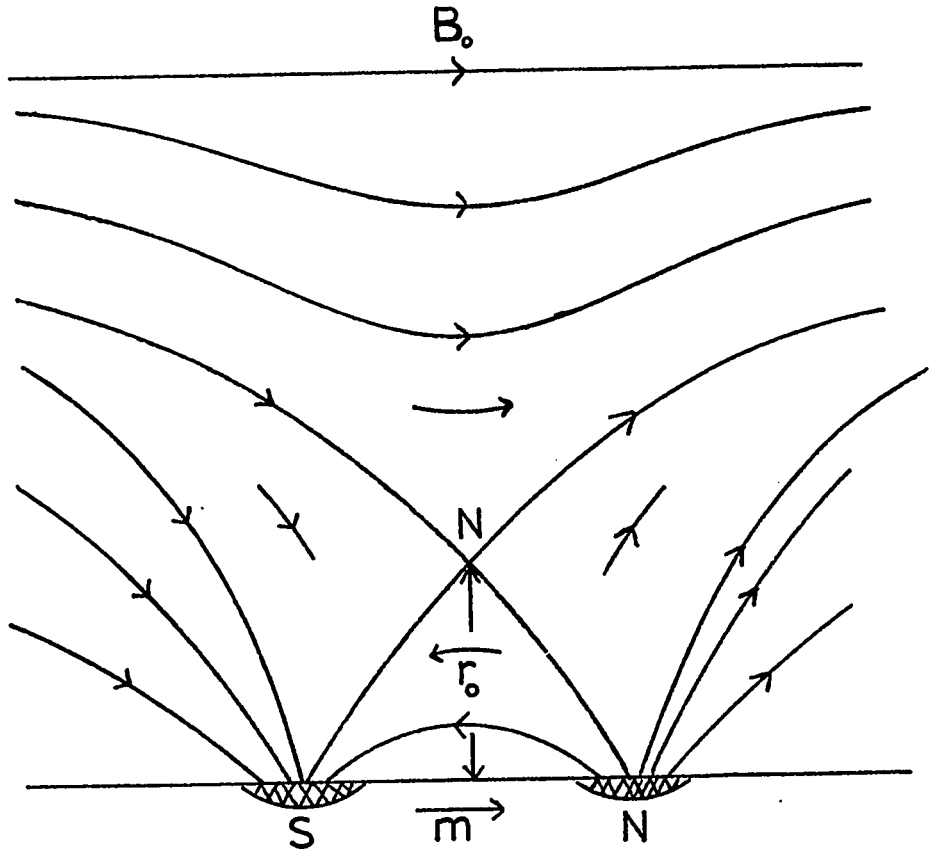

Figure 1.1 Neutral points (or lines) in the solar atmosphere originate from the superposition on the general solar magnetic field of the bipolar field of a newly emerged group having a magnetic moment m. The same situation arises when a small group emerges near the dominant parent polarity in an active center (satellite polarity or polarity reversal). Velocity fields in the photosphere can convect the fieldlines of opposite field and provide also the configuration. At N, B = 0; this is called a neutral X-type point (or simply neutral point) or hyperbolic null point.

points may originate from the superposition of the bipolar field of a sunspot group on the general solar magnetic field, or from the small polarity reversals found around the strong poles of sunspot groups. These polarity reversals, called 'satellite spots' by Rust (1968), present a polarity opposite to the one of the nearest parent spot.

The significance of neutral lines can be illustrated by Ohm's law for a moving plasma, which we consider for simplicity to be isotropic:

$$\underset{\sim}{j} = \sigma(\underset{\sim}{E} + \frac{1}{c}[\underset{\sim}{v} \times \underset{\sim}{B}]) \qquad 1.1^{*}.$$

Here σ is the plasma conductivity, $\underset{\sim}{E}$ and $\underset{\sim}{B}$ are the electric and magnetic fields in the laboratory frame, $\underset{\sim}{j}$ is the current density, and $\underset{\sim}{v}$ the bulk velocity of the plasma. It is seen from eq. 1.1 that because of the high conductivity ($\sigma \to \infty$) of the plasma, an electric field simply produces a drift motion of the plasma with drift velocity $v = c(E \times B)/B^2$. This is true everywhere except in the vicinity of the point where $B = 0$. At that location, the electric field cannot be balanced by the induction and produces a strong current in the plasma.

If fields with opposite polarities are brought into closer contact, by moving photospheric material (Sweet, 1958; Parker, 1963; Petschek, 1964) or by magnetic buoyancy forces (Syrovatsky, 1966, 1969), their annihilation and reconnection

---

* The distinction between $\underset{\sim}{B}$ and $\underset{\sim}{H}$ disappears for a non magnetic medium; for material other than ferromagnetic substances, μ differs from unity by only a few parts in 100 000.

at the neutral point are enhanced. This enhancement is further helped by the recession of the reconnected field out of the zone through Petschek's mechanism (Petschek, 1964) which describes how field dissipates at a neutral point. In Petschek's mechanism, when two oppositely directed fields are pressed together (Figure 1.2), resistive diffusion at the neutral point annihilates the horizontal component of the magnetic field and the fieldlines reconnect; each fieldline is bent sharply as it emerges from the diffusion region (Figure 1.3). The rearranged field geometry results in a disturbance which propagates as an Alfvén wave away from the X-neutral point. Reconnected fieldlines recede away from the diffusion region. The mechanism allows a source of energy due to dissipation at the neutral point and expulsion of material carried by the receding fieldlines.

We finally come to the description of models explaining the surge acceleration phase. The most detailed quantitative mechanism describing surge acceleration was proposed by Livshits and Pikel'ner (1964); they used diamagnetic ejection, often called 'melon-seed' mechanism. The model describes the evolution of a plasma condensation, identified as the surge, out of strong magnetic field typical of sunspot regions.

In a medium where large dimensions and appreciable conductivity prevail, the external field will penetrate slowly into the evolved surge plasma and the external and the

Figure 1.2. Two approaching oppositely directed fields as used in Parker's modification of the Sweet model. At the neutral point N, fieldlines are broken and reconnect. For an incompressible fluid, UL = Vl, where U is the speed at which material enters the region through L and V is the speed at which the fluid escapes through l.

Figure 1.3. Magnetic configuration of the Petschek dissipation wave mode. (a) magnetic fieldlines prior to the formation of standing waves in the Petschek flare model; diffusion is to predominate within the dashed rectangle. Resistive diffusion annihilates the horizontal component leading to the transition shown in (a) and (b). If the angle in Figure 1.2 is very small, one can regard the process as one that switches off the strong horizontal component of the field. A boundary layer is formed along the limiting line and the horizontal boundary of the diffusion region (standing wave-boundary-layer); one quadrant is shown in (c).

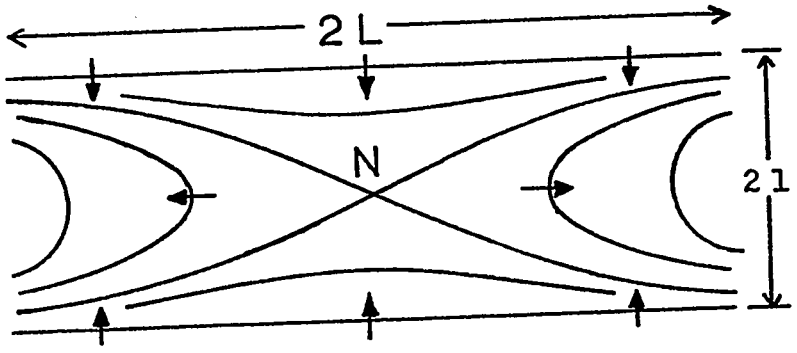

Figure 1.2

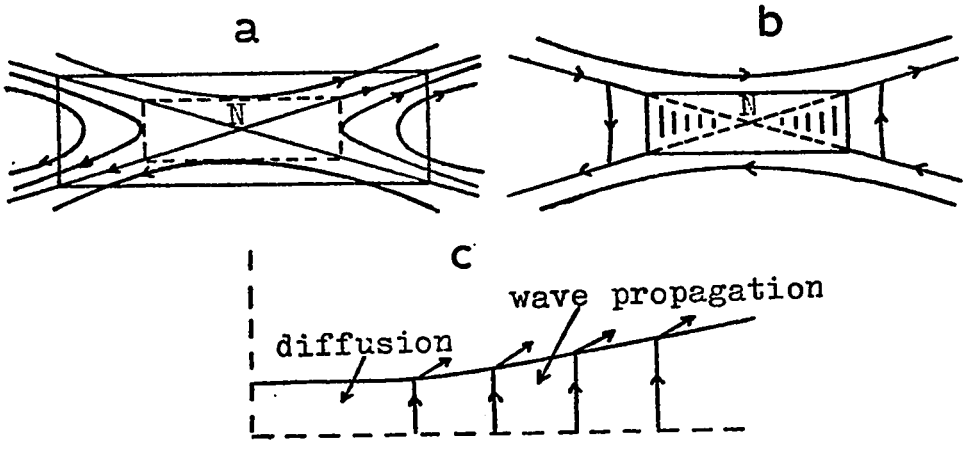

Figure 1.3

internal field will be non-interacting. An initial condensation originating in the strong spot field is created by the tangling of lines of force due to velocity fields in the photosphere where the fieldlines are anchored; dissipation, prominent at X-type neutral points, separates the condensation from the surrounding field. The assumption that the initial condensation forms near the photosphere explains the very high initial density ($\sim 10^{15}$ cm^{-3}). The density decreases by 3×10^3 to 10^4 times in the evolving condensation. Due to a more or less adiabatic expansion, the gas cools down. However, instead of dropping by 200 to 500 times, observation shows that the temperature stays about the same. The authors are unable to supply an efficient heating mechanism and have to assume that the observed heating may take place only in the skin of the surge. The presence of a condensation into which the field does not penetrate from outside will deform the lines of force of the external field. This gives rise to magnetic forces which strive to return the lines of force to their earlier position. If the external field is not uniform, then the resultant of the forces acting on all sides will not vanish, and the upshot will be that the condensation will be forced out of the region of high field strength.

Livshits and Pikel'ner consider the ejection of a condensation under the influence of the magnetic pressure gradient in a vertical jet at the solar surface. Their model predicts a velocity increasing with height for the

first few 10^4 km and then slowing down (Figure 1.4a, b).

In the same perspective, Uchida (1969) has proposed a model to explain the acceleration of chromospheric spicules which may be extended to surges (see also Pikel'ner, 1969). Spicules are small jets of chromospheric material appearing as small scale morphological and dynamical versions of surges. Uchida first points out that magnetically neutral lines and/or points, occur along the supergranulation boundaries, where spicules originate and where the magnetic field is convected by the supergranule. Dissipation and reconnection of the magnetic field occur at such neutral lines. The plasma with thus reconnected magnetic lines of force frozen in it is accelerated by the melon-seed effect in the existing strong gradient of the external field. The motion of such a jet initiated by Petschek's mechanism is followed in a vertical magnetic tube of varying cross-section at the solar surface. Uchida's model has been made relevant to surges following Rust's finding (Rust, 1968) of a case of recurrent surges and Ellerman bombs bursting out a region of a satellite spot. As we saw earlier, a satellite spot provides a magnetic configuration with a neutral point.

A more qualitative model considering possible configuration in sunspots which may result in mass ejections similar to surges was suggested by Gopasyuk (1964). Gopasyuk claims to have found a strong positive correlation between the occurence of surges and the velocity of rotation of the spot near which surges originate. He suggests that the

Figure 1.4. (a) Dependence of velocity of surges on height under isotropic expansion for $n_o = 5 \times 10^{15}$ (bottom curve), 3×10^{15} and 10^{15} cm^{-3}. The dashed curve is the empirical curve provided by observations of Newton (1942).

(b) Dependence of velocity of surges on height under the assumption of different expansion laws: for isotropic expansion and $n_o = 3 \times 10^{15}$ cm^{-3} (bottom curve), for a same initial density in expansion law $\rho \sim B^2$ and $\rho \sim B^{5/2}$. The dotted curve is for $n_o = 10^{16}$ cm^{-3} and $\rho \sim B^{5/2}$. Figures (a) and (b) were adapted from Livshits and Pikel'ner (1964).

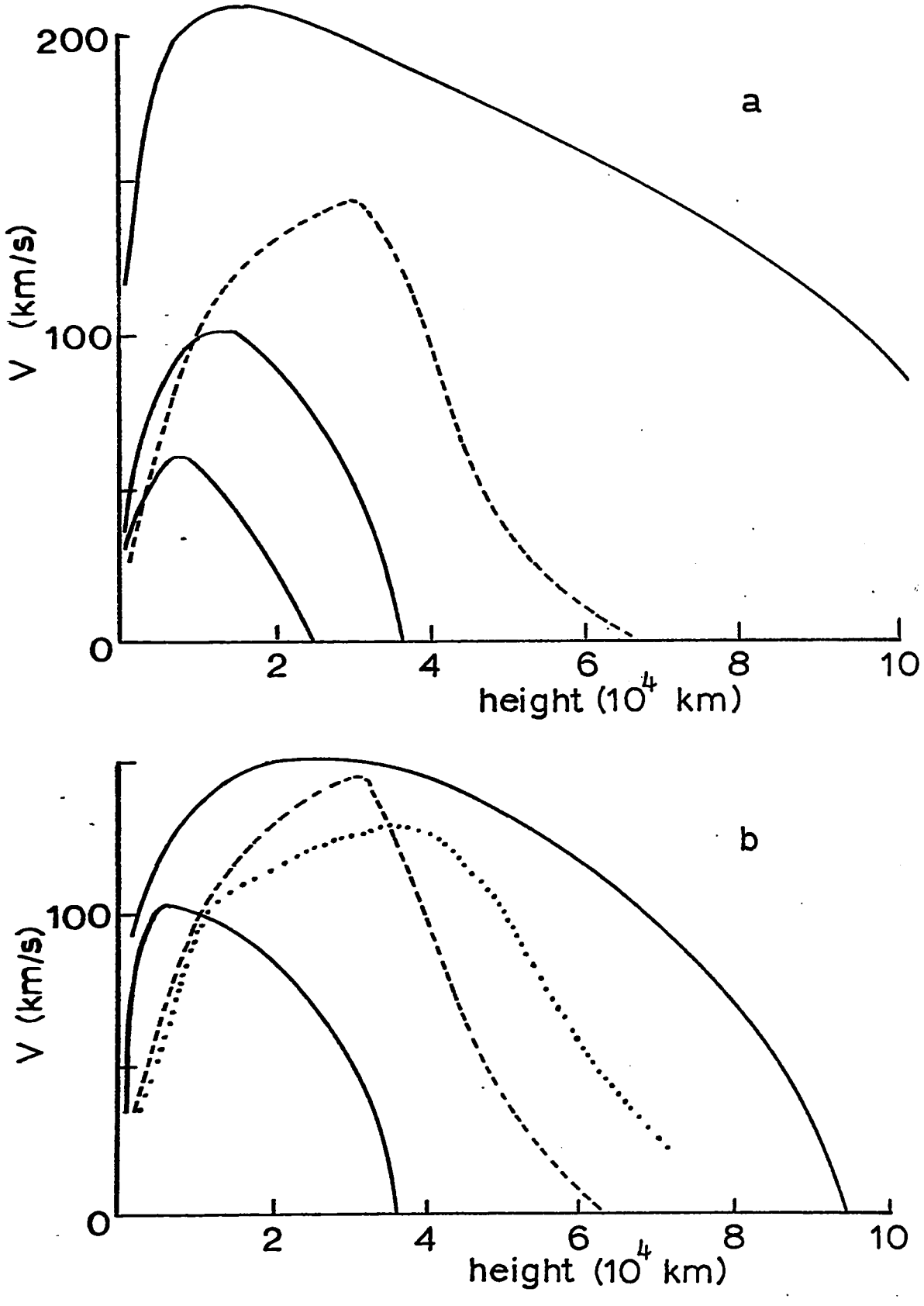
200
100
0
V (km/s)
a
2
4
6
8
10
height (10^4 km)
b
100
0
V (km/s)
2
4
6
8
10
height (10^4 km)

Figure 1.4

rotation of spots would lead to the twisting of magnetic field leading to a 'sausage instability'. The model remains silent about Ellerman bombs at the base of surges and does not predict the motion of the material. Furthermore, the amount of rotation of a sunspot is a very elusive quantity and can rarely be determined unambiguously.

Arguing against magnetic dissipation and reconnection for accelerating surges, Altschuler et al. (1968) suggested a non-linear mechanism for surges in which a plasma region of high electrical conductivity and macroscopic dimension can be rapidly accelerated without diffusion of magnetic field. For the purpose of numerical calculations, they replace the field near a polarity reversal by magnetic fields of current loops to reproduce the environment of surges originating at satellite spots. The relaxation of the magnetic field generated by two antiparallel coaxial current loops in a incompressible plasma is traced by computer. The results suggest that plasma in the form of a vortex ring can be expelled at the Alfvén velocity from sunspot regions. This model has been expanded further by Lilliequist et al. (1971). The model not only ignores the associated Ellerman bomb which is an essential part of the surge phenomenon , but also dismisses any dissipative process. It does not consider what happens to the current loops when the reversal of the motion takes place. Futhermore, the shape of the expelled plasma predicted by this theory is not supported by surge observations although ring-like vortices are sometimes seen at times of flares.

CHAPTER II

INSTRUMENTATION

2.1 THE SACRAMENTO PEAK OBSERVATORY

All the observations for this investigation were taken at the Sacramento Peak Observatory, located at Sunspot in southern New Mexico, 105° 19' W 32° 47' N, at an altitude of 2840 meters. Evans (1967) has given a description of the observatory. In this chapter, I will describe the instrumentation used to conduct my investigation.

2.1.1 THE VACUUM TOWER TELESCOPE

The Sacramento Peak Solar Vacuum Tower Telescope (Figure 2.1), designed by Richard B. Dunn, is a conglomerate of innovations adapted from space technology. The instrument has been described by Dunn (1964, 1969, 1971 a, b). I will limit myself to a basic description of the telescope, stressing the elements which account for the improvements over more conventional instruments.

The telescope is altazimuth in design. Figure 2.3 shows a cutaway of the overall structure. Image rotation is accomplished by rotating the inner tube structure together with all the auxiliary instruments. Azimuth and elevation torque motors drive the two mirrors at the top of the tower to track the sun automatically; the input to the servo is

Figure 2.1. Aerial view of the Sacramento Peak Solar Vacuum Tower Telescope; see Figure 2.3

Figure 2.2. The tunable Hα birefringent filter viewing system. The light port shows at the bottom center. To its left is the filter control unit. The Hα filter built by Zeiss shows above the exit port, about at the picture center; on top to the right is the 35 mm Acme camera. Hanging near the lower right corner is one of the hand-box through which commands are given to the computer.

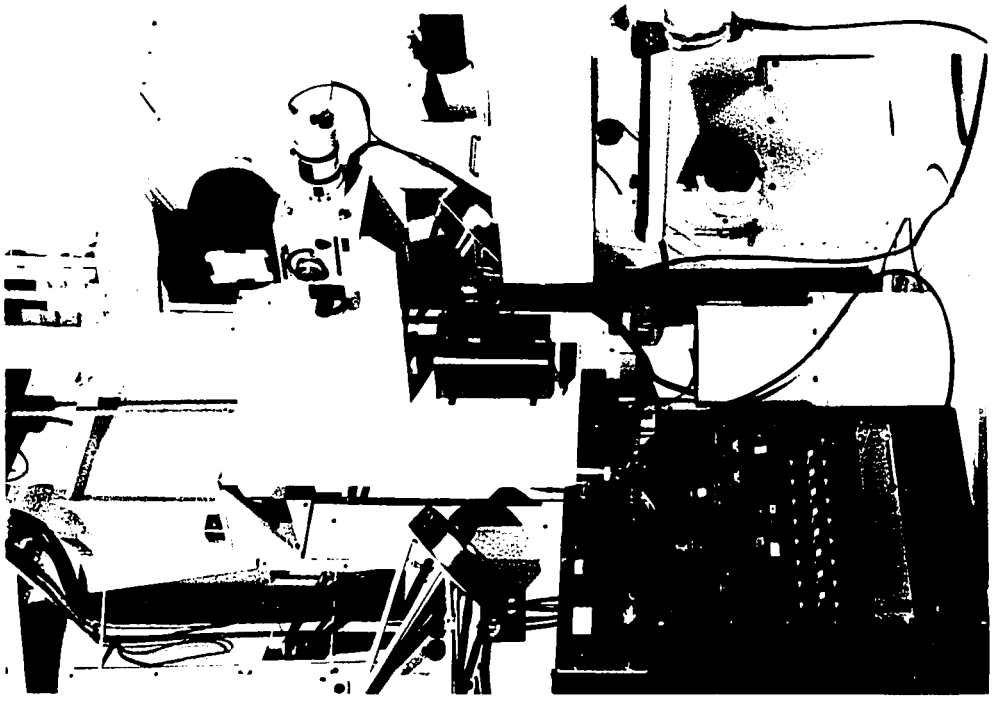

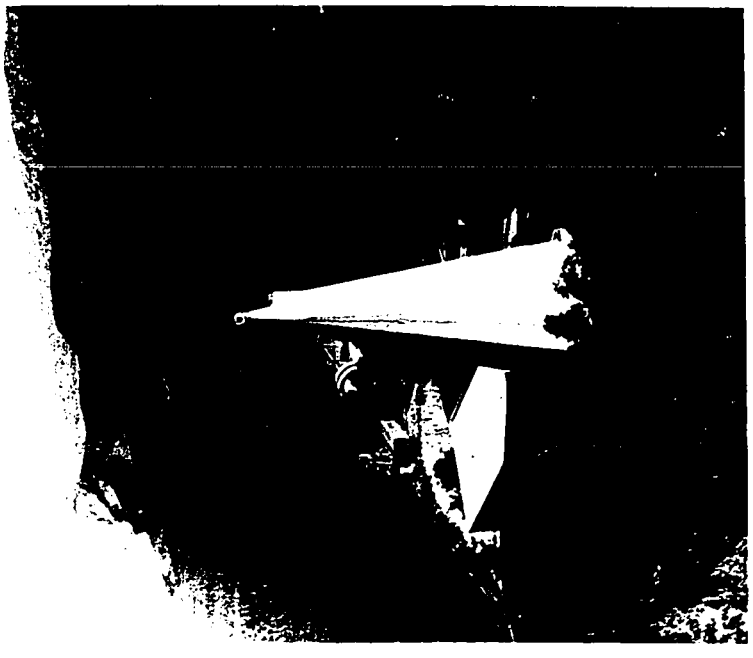

Figure 2.3. A cutaway of the telescope shows the light path from the 76-cm entrance window at top past the instrument table to the 163-cm primary mirror at the foot of the shaft. Sunlight is directed upward to anyone of the six viewing ports at ground level. The entire light path is in a vacuum chamber 98 m long at a pressure of 0.6 mm of mercury (equivalent to an altitude of 55 km above the earth's surface).

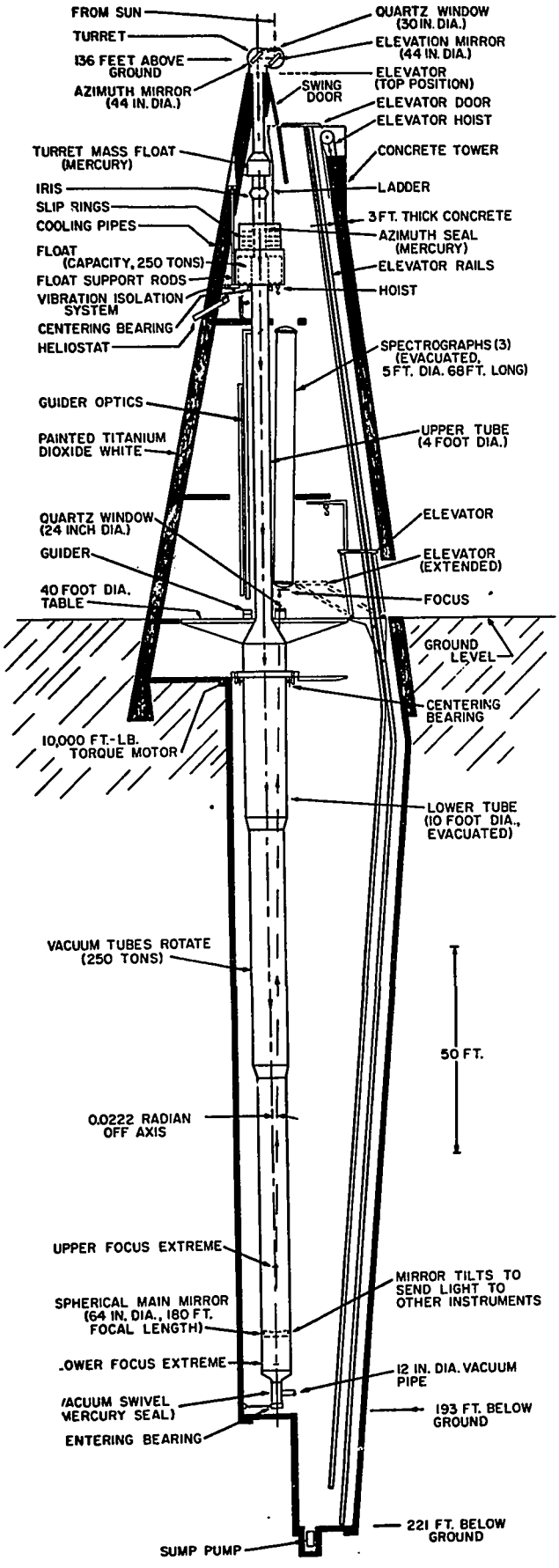
FROM SUN
TURRET
136 FEET ABOVE GROUND
AZIMUTH MIRROR (44 IN. DIA.)
QUARTZ WINDOW (30 IN. DIA.)
ELEVATION MIRROR (44 IN. DIA.)
ELEVATOR (TOP POSITION)
SWING DOOR
ELEVATOR DOOR
ELEVATOR HOIST
CONCRETE TOWER
TURRET MASS FLOAT (MERCURY)
IRIS
LADDER
SLIP RINGS
3 FT. THICK CONCRETE
COOLING PIPES
AZIMUTH SEAL (MERCURY)
FLOAT (CAPACITY, 250 TONS)
ELEVATOR RAILS
FLOAT SUPPORT RODS
HOIST
VIBRATION ISOLATION SYSTEM
CENTERING BEARING
HELIOSTAT
SPECTROGRAPHS (3) (EVACUATED, 5 FT. DIA. 68 FT. LONG)
GUIDER OPTICS
PAINTED TITANIUM DIOXIDE WHITE
UPPER TUBE (4 FOOT DIA.)
QUARTZ WINDOW (24 INCH DIA.)
ELEVATOR
GUIDER
ELEVATOR (EXTENDED)
40 FOOT DIA. TABLE
FOCUS
GROUND LEVEL
CENTERING BEARING
10,000 FT.-LB. TORQUE MOTOR
LOWER TUBE (10 FOOT DIA., EVACUATED)
VACUUM TUBES ROTATE (250 TONS)
50 FT.
0.0222 RADIAN OFF AXIS
UPPER FOCUS EXTREME
MIRROR TILTS TO SEND LIGHT TO OTHER INSTRUMENTS
SPHERICAL MAIN MIRROR (64 IN. DIA., 180 FT. FOCAL LENGTH)
LOWER FOCUS EXTREME
12 IN. DIA. VACUUM PIPE
VACUUM SWIVEL (MERCURY SEAL)
193 FT. BELOW GROUND
ENTERING BEARING
221 FT. BELOW GROUND
SUMP PUMP

derived from a photoelectric guider. When clouds intervene the servos are switched from the photoelectric guider to an electromechanical coordinate converter of right ascension and declination to azimuth and altitude, that also generates the signal for the rotation of the table.

Two flat mirrors are used to reflect the light vertically downward 96 m to a spherical primary mirror of 163 cm diameter and of 55 m focal length. A vertical instrument axis simplifies rotating auxiliary instruments to control image rotation. To eliminate internal seeing, the entire light path is kept under evacuated conditions equivalent to a pressure of 0.6 mm of mercury. The light is reflected back upwards to ground level by the primary mirror to form an image 51 cm in diameter 2.1 m above ground level. The theoretical resolution of the telescope is 0.2 sec of arc. Tilting the mirror 0.56 degree sends the light to one of several auxiliary instruments clustered around the six possible ports of exit for the light beam. The depth of focus is 0.76 cm; the primary can be focused 4.9 m up and 2.4 m down from its nominal position to accomodate small-aperture lenses placed in the exit window to change f ratios. The large size of the primary is necessary to obtain an unvignetted image of the entire solar disk.

Adequate cooling of the 76 cm aperture glass window has been one of the toughest problems to be solved by Dunn and his associates. Distortion of the window by heating of the sun was most serious near the supporting edges. The aperture

had to be diaphragmed down to 51 cm to avoid distortion of the image; this was the aperture I used most of the time (theoretical resolution $\approx 0.3''$), except for my observations in late October 1971 when I could use the full aperture. Circulating a cooled water-glycol mixture around the edge of the window and cell appears to have solved the heating-distortion problem (Dunn, 1971b).

An elaborate synchro system connects all the tracking servos together. Additional servos are required to tilt and focus the main mirror, to control the size of the iris diaphragm and to operate the devices on the main table. While at present, all the servos and the tracking are external to the telescope itself, the shutters, stepping motors, dark slides and similar actuators are operated through the computer.

2.1.2 THE NARROW-BAND BIREFRINGENT FILTER

The birefringent filter is a sharp-band monochromator for observing the sun in the light of a single line of the spectrum. The Hα monochromator in the Lyot-Ohman configuration (also known as a Lyot filter) is designed for observing the sun in the light of the red line of hydrogen at 6562.8 Å. With the exception of a narrow band with half-width of $\frac{1}{4}$ or $\frac{1}{2}$ Å, the entire solar spectrum is absorbed by polarization and interference of the incident solar light.

2.1.2.1 THEORY

The principle of this filter has been discussed by Lyot (1944) and Evans (1949, 1953). The Lyot filter takes

advantage of the birefringence of quartz, calcite and similar materials. If polarized light is passed through a quartz crystal with the optical axis of the crystal parallel to the face and at 45^{o} to the polarizer axis, it is split into two rays, the ordinary and the extraordinary. Because of the difference in the rate of propagation of the ordinary and extraordinary waves in the birefringent medium, rotation occurs. The transmission of an element b_k of thickness d_k, mounted between polarizers is a function of wavelength only; for parallel polarizers, it is

$$t_k = \cos^2 \pi n_k \qquad 2.1,$$

where n_k is the order of interference or the retardation in wavelengths, given by

$$n_k = \frac{d_k}{\lambda} (\epsilon - \omega) \qquad 2.2.$$

Here ϵ and ω are respectively the extraoridnary and ordinary refractive indices of the birefringent material. Thus the quartz rotates the plane of polarization by an amount proportional to its thickness divided by the wavelength, so as a function of wavelength the system alternately transmits and absorbs light.

In a typical design, polaroids are sandwiched between elements whose thickness increases by powers of two, i.e.

$$d_k = 2^{k-1} d_1 \qquad 2.3.$$

Therefore, the transmission curve of an assembled filter of k elements is

$$T = \cos^2 \pi n_1 \cos^2 2\pi n_1 \ldots \cos^2 2^{k-1} \pi n_1 \qquad 2.4.$$

The characteristics of T as a function of λ are exhibited

in Figure 2.4 for a simple 3 element sandwich. Curves a, b and d, represent the transmission of the third, second and first element individually. Curve e is the transmission of the three combined. The transmission curve for the whole filter consists of widely separated narrow transmission bands, the effective widths of which are the half width of the maxima due to the thickest element alone (curve d).

It is obvious that the usefulness of the birefringent filter is enormously enhanced if a transmission maximum can be adjusted to center on any desired wavelength or can be tuned continuously off-Hα by many Angstroms in order to capture the Doppler-shifted Hα profile of moving material. This can be accomplished by rotating polarizers in relation to quarter-wave plates about the optical axis. Following Evans (1949), let us consider first an element of a simple filter (Figure 2.5). Suppose the kth calcite or quartz element oriented with its γ-axis (axis of greatest principal index of refraction of a uniaxial crystal) along the x direction, is followed by a quarter-wave plate with its γ-axis along the r direction. By proper arrangement, we can have the vibration emerging from the quarter-wave plate reduced to a linear vibration at an angle of πn to the r-direction. We can omit the second quarter-wave plate and let the light enter a polarizer with its plane of polarization at angle ρ to the r-axis. The transmission of the assembly becomes

$$t = \cos^2 (\pi n - \rho) \qquad 2.5.$$

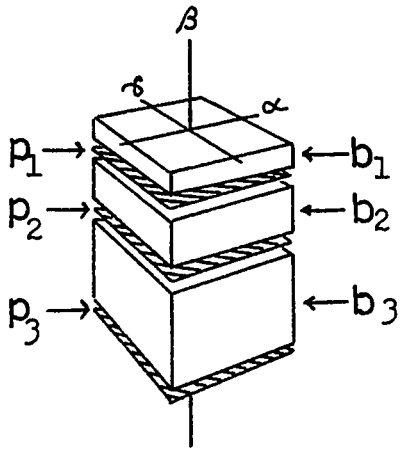

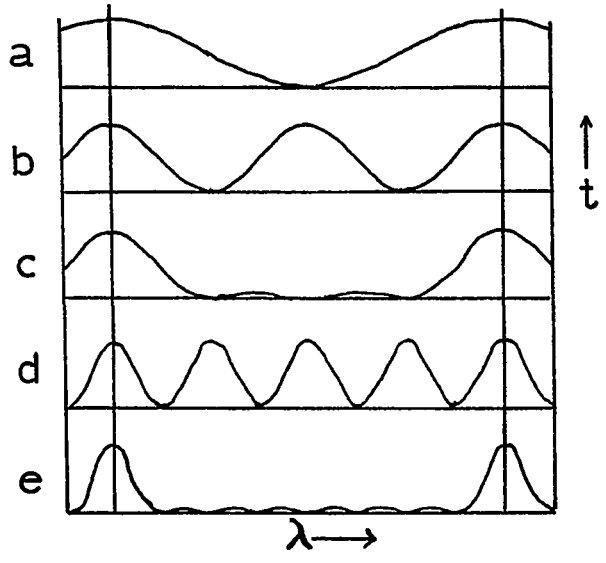

Figure 2.4. (i) Birefringent filter of three elements; a polarizer must precede the elements. (ii) Transmission curves of elements of (i): curve a is for the thinest element, and b and d are for elements two and four times as thick respectively. Curves c and e shows the combined effect of a-b and a-b-d respectively. (After Evans, 1949)

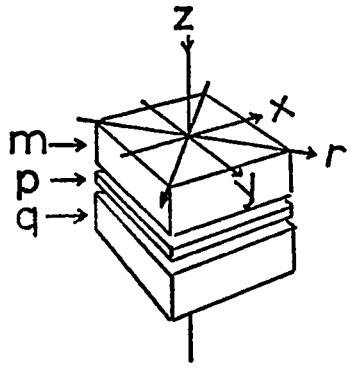

Figure 2.5. Birefringent components of a single unit of a split element filter. (After Evans, 1949)

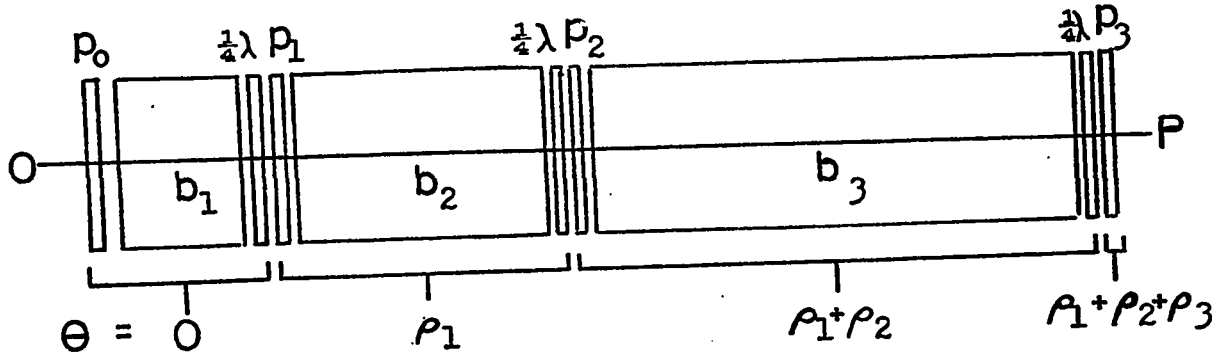

p - polarizer

$\frac{1}{4}\lambda$ - quarter wave plate

θ - position angle of unit about axis

Figure 2.6. Simple filter of three elements with quarter wave plate phase shifters. (After Evans, 1949)

By adjusting ρ (i.e. by rotating the polarizer) until $n_\lambda - \rho = \pi$ an integer, we can set t = 1 for any chosen wavelength.

An adjustable simple birefringent filter consists then of a series of units shown in Figure 2.6, each composed of a polarizer, a birefringent element with its γ-axis at 45° to the axis of the polarizer and a calcite. The three parts of each unit remain fixed with respect to each other, but the unit itself must be rotatable around the instrumental axis. The angle ρ_r is then the angle between the γ-axis of the rth quarter-wave plate and axis of the immediately following polarizer. The birefringent elements have the same thickness as the non-adjustable filter. The transmission of the whole is

$$T = \cos^2(\pi n_1 - \rho_1)\ \cos^2(\pi 2n_1 - \rho_2) \ldots\ \cos^2(\pi 2^{k-1} n_1 - \rho_k) \qquad 2.6,$$

$$\text{where } \rho_k = 2^{r-1}\rho_1.$$

Since the values of ρ are proportional to the powers of 2, it is a relatively simple matter to devise a gear train by which the wavelength of the transmission band can be adjusted with a single control knob.

2.1.2.2 THE CARL ZEISS POLARIZATION INTERFERENCE Hα FILTER

The birefringent filter I used was built by the German firm Carl Zeiss. A description of the apparatus was given by Haase and Gaenswein (1967). Figure 2.7 gives a cross-section of the filter and Table III lists the details of the optical system of the filter. The system of 8 elements results in an effective bandwidth (half-width) of $\frac{1}{4}$ Å.

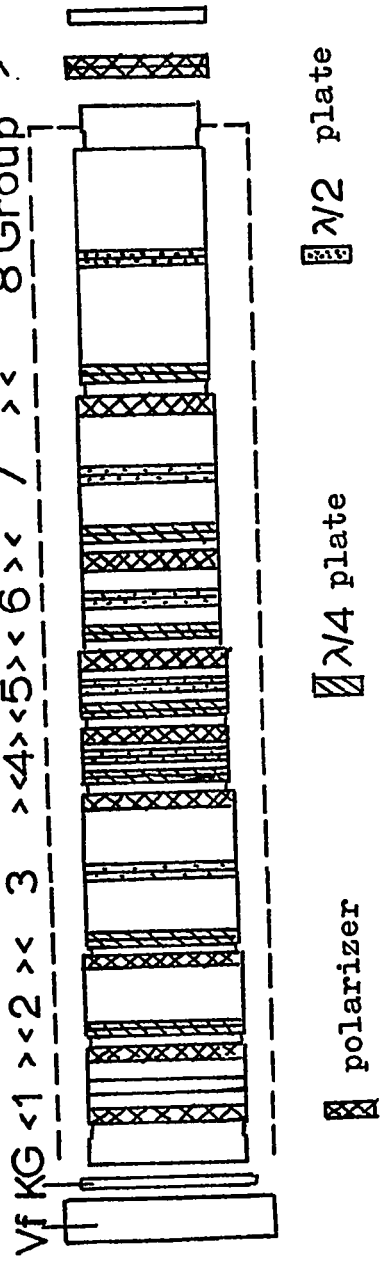

Figure 2.7. Optical design of the Hα monochromator; see also Table III.

Table III

Optical design of the H-alpha monochromator

Unit	Composition and type of crystal	Blank thickness of crystals (mm)	Orientation within line center of H-alpha	Half width in Å	Angle of rotation α during line shift
1. Unit	Polarizer		0°		
	Quartz	3.5	45°		
	Quartz	3.5	0°	32 Å	1 α
	Quartz	3.5	135°		
	Polarizer		90°		
2. Unit	2 quartz plates	$\lambda/4$	90°		
	Quartz	14	45°	16 Å	2 α
	Polarizer		90°		
3. Unit	2 quartz plates	$\lambda/4$	90°		
	Quartz	14	135°		
	2 quartz plates	$\lambda/2$	0°	8 Å	4 α
	Quartz	14	45°		
	Polarizer		90°		
4. Unit	2 quartz plates	$\lambda/4$	90°		
	Calcite	1.5	135°		
	2 quartz plates	$\lambda/2$	0°	4 Å	8 α
	Calcite	1.5	45°		
	Polarizer		90°		
5. Unit	2 quartz plates	$\lambda/4$	90°		
	Calcite	3.0	135°		
	2 quartz plates	$\lambda/2$	0°	2 Å	16 α
	Calcite	3.0	45°		
	Polarizer		90°		
6. Unit	2 quartz plates	$\lambda/4$	90°		
	Calcite	6.0	135°		
	2 quartz plates	$\lambda/2$	0°	1 Å	32 α
	Calcite	6.0	45°		
	Polarizer		90°		
7. Unit	2 quartz plates	$\lambda/4$	90°		
	Calcite	12.0	135°		
	2 quartz plates	$\lambda/2$	0°	0.5 Å	64 α
	Calcite	12.0	45°		
	Polarizer		90°		
8. Unit	2 quartz plates	$\lambda/4$	90°		
	Calcite	24.0	135°		
	2 quartz plates	$\lambda/2$	0°	0.25 Å	-
	Calcite	24.0	45°		
	Polarizer		90°		not rotatable

The first crystal unit of the filter (as seen in the direction of the light beam, from left to right) is composed of three thin quartz plates (Table III). These are flanked by two crossed polarizers. Spectroscopically it results in a fixed passband with a half-width of 32 Å. In order to obtain the desired line shift, the first to the seventh units are designed so that they can be rotated as explained above. The rotation of the quarter-wave plate of the second unit in relation to the second polarizer of the first unit causes a shift of ± 16 Å in the bandpass of the second unit. The following units 3 to 7 also start with a quarter-wave plate and end with a polarizer permanently oriented in the unit. Only the polarizer of the eighth unit is arranged separately. This polarizer can be swung out of the light path, then making possible to change the half-width from ¼ to ½ Å; the thickest calcite unit is spectroscopically ineffective once the polarizer has been swung out.

The orientation of the different plates and of the vibration direction of the polarizers (indicated in column 4 of Table III) in relation to the preceding and the following components is determined only once. Column 5 lists the half-width of the units and column 6 their speed of rotation; starting with unit one they follow a ratio 1:2:4 etc. up to a factor 64 with the seventh unit. Thus a 90° rotation of unit one (equivalent to a line shift of 16 Å) corresponds to 16 total revolutions of unit 7.

On the entrance side a multilayer interference filter for

the wavelength Hα is located as a prefilter Vf outside the main optical component housing (Figure 2.7). Its half-width is 60 Å and its transmittance 80%. In conjunction with a Schott KG heat-absorbing filter, this interference filter eliminates the undesirable heat radiation of the sun. The optical components in the housing are embedded in silicone oil (n = 1.5) providing an oil film between the different plates. The oil film also serves to reduce reflection at the surfaces and hence increases the transmittance of the filter and improves the optical quality of the solar image. The relatively high transmittance (43%) of the polarizers also contributes to an increased total transmittance of the filter.

Table IV gives a summary of the technical data of the Zeiss Lyot filter in its version A which I used. My set-up with the tunable Hα Lyot filter and the 35 mm Acme camera is shown in Figures 2.2 and 2.8.

2.1.3 THE DOPPLER-ZEEMAN ANALYZER

The magnetic maps of active regions were taken by David M. Rust and Ramesh Sinha with the Sacramento Peak Doppler-Zeeman Analyzer (DZA) during the summer and fall of 1971. The DZA has been described by Evans (1966) and its modified version by Dunn (1971c). I will simply state the principle of operation and keep the discussion of the problems encountered for the next chapter. Problems related to the interpretation of magnetograph measurements are numerous and still being investigated. Detailed discussion

Table IV

Summary of technical data of Lyot (Zeiss) filter

Item	Unit	Type A
Reference wavelength	Å	6562.8
Stability of reference wavelength	Å	±0.03
Half width -- may be switched to	Å Å	¼ ½
Line shifter	Å	±16
Transmittance for ¼ Å		
half width and incident plane polarized light	%	5
Clear apertures of filter		
entrance side	mm	36
exit side	mm	28
Admissible inclinations of beam		
at ¼ Å half width	degrees	1.6
at ½ Å half width	degrees	2.25

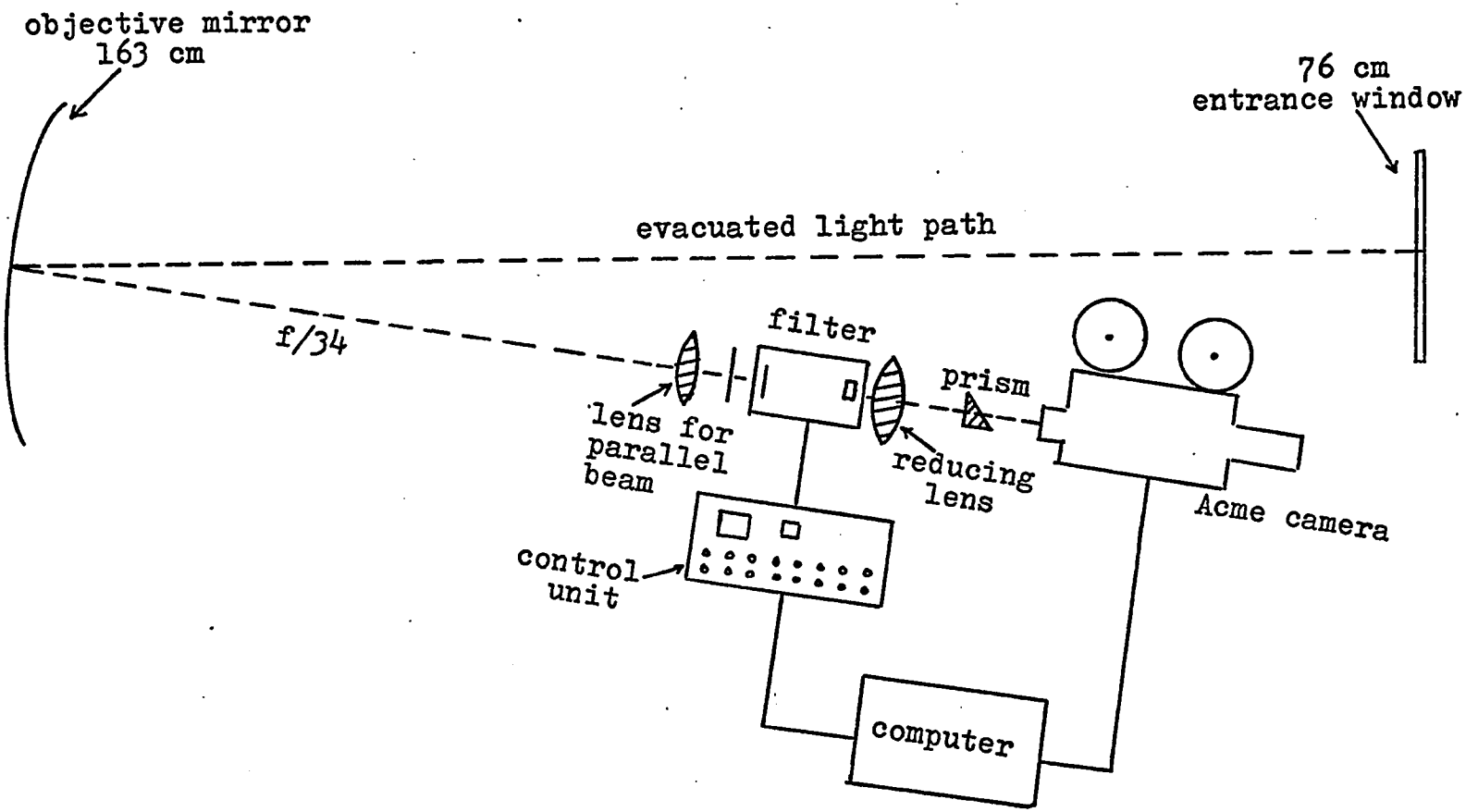

Figure 2.8. Schematic layout of the Hα monochromator in the observing system.

of related work appears in Howard (1971).

Certain absorption lines in the solar spectrum are magnetically sensitive in that they may be divided into components by the proper use of polarizing optics. The quarter-wave plate and polarizing beam splitter, in conjunction with the spectrograph produce two spectra that are called the right and left circularly polarized components of the light. In the presence of a longitudinal magnetic field, each polarized line profile (the two σ components) is displaced from its unperturbed position by an amount equal to

$$\pm \Delta\lambda = 4.67 \times 10^{-13} \lambda^2 \bar{g} B \qquad 2.7,$$

where B is the field intensity in gauss, λ the wavelength in Ångstroms and $\bar{g}$ the mean Landé splitting factor. Reversing the direction of the magnetic field vector will reverse the signs of polarization. The Doppler-Zeeman Analyzer gives a measure of the displacement of the σ components which is related to the intensity of the longitudinal component of the field, i.e. the line-of-sight component.

The purpose of the magnetograms is to provide a detailed magnetic map of the longitudinal field of active regions in order to reveal peculiarities in the magnetic field where surges tend to originate. All the magnetograms were taken with the iron lines listed in Table V. Magnetograms were supplemented by recordings from Mount Wilson Observatory in the form of large scale

magnetograms and visual Zeeman measurements of maximum field intensity in sunspots. Good sunspot observations are a very useful substitute for incomplete magnetograph data.

Table V

Iron lines for magnetic field recording

Å	multiplet		excitation potential eV	$\bar{g}$
5250.2	FeI	1	0.12	3.0
6173.3	FeI	62	2.22	2.5
6302.5	FeI	816	3.69	2.5
6336.8	FeI	816	3.69	2.5

CHAPTER III

OBSERVATIONAL PROCEDURE AND DATA REDUCTION

3.1 OBSERVING ELLERMAN BOMBS AND SURGES

3.1.1 OBSERVING PROCEDURE

Although I was assigned specific observing runs, I tried to arrange my schedule to coincide with the presence of promising active regions on the solar surface. Obviously, I chose the regions most susceptible to have surge activity: any young, complex or developing region is a good prospect; however, as any observer of solar activity has experienced to his despair, there are no general rules in this game. Choice of a specific region must be made because the camera field of view encompasses only a 18 x 24 mm frame out a solar image 215 mm in diameter; this represents a region of 117 000 km x 155 000 km (1.8×10^{10} km^2) or 160 x 214 arcsec (34 200 arcsec^2). To catch good events, one needs to be alert all the time to be ready to move to a more promising region. One has to be careful not to move without adequate reason; false alarms are numerous and one risks missing the beginning of everything. The best region is one which has already produced one or more surges in the preceding hours.

I set up the camera with the Zeiss Hα filter to scan continuously the profile of the Balmer Hα hydrogen line, for recording line-of-sight displacements of moving material in the chosen active region. The amount of line shift produced by material moving at line-of-sight velocity v is given by $\Delta\lambda/\lambda = v/c$, where $\Delta\lambda$ is the amount of displacement from the rest wavelength λ due to material moving with velocity v; c is the light velocity. The control unit attached to the Zeiss filter (Figure 2.2) allowed 8 channels, i.e. the passband of either $\frac{1}{4}$ or $\frac{1}{2}$ Å could be moved to eight positions across the Hα profile between ±16 Å. I generally used the $\frac{1}{4}$ Å passband (corresponding to a velocity dispersion of 11.4 km/s) in the following sequence: -2 Å (92 km/s), -1 3/8 Å (63), -7/8 Å (40), -5/8 Å (28), ±0 Å, +5/8 Å, +7/8 Å and +1 3/8 Å. Figure 3.1 shows the position of the passband across the solar photospheric Hα profile. This range might look narrow but it proved to be sufficient for the majority of cases; surge velocities reach about 150 km/s. At Hα 6562.8 Å the displacement is about 46 km/s/Å. Moreover, because of rapid changes at the base of the bomb structure, good time resolution (which in practice goes as the inverse of the filter range) is essential.

The computer was programmed to control the whole procedure. A sequence 20 sec long includes the time necessary for the profile scanning and for coming back to the starting point. The program was designed for a total

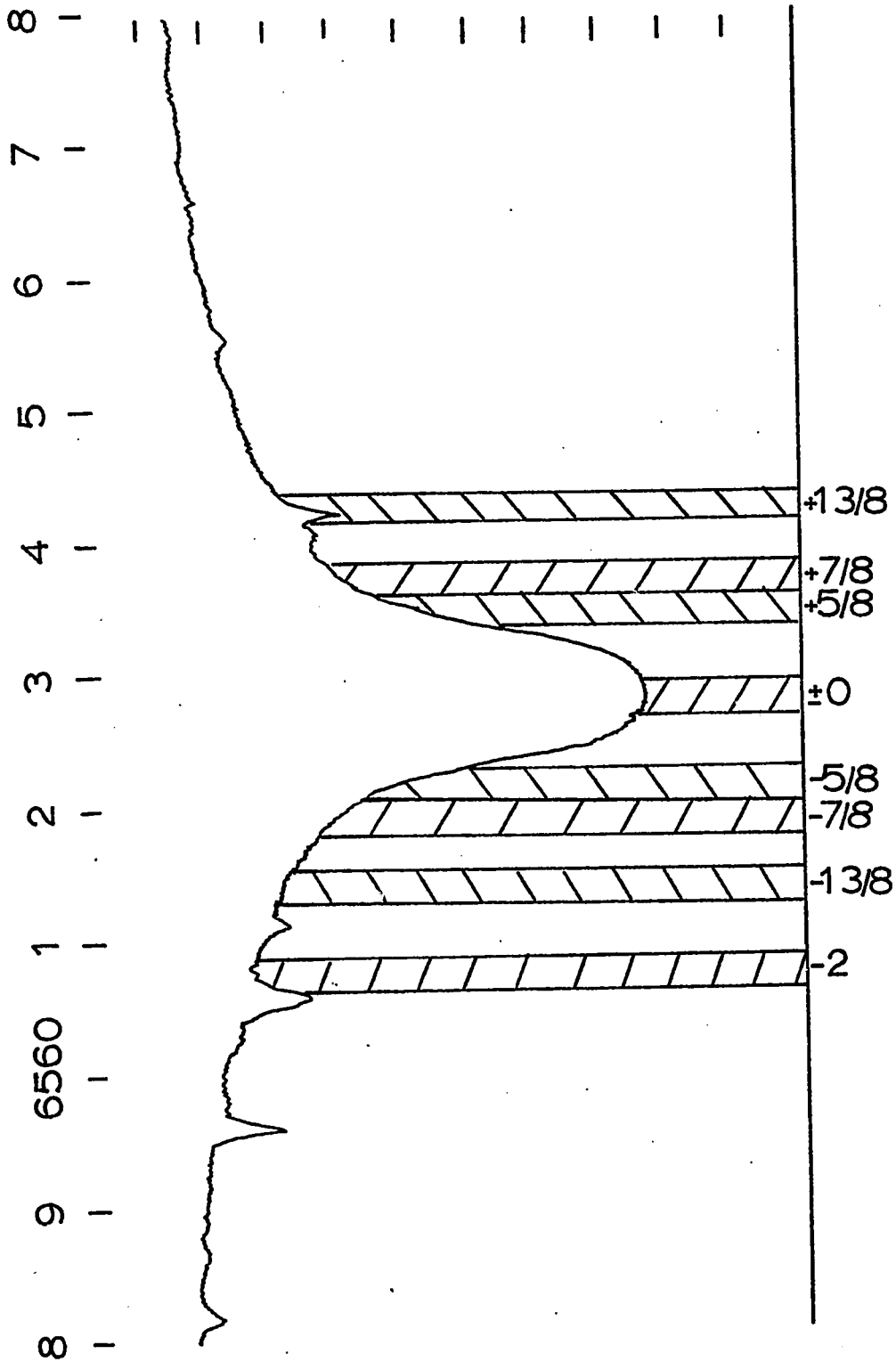

Figure 3.1. The solar Hα profile with the position of the filter passband (the passband half-width of ¼ Å is shown) stepped across the Hα profile in order to catch Doppler-shifted features in the chromosphere and the corona.

of 2000 loops (40 000 sec of running time) or sequences. Following the command to start a full sequence allowing a total time of 20 sec, the Acme camera receives a pulse of 0.1 sec to be armed, followed by a length of time of 0.3 sec to allow the camera to complete its operation cycle. The camera aperture is controlled by a specific voltage set at the corresponding channels on the Zeiss control unit (Figure 2.2). The filter passband moves to the next position in the Hα profile and so on. The result of this is a continuous sweeping of the Hα line at 8 different positions every 20 sec.

The recording film was KODAK Solar Flare Patrol Film (Estar base) type SO-392. It has a fine-grain, high contrast panchromatic emulsion with extended red sensitivity peaking in the region of Hα. By printing on 16 mm film the Hα-2 Å frames, then the Hα-1 3/8 Å, etc., I obtained cinematographic sequences at given wavelength shifts, corresponding to known line-of-sight velocities.

3.1.2 SEEING EFFECTS ON FILTERGRAMS

The problem of seeing is one affecting any investigation dealing with the study of fine structure in the solar atmosphere. Seeing is caused by very small differences in the refractive index of air from one point to another. These differences correspond to density variations that are due to small temperatures fluctuations from place to place. Air-temperature fluctuations of a few tenths of a degree are typical in the lowest km of atmosphere and larger differences occur closer to the surface due to the

heating by the sun. A fundamental property of these thermal variations is their linear scale. Direct measurements have confirmed that a whole spectrum of turbulence (mm up to tens or hundreds of meters) exists in the earth's atmosphere (Young, 1971).

The main effect of seeing is to smear filtergrams; it can result in a slight reduction of contrast or in a total blurring. It may be that only portions of the field of view are blurred. Filtergrams taken only seconds apart reveal that periods of bad and good seeing can succeed each other very rapidly. It is easy to reject pictures degraded by bad seeing because its effect is so obvious. Normally, one observes when seeing is at least fair, i.e. when features of the order of one sec of arc, e.g. photospheric granules, can be resolved. However, often one needs to keep observing spectacular events through periods of relatively bad seeing with the hope of recording a few frames during short periods of fair seeing. As we will see in section 3.2, the effect of seeing on magnetic mapping is not as easily detectable.

Periods of good-to-excellent seeing (i.e. better than one sec of arc) at Sacramento Peak Observatory occur regularly during the early mornings of summer months (May to September); those periods start generally about half an hour after sunrise and last at most for 2 to 3 hours. Summer being the rainy season in the Southwest (with almost daily showers or thunderstorms), these

periods of fair seeing apparently correspond to the larger thermal inertia of the atmosphere due to the higher water content. Observations have proven that the Vacuum Tower Telescope achieves its theoretical resolution (0.2 sec of arc) during the finest seeing periods; this remains possible in solar astronomy because of the short exposure times required (≈0.1 sec).

Seeing induced errors affecting the interpretation of filtergrams are the following:

a) a chain of small dot features takes the appearance of a continuous fuzzy filament;
b) decrease in contrast of small bright features; Ellerman bombs, for example, may be completely washed out;
c) smearing of thread-like structures into a solid sheet structure;
d) impossibility of identifying the base of dark features near the umbra of spots or pores;
e) impossibility of sketching the fine structure at the base of surges near the Ellerman bomb;
f) doubling of features in parts of the frame;
g) spurious position, size and morphological time changes of small features like pores.

3.1.3 INTERPRETATION OF DOPPLER EFFECTS ON FILTERGRAMS

The tunable Hα birefringent filter allows one to step the passband across the whole profile of Hα in order to monitor the line-of-sight velocity of Doppler-shifted features in the solar atmosphere. This is based on the

reasonable assumption that the large shifts ($> \frac{1}{4}$ Å) encountered in the solar atmosphere are caused by bulk motion of matter. This is also implied by the fact that a typical sequence of 8 filtergrams taken across Hα within 20 sec reveals a surge profile which is highly asymmetrical with respect to Hα 6562.8 Å in the presence of large shifts. No other mechanism is known to achieve such large asymmetry in the absorption profile of Fraunhofer lines in the solar spectrum. The presence of such moving features is confirmed by the observation of features with velocities perpendicular to the line of sight consistent with the observed Doppler shifts.

The observed Doppler width is related to the temperature T and microturbulent velocity v by the following equation

$$\frac{\Delta\lambda}{\lambda}_D = \frac{1}{c}\sqrt{2\,\frac{kT}{m} + v_t^2} \qquad 3.1$$

In active prominences like surges, low resolution spectra show the hydrogen lines as very broad, with Gaussian profiles often corresponding to values of $\Delta\lambda_D/\lambda$ between 1×10^{-4} and 2×10^{-4}. The higher value would give a broadening temperature in excess of 2×10^5 K which is unreasonable. A value of $v_t = 60$ km/s would account for this amount of broadening. High resolution spectra and filtergrams reveal the presence of a 'multi-stream' type of flow in surges (Figure 5.17 as an example).

In the first approximation, from the Doppler shift of area of maximum darkness in off-band Hα filtergrams, one can deduce the mean velocity of the material absorbing

radiation from below at the corresponding wavelength shift. The observed intensity coming from point (x,y) in the filtergram can be written

$$I(\lambda,x,y) = I_0(\lambda,x,y) \exp\left[-\tau_0(\lambda,x,y)\right] + \int_0^{\tau_0(\lambda,x,y)} S(\lambda,x,y,\tau) \exp\left[-\tau(\lambda,x,y)\right] d\tau \quad 3.2,$$

where $\tau_0(\lambda) = \tau_0(\lambda_0) \exp\left[-(\lambda-\lambda_0)^2/\Delta\lambda_D^2\right]$ 3.3,

with $\Delta\lambda_D$ given by eq. 3.1. $I_0(\lambda,x,y)$ denotes the intensity entering the surge from below, $\tau(\lambda,x,y)$ is the optical depth, $\tau_0(\lambda,x,y)$ the optical thickness of the surge along the line of sight, $S(\lambda,x,y,\tau)$ is the source function at an optical depth and $\lambda_0 = 6562.8\ (1 + \frac{v}{c})$ where v is the 'macroturbulent' velocity of the surge material. The observed filtergram results from the convolution of the observed profile I_λ with the filter passband transmission function. The point to emphasize is that the first term on the RHS of eq. 3.2 is strongly dependent on wavelength due to the fact that all surge motion takes place above the chromosphere responsible for the Hα rest profile. This implies that if maximum darkness of a feature is seen at Hα-5/8 Å, its bulk velocity may differ slightly from its inferred value through the Doppler shift from the filter passband center. This applies mainly in the area of the steepest part of the profile, i.e. for filtergrams taken between ¼ and 3/4 Å from the center of Hα.

A critical difficulty in interpreting off-band filtergrams lies in distinguishing between real motion of material

and visibility changes. Visibility is defined as

$$V = (I_{max} - I_{min})/(I_{max} + I_{min}) \qquad 3.4.$$

Because it is slowing down or accelerating, a knot or a thread of material is shifted to another wavelength where its visibility increases. The reality of moving material is ascertained:

a) by choosing moving features in the earliest stages of ejection when most of the material is moving in unison and is uncontaminated by differentially moving gas arising from successive bursts;

b) by outlining the velocity curve as a function of height or distance from the origin for all wavelengths of the same wing of Hα; all points if measured simultaneously in time should fall roughly along a same curve if representing real motion; motion wrongly derived from changes in visibility reveals strong discrepancies between the given wavelength shifts.

It is known that the tip of a surge tends to fade at its peak due in part to visibility changes, but also to possible heating by the corona. Although one must be careful in measuring velocities of knots at the peak of a surge trajectory, the problem is not as critical for theoretical interpretations as velocity measurements done very near the base of the surge.

3.2 INTERPRETATION OF FIELD MEASUREMENTS IN MAGNETIC REGIONS

Rust (1972) has investigated in some detail the procedure and problems involved in mapping evolving active centers

with the Doppler-Zeeman Analyzer (DZA). Most of his discussion is relevant to this work; I will summarize his main points further.

The DZA was designed to give rapid and precise mapping of the magnetic fields in active regions. In the DZA, two spectra are formed simultaneously one above the other. The top one is analyzed for the right-handed circularly polarized component and the lower for the left-handed component. The DZA simply measures the displacement of the spectral line relative to its average position by balancing the light passing through a slit on each side of the line. An unbalance causes an error signal that is amplified in a servo loop to drive a torque motor that, in turn, rotates a cube of glass until the signal is nulled. The amount of rotation of the cube, and thus the displacement of the line, is measured. If one assumes that the profile is symmetrical and regular, the DZA gives independent measurements of the central wavelength of the right-circularly polarized and left-circularly polarized profiles, corresponding to the 'R' channel signal and the 'L' channel signal respectively in the DZA; otherwise, only the position of midway between equal intensity points is given. The Zeeman signal (proportional to $\Delta\lambda$) is the difference in the L and R channel signals.

Because the instrument measures the right-circularly polarized and left-circularly polarized components of the line independently, it does not saturate in strong fields,

where the Zeeman splitting is comparable with or larger than the line width as it happens in the Babcock magnetograph. In the Babcock magnetograph, two fixed slits transmit the light from the steepest position of the line profile to photomultipliers. An electro-optical modulator alternately transmits only left-handed and right-handed circularly polarized light. If the light comes from a region of appreciable longitudinal field, the L and R component are separated; the signal is the alternating difference as the modulator alternates L and R light and gives an output signal proportional to the difference.

The apparent rest position of the spectral line changes slowly during DZA observations; this is due to thermal and gravitational shifts in the spectrograph. A fitting technique removes most of the zero drift. In setting up to observe, one has to be careful to center an active region completely and to provide broad bands of quiet sun around the edges. Thus, in finding the zero point of the magnetic scale, one assumes that the regions of smooth magnetic signal are regions of zero field, and that there are no broad plateaus of elevated fields. The many recent papers on the fine structure of the solar field indicate that this procedure is valid (see Stenflo, 1971). Usually, the empirically determined zero level does not vary by more than 5 G from map to map, even when the active region is shifted around in the scan area. The DZA is calibrated by measuring the line shifts produced by solar rotation.

The recording of magnetic changes associated with activity has proved to be an extremely elusive task due to poor spatial resolution, noise, and seeing effects which mimic field variations very easily; see recent comments by Michard (1971) and Rust (1972). Moreover, Sweet (1971) remarked that it is possible for the emerging and reentering flux to change connectivity without changing the observed longitudinal field; measurement of the transverse component is needed to record the complete change. Quantities like total flux $|F_+| + |F_-|$ or net flux $|F_+| - |F_-|$ of a whole active region have been used to detect changes which might be associated with flare occurence. Most observations have led to negative results and the few positive ones can be explained by calibration variations. For example, variation in the zero point by slightly more than $\frac{1}{2}$ G could account for a total flux change of 10^{21} Mx in a typical size map of an active region. Comparison of magnetograms from day to day must also take into account the apparent change of flux which is explained by the change in aspect angle, since a region moves on the average 13^{o} per day.

In my investigation, I searched for changes of small magnetic features (<20") on the magnetic maps taken with a scanning aperture of 5"x5" or 6"x6". Those have been known to be associated with some flares (Ribes, 1969; Michard, 1971 and Rust, 1972). The study of small magnetic structures is not critically dependent on calibration error

contrary to flux measurements involving a whole active region. However, the evolution of these small magnetic structures must be studied over the period of a few hours and seeing effects may mimic flux variations because the source of an intense magnetic field responsible for those small features may be of the same size as the seeing disk.

Mapping of active regions with the DZA is done with a scanning aperture normally larger than the seeing disk; the procedure uses for example an aperture of 3"x6" and the reduction program draws a map where the measured net flux over two successive measurements is averaged (i.e. 6"x6"). Therefore, the magnetograph does not resolve magnetic features less than six arcsec; it does not give the exact value of the field at one point but rather the net average field over the area of 4350 square km seen by the scanning aperture. Therefore, small magnetic features may actually be much stronger and with sizes smaller than 6". Also, 'valleys', which are regions of minimum magnetic field strength but of the same polarity as the parent spot, may be unresolved polarity reversals. Bad seeing conditions smear the magnetic maps by smoothing steep gradient and hills of strong fields (just as the optical image loses its contrast) and mimic weakening of these gradients (if seeing deteriorates) or strengthening of those features (if seeing improves) as illustrated in Figure 3.2. Therefore, in analysing successive magnetograms, one must monitor three or four apparently steady magnetic features similar in size

Figure 3.2. Magnetic maps in the line of FeI 6302.5 of region MW 18501 taken by R. Sinha with the DZA on 25 July 1971. Seeing conditions were poorer at 1551 UT (bottom map) than earlier at 1358 UT; this led to a smoothing out of sharp features and gradients. Negative fields in particular do not appear as intense and are more spread out at 1551 UT. For example, the average positive and negative fields were +36 G and -43 G respectively at 1358 UT and +32 G and -37 G at 1551 UT. This magnetic smearing corresponds to contrast reduction and blurring observed in filtergrams at periods of bad seeing. Contours levels are $\pm$10 G, $\pm$20 G, $\pm$40 G, ... Solid contours enclose positive field; dashed contours enclose negative field. This applies to all magnetic maps shown in this dissertation.

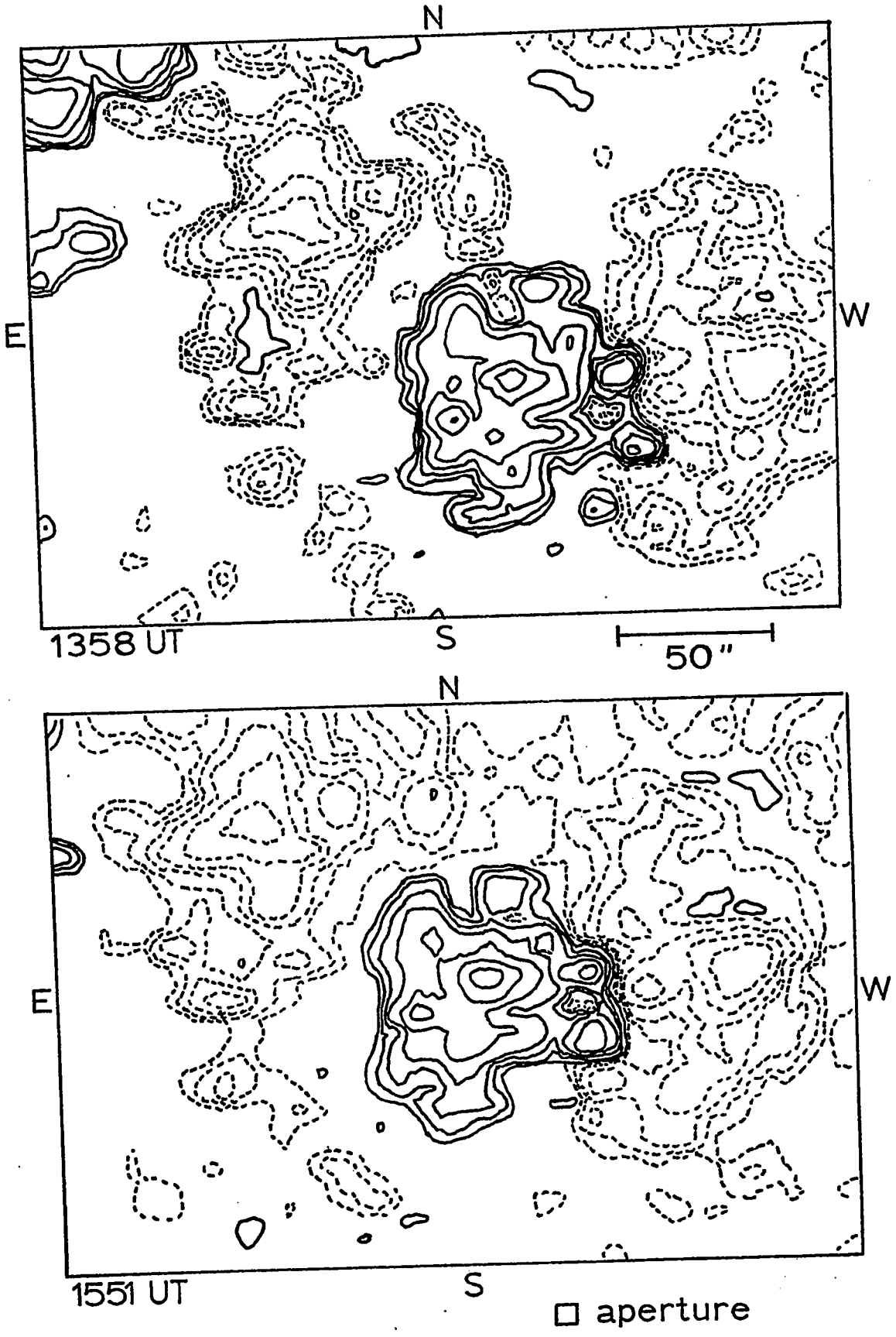
N
E
W
S
1358 UT
50"
N
E
W
S
1551 UT
□ aperture

and field intensity in order to demonstrate the variability of critical features. Comparison with optical images taken at the same time near the magnetograph site may help in evaluating the general quality of the seeing. It is also important to have a large number of maps over a period of a few hours; changes based on the comparison of two or three maps are unreliable. It takes on the average 5-10 min to map an active region; therefore, different portions of the scan are affected differently by the seeing condition or by light cirrus clouds.

Figure 3.3 illustrates the response curve of the DZA to magnetic field for different inclination angles γ of the field with respect to the line of sight. The response of the magnetograph remains linear up to field strengths of at least 1000 G (depending on the inclination of the field vector). At larger field intensities, the DZA gives a stronger response than expected from the $\cos\gamma$ law for a longitudinal magnetograph; this is due to the fact that the components of the spectral line are separated by such a large distance from the unshifted π-component, that the DZA is no longer influenced by the unshifted component. Thus, for large fields the DZA gives a signal which reaches 1.5 times the predicted value for 2000 G and $\gamma = 75^{\circ}$ (Figure 3.3); a field of 4000 G would be recorded at almost that level for any inclination of the field since for strong fields, the DZA measures the total field, regardless of its orientation. This explains why the DZA shows the

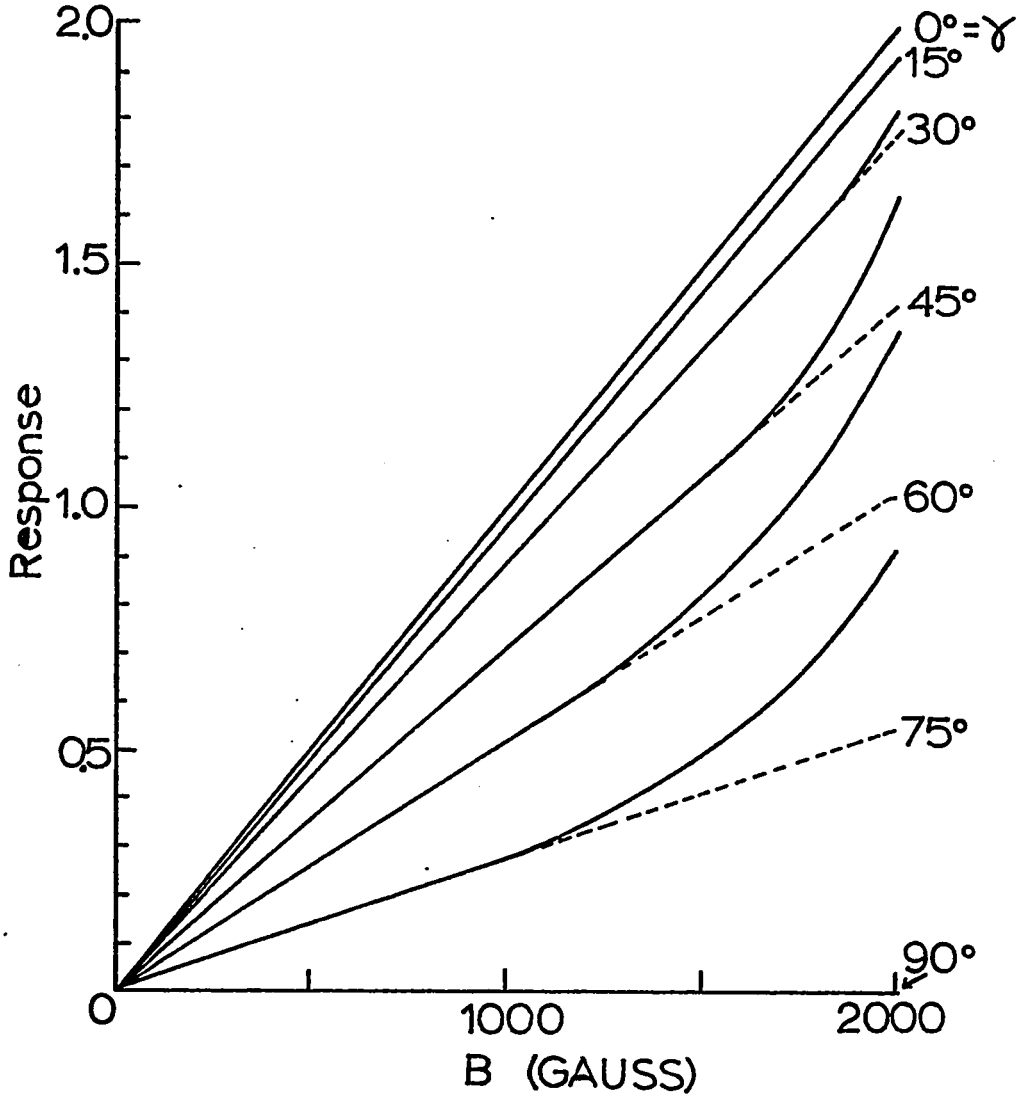

Figure 3.3. Response curve of the Doppler Zeeman Analyzer to magnetic fields for different inclination angles. The straight lines extending into dotted lines are the expected responses for a longitudinal magnetograph.

strong fields of sunspots in outstanding 'relief' even at large heliographic angles.

In Babcock-type magnetographs, the discrepancy between measured magnetic flux in different lines is explained by the temperature sensitivity to magnetic field strength of those lines (Harvey and Livingston, 1969); temperature effects appear most critical in weak fields. Because it measures the spacing between the unperturbed and the circularly polarized perturbed profile (not the intensity difference as the Babcock magnetograph), the DZA is less sensitive to such effects; nonetheless it gives values of magnetic flux about 10-20% lower with the line of FeI 5250.2 than FeI 6302.5 Å. Figure 3.4 a and b shows two magnetograms taken successively with the DZA in these two different lines; Table VI lists the fluxes measured in the two lines.

Studies by Rust and Sinha (1971, unpublished) indicate much higher fields when deduced from photographically recorded Zeeman splitting of magnetically sensitive lines than from DZA measurements; the discrepancy may reach a factor of two. Because of the higher resolution and lower light scatter of the photographic method, this is due to the compactness of spot fields. Thus the DZA tends to smooth out sharp field peaks, but the flux measurements maintain an accuracy within 25% of the true value (Rust, 1972).

Figure 3.4. Sunspot group MW 18594 (23 October 1971) was mapped successively with the DZA in the lines of FeI 5250.2 (2024 UT) and FeI 6302.5 (2056 UT) with a scanning aperture of 5" x 5". Position of the scan center: N05 W20. See Table VI for comparative data.

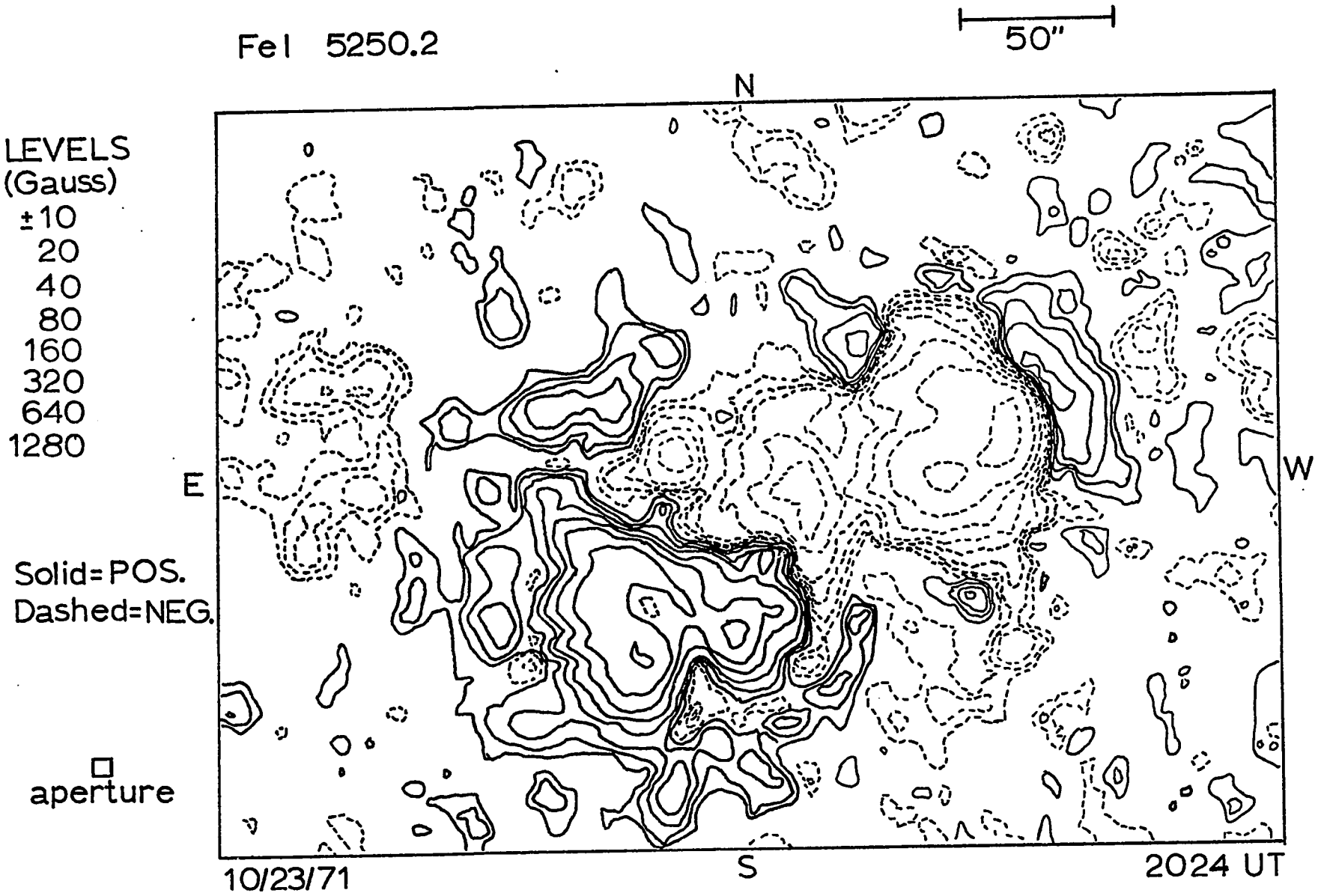
Fe I 5250.2
50"
N
LEVELS
(Gauss)
±10
20
40
80
160
320
640
1280
E
W
Solid=POS.
Dashed=NEG.
aperture
S
10/23/71
2024 UT

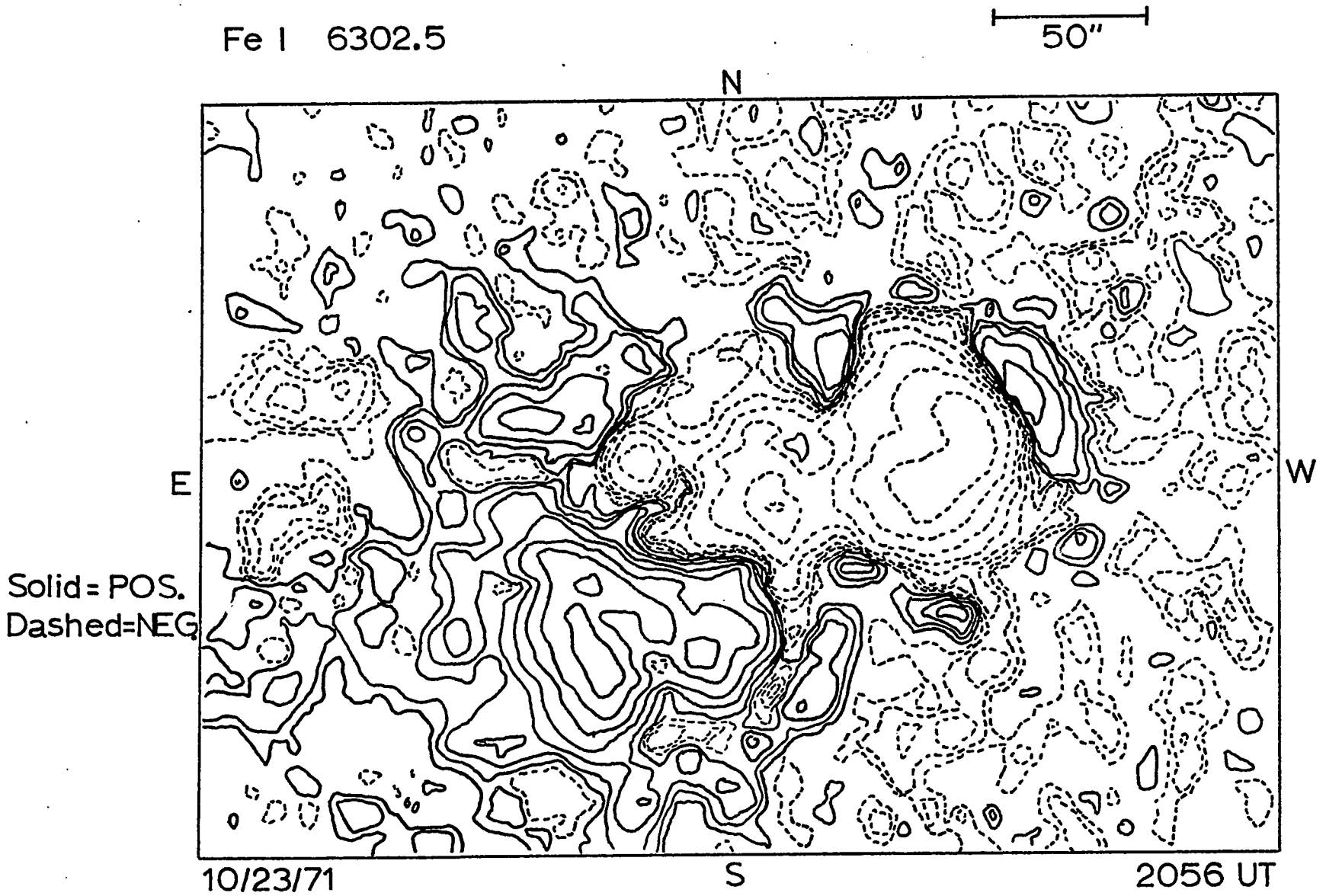
Fe I 6302.5
50"
N
E
W
S
Solid = POS.
Dashed=NEG.
10/23/71
2056 UT

Table VI

Magnetic flux in region MW 18594 (10/23/1971)

	FeI 5250.2	FeI 6302.5
Time	2024 UT	2058 UT
Maximum field	1326 G	1590 G
Minimum field	-1463 G	-1639 G
Average (+) field	55.5 G	69.6 G
Average (-) field	-72.5 G	-82.1 G
Average absolute field	64.0 G	76.0 G
F_+	1.188 E 22 Mx	1.46 E 22 Mx
F_-	-1.552 E 22 Mx	-1.789 E 22 Mx
$\|F_+\| - \|F_-\|$	-3.637 E 21 Mx	-3.235 E 21 Mx

CHAPTER IV

OBSERVATIONS

Table VII lists the main surge events I investigated. These surges occured in eight active centers over 16 days out of 28 different active regions I observed on 42 days between June and October 1971 (see Appendix III). The table also lists active centers MW 18235 (6-7 December 1970) and MW 18479 (27 June 1971) for which Dr. R. B. Dunn kindly provided me with his observations. The first column gives the Mount Wilson identification number of the active centers and their coordinates on the sun. The second column gives the Mount Wilson magnetic class of the active center for the same day it was observed; Appendix I presents the details of this classification and the percentage of occurence of the different classes. It is interesting to note that the $\beta\gamma$ class which has a frequency of 3% among all groups, enters 6 times out of 16, i.e. 38%, for the surge producing regions listed in this table. The $\beta\gamma$ class is characterized by a general bipolar configuration but the dividing line between polarities is not well marked. Furthermore, region MW 18468 which was βp on 29 June when it produced its importance 2 surge subflare associated surge, had moved

to βγ class on 30 June. Column three gives the date and time during which I used the Hα Lyot filter. The fourth column refers to the number of surge main events observed. I emphasize that surges are constituted of clusters of fine threads more or less independant; several ejective threads, not necessarily simultaneous, generally form a single surge event. The importance of the surges as defined in section 1.3 (Table II) is listed in the following column.

Column six summarizes the observed peculiarities in the magnetic field distribution or sunspot pattern which may be related to the observed activity. EMS, AFS and LIGHT BRIDGE are used as key words in Table VII in order to characterize the magnetic environment and history of the surge events. The statement EMS stands for 'evolving magnetic structure' characterizing a region of the order of 10^4 km across (less than 20") where magnetic field distribution and intensity is observed to change significantly over a period of less than 24 hours; chapter V deals with the problem of identifying EMS. AFS (Arch Filament System) describes a system of very low arch shaped prominences associated with rising flux tubes which lift the chromospheric material upward where it flows back downward along the flux tubes (Bruzek, 1969); AFS are associated with the very first few days of young active regions. f and p refer respectively to the following and preceding portions of the active center.

Light bridges are structures of bright (same as quiet photosphere) material crossing the umbra of some spots.

Column seven includes some remarks about the surge activity. Finally, column eight specifies the nature of the brightening associated with the base of the surge: B (Ellerman bomb), F (Flare of importance 1 or greater) and SF (Subflare); the distinction between Ellerman bomb and flare brightening will be discussed in section 5.1.3.

Table VII

Recorded bomb and surge activity

Mt Wilson region	Magnetic class	Time of observations	No. of events	Importance of surge
18235 E66 N14	$\beta\gamma$	12/6/1970 1600-1612 UT	1	2
18235 E55 N14	$\beta\gamma$	12/7/1970 1604-1620 UT	1	1
18479 E80 S10	βp	6/27/1971 1506-1541 UT	1	1
18479 E55 S12	$\beta\gamma$	6/29/1971 1518-1549 UT 1640-1739 UT	1	1
18468 W13 N15	βp	6/29/1971 1550-1638 UT	1	2
18468 W27 N15	$\beta\gamma$	6/30/1971 1553-1627 UT	2	S

Table VII

Recorded bomb and surge activity

Magnetic environment	Surge activity	Associated brightening
An area of (+) flux, 1600 G, present in the leading (-) portion disappears during the 6-7 Dec. interval. More (-) flux emerges at the west end of light bridge. EMS, LIGHT BRIDGE	Subflare and surge activity in a broad bridging penumbral region in the p spot on 7 Dec.	SF
No spot visible at -2 Å; location develops spots in the following days. EMS	Surge from intense brightenings visible as 10 bombs at -2 Å.	B
Ellerman bomb near a (-) spot. A pore (+1200 G) located in the (-) f portion has disappeared on 30 June when region has developed stronger (-) f. EMS	Surge stretches from the bomb.	B
Surge from bombs located near (-) pores in the f (-) portion. The day after, regions reveals new (+) flux in the area surrounded by subflare. Surge comes from bright kernel near (-) pores. EMS	Surge with spectacular thread structure. Brightest Hα kernel lays over 5 (+) pores. p (+,-) portion has a dozen of small surges with AFS.	SF, B
7 small surges seen in the developing (+) portion of center. AFS	Surges discriminated from AFS by higher visibility in the blue wing of Hα at the feet of AFS near disk center.	B

18511 E62 S15	αp	7/25/1971 1502-1622 UT 1645-1715 UT	6	1, 2
18511 W18 S13	αp	7/31/1971 1258-1542 UT	1	1
18522 E77 S10	αp	8/3 /1971 1355-1528 UT	3	3^+, 3, 1
18522 E63 S10	αp	8/4/1971 1311-1416 UT	4	S, 1
18538 E58 S13	$\beta\gamma$	8/19/1971 1514-1724 UT	2	1
18538 E42 S13	$\beta\gamma$	8/20/1971 1449-1706 UT	2	S

Surges from consecutive bursts of bombs located along the edge of light bridge adjacent to strongest polarity umbra (+) spot. LIGHT BRIDGE	Surges are dark or partly bright filaments extending from bombs. Full arch structure visible around 1505 UT.	B
Small surges from bombs (no visible pore related) west of double spot, in the prolonged direction of light bridge. Small (-) flux emerged through the (+) portion west of pores and disappeared on 1 Aug. EMS, LIGHT BRIDGE?	Small arch-shaped surges from bombs in (+) portion connected with (-) evolving magnetic polarity. Bombs within 10" of ems.	B
Nothing peculiar visible in spot pattern or magnetic configuration	Many spectacular sprays and surges out of region ahead single visible spot.	F
Region develops f(-) portion. A few pores have made their appearance. EMS	Intense bomb activity with ejections. Most spectacular event probably an eruptive prominence.	B, SF
Relatively quiet large group with surge from disturbed penumbra in p spot and at the end of light bridge in the f spot. No satellite spot visible. LIGHT BRIDGE.	See Big Bear SO show movie. Brightenings along edges of light bridge in p spot.	B
Bomb and surge activity along and at the end of light bridge of p spot. Surge coming from penumbral filaments instead of being radially directed are parallel to the border; the change may reveal a major modification of the transverse component of the magnetic field. LIGHT BRIDGE, EMS?		B

18538 W90 S13		8/30/1971 1646-1736 UT	1	S
18594 E26 N10	βp	10/19/1971 1946-2049 UT	1	1
18594 E17 N10	βf	10/20/1971 1418-1538 UT 1916-2030 UT	2	1
18594 E05 N10		10/21/1971 1345-1455 UT	2	S
18594 W05 N10	βp	10/23/1971 1347-1440 UT 1900-2055 UT	3	2, 1
18594 W80 N10	βp	10/27/1971 1403-1527 UT	1	S

	Surges on west limb common state of chromospheric activity above relatively quiet group.	B
Subflare with small surges in region of rising opposite polarity in f portion of group. EMS		SF
Small surges and brightenings in region of 'missing' penumbra ahead of p spot.		B
Small surge coming from region of satellite polarity trailing f portion. Coverage insufficient for change study.		B
Surge and bomb activity in weakening satellite (-) polarity, south of f (+) spot. Appearance and disappearance of pores observed along flux change rate 3×10^{15} Mx/s. EMS	3 homologous surges during the second period of observing; surges originate at cluster of bombs	B
Bombs and small ejections along light bridge in the p spot. LIGHT BRIDGE		B

CHAPTER V

RESULTS I. THE SURGE ENVIRONMENT

5.1 THE RELATIONSHIP BETWEEN Hα BRIGHTENINGS AND EJECTIONS

5.1.1 INTRODUCTION

The spike of dark or bright material of a surge always tends to grow out rapidly from a small compact knot with a diameter of a few arcsec or less. The knot may reach flare intensity within 5-10 min. These bright knots or Ellerman bombs (Ellerman, 1917), whose spectral properties are of the same kind as 'moustaches' investigated by Severny and Koval (1961) and by Koval (1964, 1965a, b, 1967), form the base and possibly the source of the surge (Bruzek, 1969). This is confirmed by the fact that almost every surge I studied, extends from Ellerman bomb brightenings which appear at the initial phase of the surge (Figure 5.1). McMath et al. (1960) were the first to confirm the identity between Ellerman bombs and moustaches.

Table VIII shows the relation of the surges I studied with the Hα brightenings located at their bases. The table summarizes the surge activity recorded in 8 active centers occuring on 16 different days. The table is biased for the larger importance surges; the contribution of normal active regions to small size ejections is based mostly on a detailed

Figure 5.1. (i) At top, regions MW 18479 (E43 S11) in the background and MW 18476 (E40 S14) in the foreground at 1525 UT on 29 June 1971. (ii) At bottom, region MW 18594 (W20 N08) at 1931 UT on 23 October 1971. The arrows point to Ellerman bombs with associated ejections of different sizes. Both filtergrams are at Hα-7/8 Å.

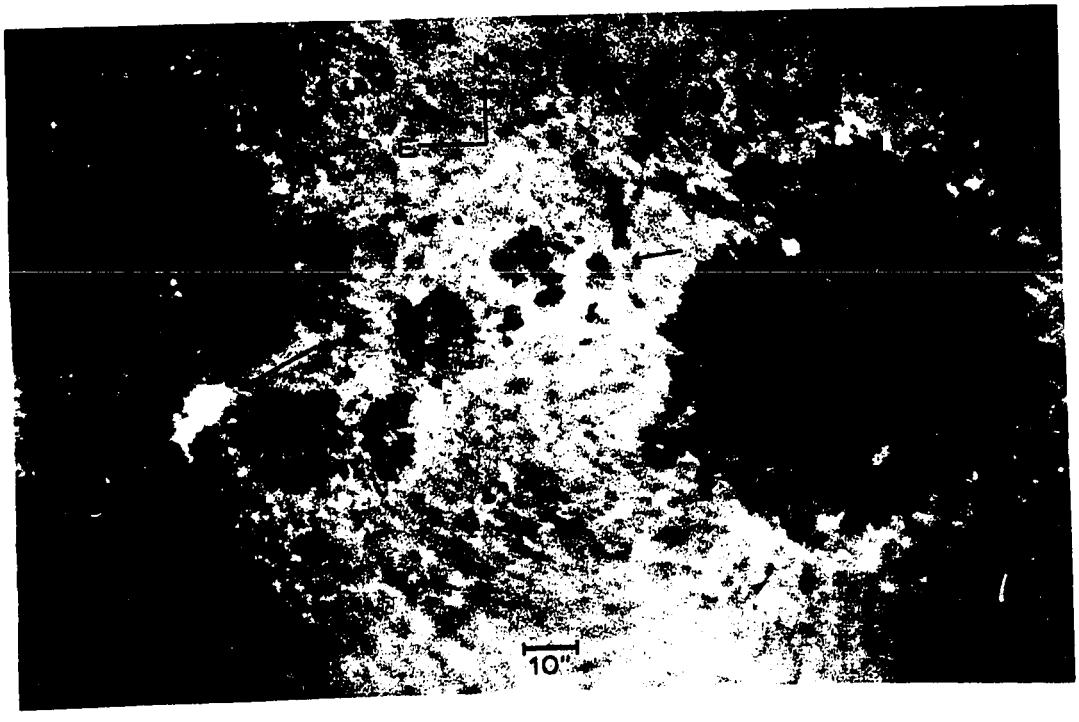
10"

study of only two active centers (MW 18468 and 18522) so that the real contribution of bomb associated surges is much higher than shown. Therefore, most surge activity is related to Ellerman bombs. The largest surges (importance 3 and 3^+) may be related to flares only; however these events might be classified as sprays as are the two Imp 3 objects of Table VIII. In 6 of 7 cases of surges related to subflares, the ejecta originated from a bright Hα kernel of the flare; however, most bright kernels of flares were not ejection producers.

Table VIII

Surge relationship to Hα brightenings (number)

Surge importance	From flare	From subflare	From Ellerman bombs
S	1	1	155
1	1	4	12
2	0	2	4
3	1*	0	0
3^+	1*	0	0

* August 3, 1971 events; most likely sprays

Curves showing how surges develop just after bombs or subflares appear in Figure 5.2: the dark ejection appears near the maximum brightness phase of the bomb and stretches to maximum extent while the bomb fades away. The close relationship between bombs and surges suggests that there exists a physical link between the two phenomena; I have

Figure 5.2. Relationship between bomb and surge development. The vertical scale refers to relative intensity for bombs and relative extent for surges. In the case of 29 June 1971, the flaring is a subflare while in the other events they are bombs with shorter lifetimes. Actually, most peaks of bomb activity in MW 18511 and 18594 are composed of a few brief bomb flashes; surge threads develop from these flashes (Figure 5.1). Bomb lifetimes were measured at Hα-2 Å. Maximum extents are 30 000 km for the 25 July 1971 surge veil, and about 100,000 km for the 23 October and 29 June 1971 surges; bomb intensity at Hα-2 Å ranges roughly from 80% of the close-by continuum at minimum to 105% at maximum.

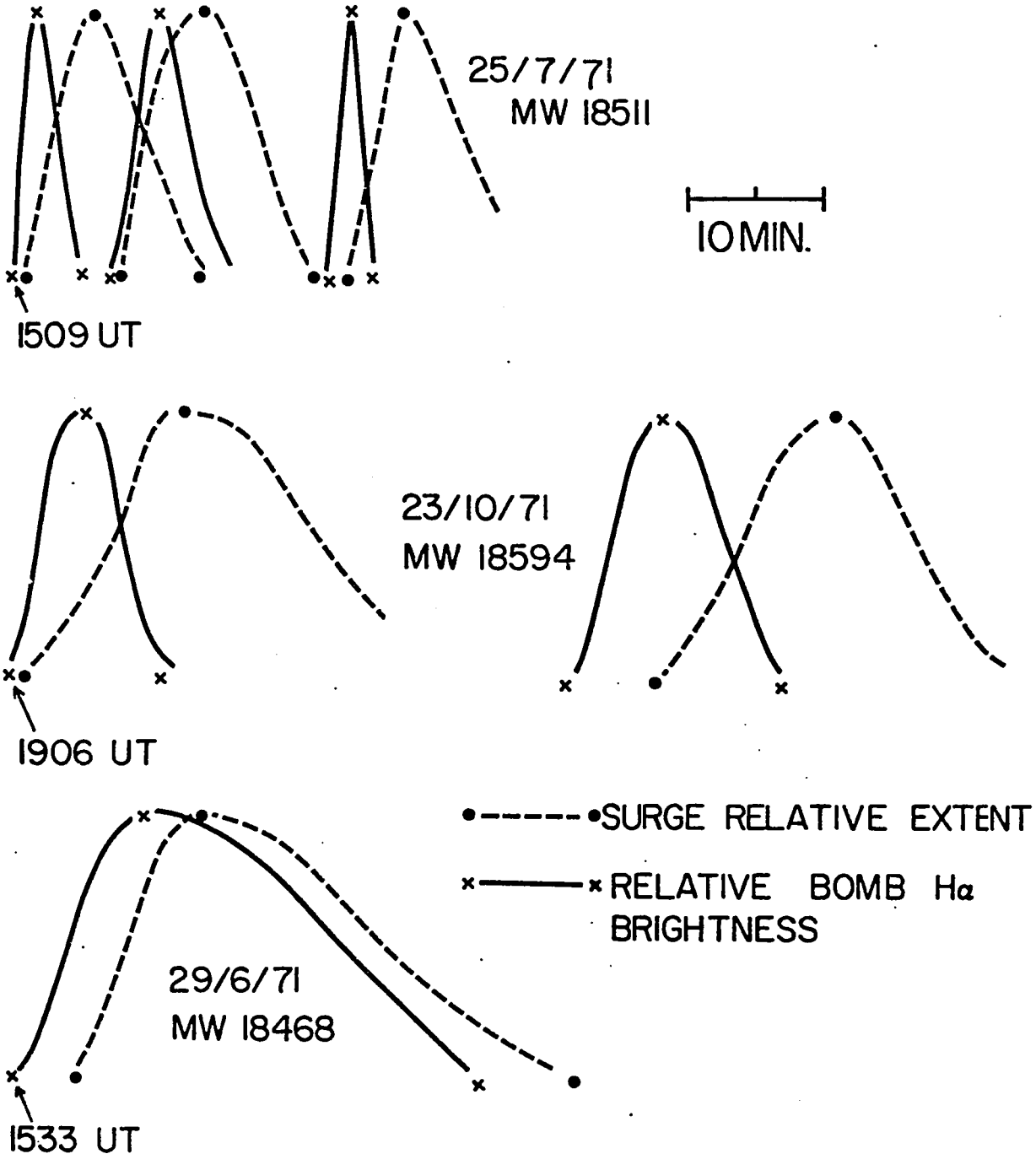
25/7/71
MW 18511
10 MIN.
1509 UT
23/10/71
MW 18594
1906 UT
SURGE RELATIVE EXTENT
RELATIVE BOMB Hα
BRIGHTNESS
29/6/71
MW 18468
1533 UT

therefore investigated in some details the properties of bombs in two active regions: MW 18468 (29 June 1971) near disk center and MW 18522 (4 Aug. 1971) near east limb, respectively βp (bipolar, main spot preceding) and αp (unipolar, faculae following) in the Mt Wilson magnetic classification of sunspot groups (see Appendix I).

5.1.2 OBSERVATIONAL

Engvold and Maltby (1968) found the intensity maxima (about 5-10% above the local continuum) in profiles of bombs to occur in the range 0.5-2.0 Å off Hα with strong central absorption. Bombs are hardly visible in the core of Hα because of interposing chromospheric material. Bombs being best visible off-Hα±0 Å, I used high resolution observations (~1/3") obtained with a Lyot birefringent Hα filter having a tunable bandpass of ¼ Å. Table IX lists relevant data about the regions studied and the Lyot filter sequence used. Bomb activity in MW 18468 was associated with a small developing region with an arch filament system and emerging opposite flux in the leading portion of the group. In region MW 18522 near east limb (Figure 5.3), the eastern portion of the active center was in its emerging phase. Table X lists the regions with their bomb distribution. The difference between the total number of bombs and those measured (columns two and three) is due to bombs present at the beginning of the film and others still active when the film finished. Homologous bombs (fourth column) refer to two or more (up to five)

Table IX

Active regions studied

Region	Magnetic class	Date 1971	Time of observation UT	Position	Length of filter sequence	Wavelength shift from H ±0 Å
MW 18468	βp	6/29	1550-1638	W13 N15	25 s	-2, -1 3/8, -7/8, -5/8, ±0, +5/8, +7/8, +1 3/8
MW 18522	αp	8/04	1311-1416	E65 S10	20 s	

Table X

Ellerman bombs in active regions

Region	Total number of bombs	Number of bombs measured	Homologous bombs & (groups)	Bombs accompanied by ejections
MW 18468	103	69	46 (21)	58 (56%)
MW 18522	75	60	41 (16)	65 (86%)

Figure 5.3. Filtergrams at Hα+7/8 Å (top) and Hα-2 Å (bottom) of region MW 18522 (E65 S10) on 4 August 1971, 1345 UT. About 20 Ellerman bombs are visible in the upper filtergram; some of the brightest bombs also appear at Hα-2 Å. Notice the numerous pores in the following portion of the active center. The solar limb can be seen in the upper left corner.

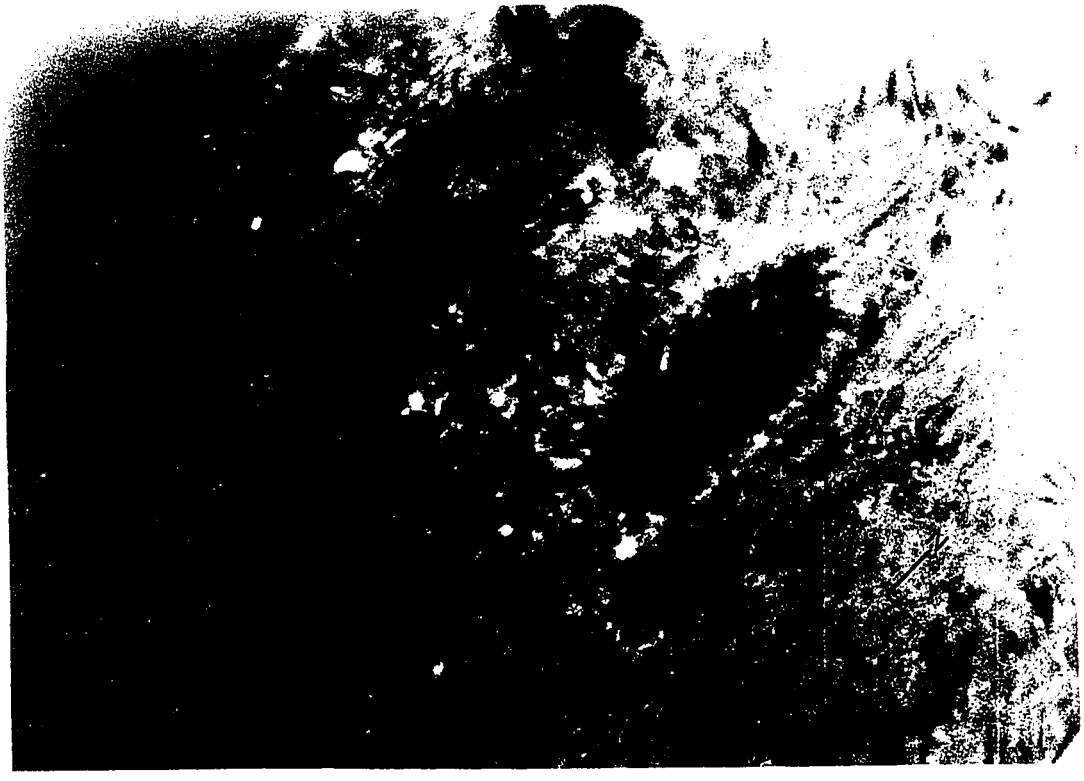

events originating within less 2" of the same position.

5.1.3 ANALYSIS AND RESULTS

Engvold and Maltby (1968) pointed out the problems of identifying bombs. How does one distinguish between Ellerman bombs and bright points in the photospheric network or subflares when observing at Hα? Bombs are only rarely visible at Hα±0 Å while subflares are brightest there. One also differentiates the bomb from the subflare by its compactness; filtergrams of subflares reveal their wiggly structures like lightning strokes. Photospheric bright points appear dimmer than bomb brightenings and do not undergo impulsive brightening.

I found relatively little difficulty in identifying bombs at more than ½ Å from Hα±0 Å. The analysis was facilitated by running the 16 mm film at high speed through a variable speed projector. I searched for points with brightness fluctuations of the order of a few minutes. I took as the bomb duration the measured time between the first impulsive brightening and complete dimming to surrounding brightness. Finishing times are not as well defined as are starting times; as mentioned by Vorpahl and Pope (1972), some bombs tend to pulsate; others do not just disappear, but tend to a minimum and flare again later. For those cases, the time of minima was defined as finishing time. Only six of the 75 bombs in MW 18522 and one of the 103 in MW 18468 could be seen at Hα±0 Å. In general, absorbing material obscured completely the bomb locations;

at best they coincide with extended diffuse plage emission.

Results about the lifetimes and the locations of bombs are presented in the form of block diagrams in Figures 5.4, 5.5 and 5.6 and in Tables XI and XII. Time delays in Figure 5.6 are evaluated with respect to starting and ending times at Hα-2 Å. The reasons for choosing -2 Å as reference are its reliable timing and its large sample size. The 'error' bars in the curves (Figure 5.5) of mean durations as a function of wavelength shift are evaluated from the timing discrepancy of bomb starting and finishing times (third and fourth columns of Table XI); they represent the mean deviation of three or four repeated measurements for each of a dozen of representative bombs. Table XII lists the mean durations of Ellerman bombs as function of their locations; the shorter mean duration by about 20% in pore associated bombs is systematic and probably significant statistically and physically. The close association between bombs and the outer edges of penumbrae (within 7"), pores (within 2-3") and the photospheric network (within 5") implies the association of bombs with the boundaries of magnetic field concentrations.

Cinematographic analysis also reveals a close relationship between bombs and the ejection of dark or bright material. Ejections in the form of moving threads 3-30" long connecting to bombs were investigated at each wavelength near Hα; these ejections always appear within minutes of the bomb brightness maximum. I classified ejection as associated with a bomb if I could detect at one or more of the six wavelength

Figure 5.4. Histograms showing the distribution of Ellerman bomb durations per interval of two minutes for regions MW 18468 near disk center (see Figure 5.17) and MW 18522 near east limb (see Figure 5.3). The dashed arrow indicates the median and the full arrow the mean. There are no data for -7/8 Å (MW 18522) and +7/8 Å (MW 18468) because of a technical difficulty in printing the original film on 16 mm. No Ellerman bomb could be identified at Hα±0 Å in MW 18468.

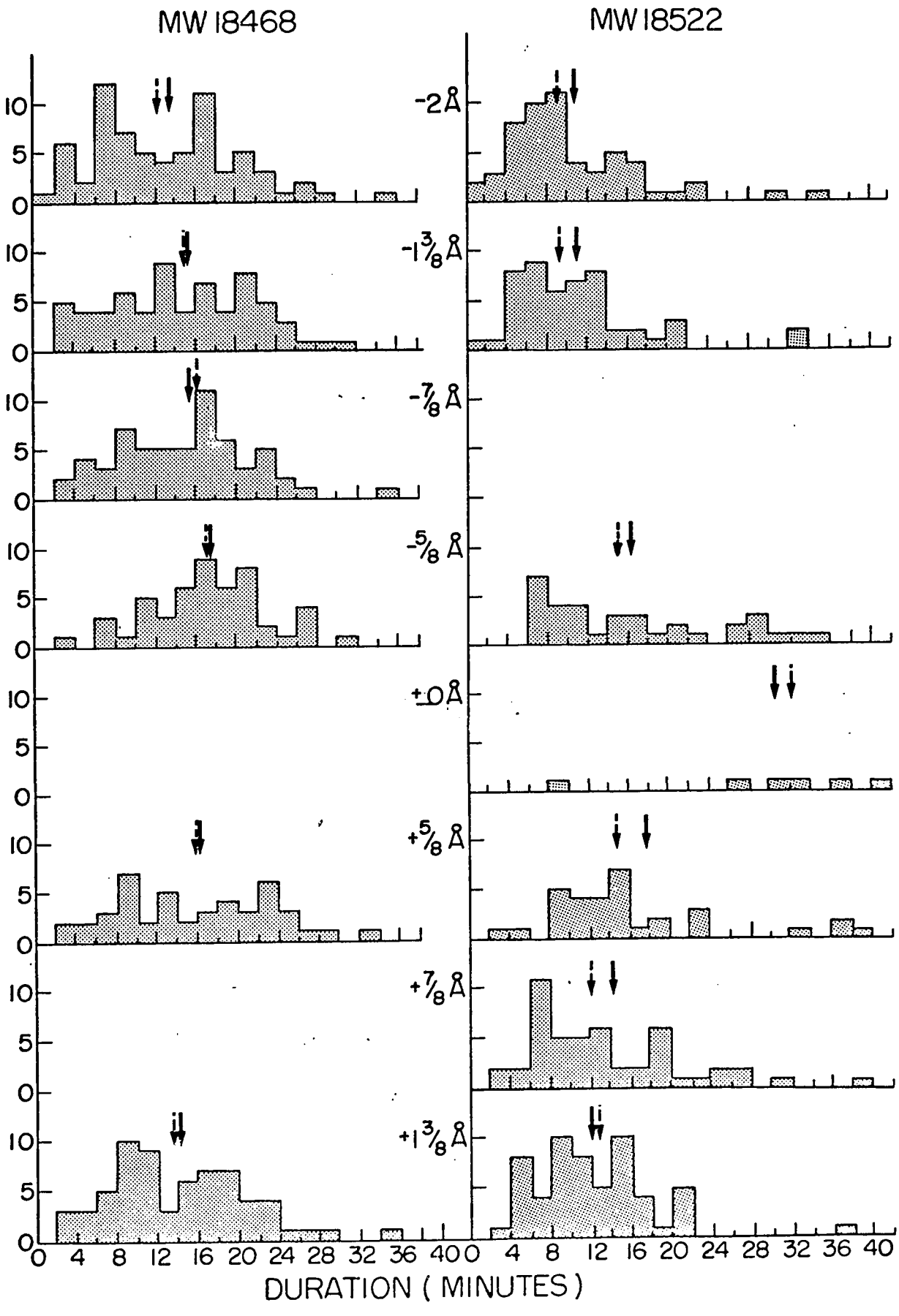
MW 18468
MW 18522
-2Å
-1 3/8 Å
-7/8 Å
-5/8 Å
+0Å
+5/8 Å
+7/8 Å
+1 3/8 Å
0 5 10
0 4 8 12 16 20 24 28 32 36 40
DURATION (MINUTES)

Figure 5.5. Mean durations of Ellerman bombs vs wavelength near Hα. The error bars are discrepancy bars as explained in the text.

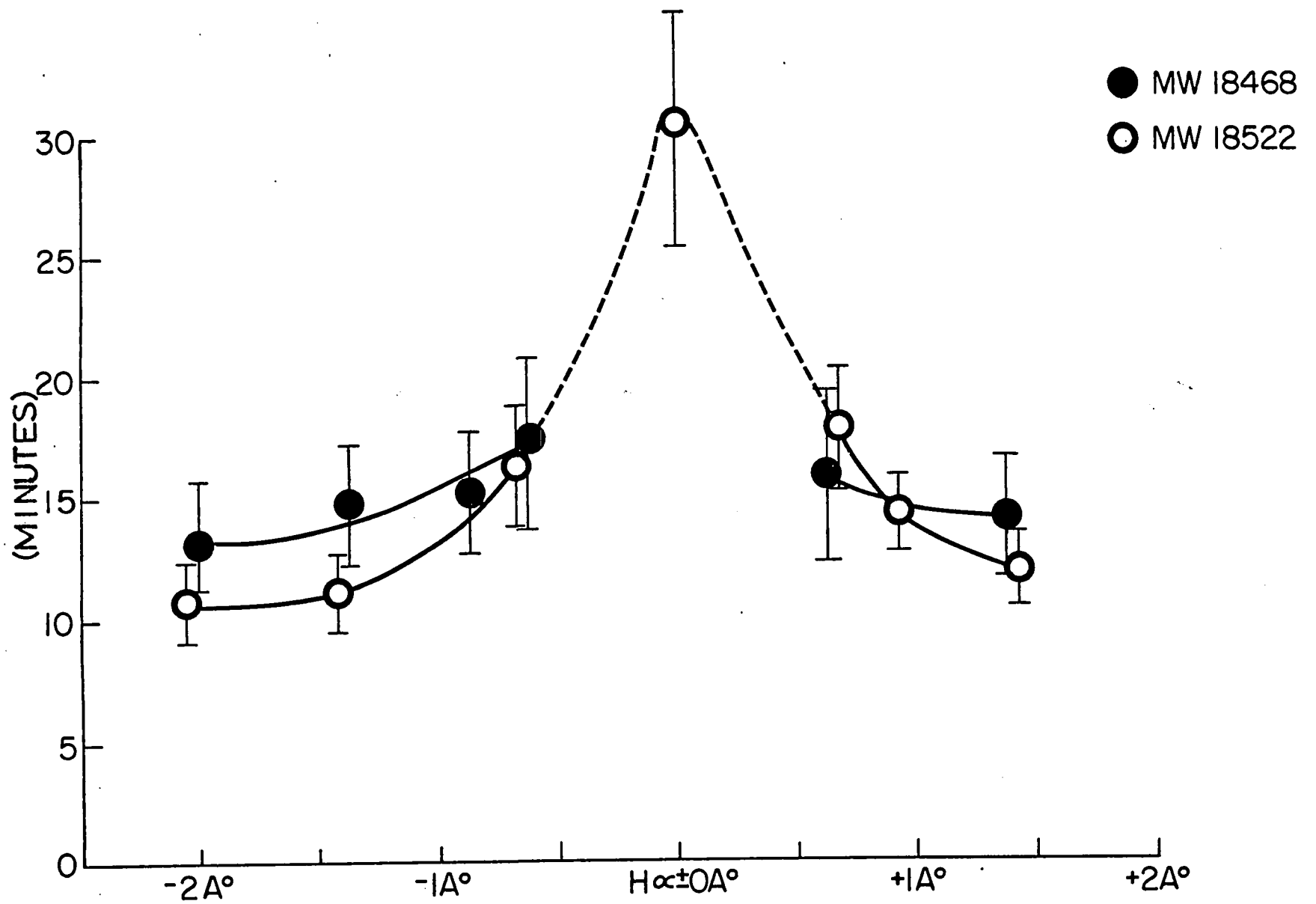
MW 18468
MW 18522
30
25
20
15
10
5
0
(MINUTES)
-2A°
-1A°
Hα±0A°
+1A°
+2A°

Figure 5.6. Histograms of time delays between bombs at Hα-2 Å (reference wavelength) and at other wavelength shifts near Hα for starting and finishing times. Bombs tend to start at about the same time at all wavelengths near Hα and to finish later (than -2 Å) at these wavelengths. Events with negative (positive) delays start or finish earlier (later) than their corresponding events at Hα-2 Å.

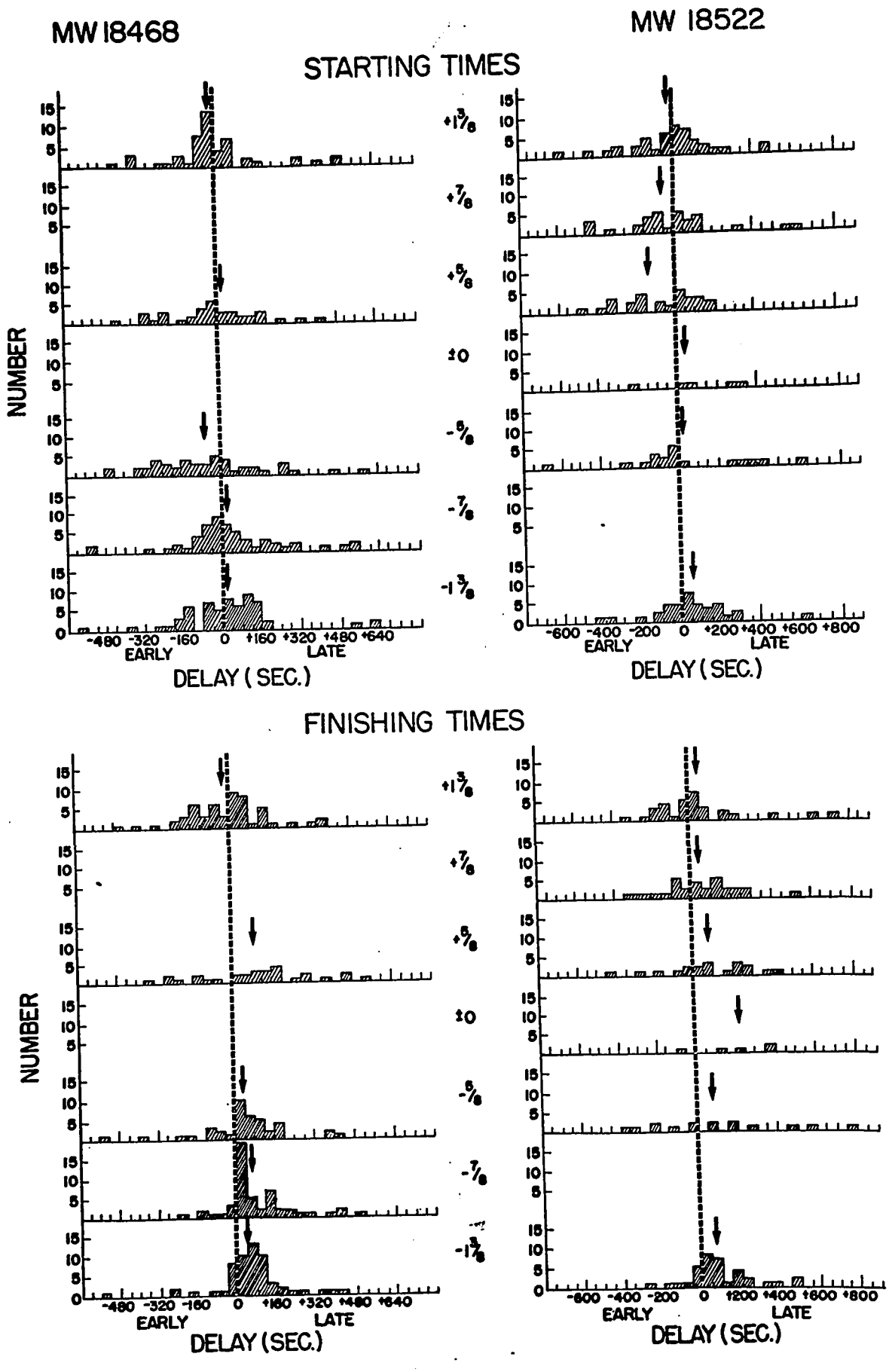
MW 18468
MW 18522
STARTING TIMES
NUMBER
+1 3/8
+7/8
+5/8
±0
-5/8
-7/8
-1 3/8
-480 -320 -160 0 +160 +320 +480 +640
-600 -400 -200 0 +200 +400 +600 +800
EARLY
LATE
DELAY (SEC.)
FINISHING TIMES
NUMBER
+1 3/8
+7/8
+5/8
±0
-5/8
-7/8
-1 3/8
-480 -320 -160 0 +160 +320 +480 +640
-600 -400 -200 0 +200 +400 +600 +800
EARLY
LATE
DELAY (SEC.)

Table XI

Duration of Ellerman bombs

(Å)	sample size	timing discrepancy (min) start	timing discrepancy (min) end	mean duration (min)	median duration (min)	standard deviation (min)	skewness
			MOUNT WILSON 18468				
-2	69	±1.0	±1.5	13.3	12	7.3	+40
-1 3/8	66	1.0	1.5	14.8	15	7.1	+ 2
-7/8	61	1.0	1.5	15.2	16	6.5	+15
-5/8	50	1.5	2.0	17.3	17	6.0	+ 3
+5/8	45	1.5	2.0	15.9	16	7.4	+ 4
+1 3/8	65	1.0	1.5	14.1	14	6.9	+39
			MOUNT WILSON 18522				
-2	56	±0.6	±1.0	10.7	9	6.9	+79
-1 3/8	50	0.6	1.0	11.1	9	6.5	+78
-5/8	34	1.0	1.5	16.3	15	9.0	+21
±0	6	1.5	3.5	30	32		
+5/8	34	1.0	1.5	17.8	14	10.7	+36
+7/8	50	0.6	1.0	14.3	12	8.8	+62
+1 3/8	60	0.6	1.0	12.0	12	6.0	+69

Table XII

Mean durations (min) of Ellerman bombs at various locations [a]

	edge of penumbra	edge of pore	in bright photospheric network	isolated
	MOUNT WILSON 18522			
% of total	40%	14%	40%	6%
-2 Å	12 (26)	8 (6)	10 (22)	11 (4)
-1 3/8 Å	11 (20)	9 (7)	11 (22)	14 (4)
-5/8 Å	18 (16)	13 (4)	18 (11)	10 (3)
±0 Å	32 (1)	9 (1)	36 (4)	- (0)
+5/8 Å	16 (19)	7 (5)	24 (11)	22 (1)
+7/8 Å	14 (23)	13 (5)	15 (20)	17 (4)
+1 3/8 Å	12 (25)	10 (10)	13 (28)	14 (4)
	MOUNT WILSON 18468			
% of total	20%	25%	55% [b]	
-2 Å	10 (13)	10 (16)	16 (34)	
-1 3/8 Å	15 (12)	13 (15)	16 (33)	
-7/8 Å	12 (11)	14 (12)	17 (31)	
-5/8 Å	15 (6)	16 (12)	18 (28)	
+5/8 Å	16 (8)	14 (7)	16 (28)	
+1 3/8 Å	14 (11)	11 (12)	15 (35)	

[a] The number in brackets indicates the sample size.

[b] The photospheric network cannot be distinguished at disk center.

shifts an associated ejective feature following within a few minutes the appearance of a bomb. In MW 18522, 65 (86%) Ellerman bombs were seen to be followed by a small ejection and 58 (56%) in MW 18468. The largest number of ejecta were seen at -5/8 Å in MW 18522. Very few appeared at -2 Å. In MW 18468 ejections are visible as frequently at -2 Å as at any other wavelength shift, reflecting the high velocity of those features (at least 100 km/s).

5.1.4 DISCUSSION

Mean durations of bombs at disk center are larger by about 20-30% than near the limb; the lifetimes as a function of wavelength near Hα vary less at disk center than near the limb (Figure 5.5 and column five of Table XI). However, lifetimes are about the same at 3/4 Å from the core of Hα for both regions. This reflects the fact that the Ellerman bomb is a low chromosphere phenomenon. While bombs generally have a triangular or elongated shape at large heliocentric angles, they are almost exclusively point-like objects near disk center; this indicates an elongation of the bombs normal to the surface. The bomb lifetime distributions and means are in agreement with the lifetime range (1.5-20 min) quoted by Severny (1964).

In view of the relationship of bomb with ejection of dark material, the observed delays (Figure 5.6) as a function of wavelength shift imply an asymmetry of the bomb Hα profile which may evolve throughout the bomb duration. The possibility that motion of absorbing material between the observer

and the bomb might explain in part the asymmetric line profiles of moustaches has been suggested by Koval (1964, 1965), Engvold and Maltby (1968) and Bruzek (1972). But the problem of asymmetry remains complex (Severny 1964, 1968; Koval and Severny, 1970).

This study is limited in the following respects:

(1) This analysis deals with transient Hα brightenings with light fluctuations shorter than the observing period, i.e. less than one hour; McMath et al. (1960) mention events lasting for hours. Because of the crude visual method, an ambiguity remains in distinguishing between emission grains in the photospheric network and Ellerman bombs seen in off-band filtergrams (see Bruzek, 1972). Still, events longer than 30 min are exceptional (Figure 5.4).

(2) Very short bursts less than a few tens of seconds in duration appear numerous at the limit of resolution. I had an event lasting 20-40 s in MW 18522 and one lasting 50-75 s in MW 18522. Better time resolution is needed to explore those events.

Bombs accompanied by ejections were generally resolved and could be measured in a very rough manner; in some cases, it was hard to differentiate between a large bomb and a cluster of two or three smaller bombs. I measured the bomb dimensions near its brightness maximum on enlarged prints (1.7 mm/arcsec) of region MW 18522 at Hα+7/8 Å; I took into account the various shapes of bombs by establish-

ing the size of a bomb brightening as the product of its largest axis by its smallest. The size of the brightening as I defined it cannot be considered to be the physical size of the bomb without assumptions. However, it provides a direct way for grading bomb 'sizes' in order to relate the importance of a bomb with other properties like the length of the associated ejection.

The frequent association of bombs with dark or bright ejecta remains a most interesting feature of bombs. The high rate of occurence (86%) in MW 18522 of accompanying ejections suggests that the two phenomena are closely linked. The smaller percentage (56%) in MW 18468 near disk center is probably due to the large Doppler shift of ejecta and to the less favorable geometry for detection. The thread-like shape of these ejecta is suggestive of magnetic control, making them appear as small scale versions of the larger surges investigated by Roy (1973).

To investigate a possible relationship between the size of the ejection and the properties of its associated bomb, I calculated the correlation coefficient (Pearson's coef.) for 34 sets of observations in MW 18522. Correlation coefficients were found to be (i) $r = 0.26$ between ejection size and bomb size; (ii) $r = -0.14$ between ejection size and bomb lifetime; (iii) $r = 0.35$ between ejection size and bomb size times bomb lifetime. The only significant correlation is the one between the ejection apparent length and the size times lifetime of the associated Ellerman bomb.

For the 34 pairs of observations, the probability is less 5% that the value $r \geq 0.34$ will occur by chance. The significant positive correlation between the apparent length of the ejection and bomb size times bomb duration is consistent with a model where the surge material is squeezed out from the bomb itself.

5.2 THE MAGNETIC ENVIRONMENT OF SOLAR SURGES

In the following paragraphs, I discuss various photospheric sunspot patterns and magnetic configurations associated with surges. Most configurations fulfill, although on a smaller scale, the criterion of 'structures magnétiques évolutives' or evolving magnetic structures (EMS) introduced by Martres *et al.* (1968).

5.2.1 SURGES AND SATELLITE POLARITIES

The best known type of surge-generating region is the satellite spot imbedded near the penumbra of a larger opposite polarity spot (Gopasyuk *et al.*, 1963; Rust, 1968). However, because most magnetograms have relatively poor resolution (~10"), satellite spots often remain invisible. The only clue for some disturbing agent is the vanishing penumbral structure or the complexity of the penumbral filament alignment. For example, Figure 5.7 gives the number of bomb locations and Ellerman bombs per sector of 20° within four arcsec on either side of the penumbra-photosphere border around the main spot of MW 18522 (4 Aug. 1971: 1311-1416 UT); the largest number of bombs and bomb locations (shaded) is found in the sector coinciding with

Figure 5.7. Distribution of bombs and of their locations along the penumbra-photosphere boundary of the main spot of MW 18522 (Figure 5.3); the number of bombs and of bombs locations (shaded) per sector of 20^{o} is graphed. Maximum corresponds to an area of disturbed and missing penumbra.

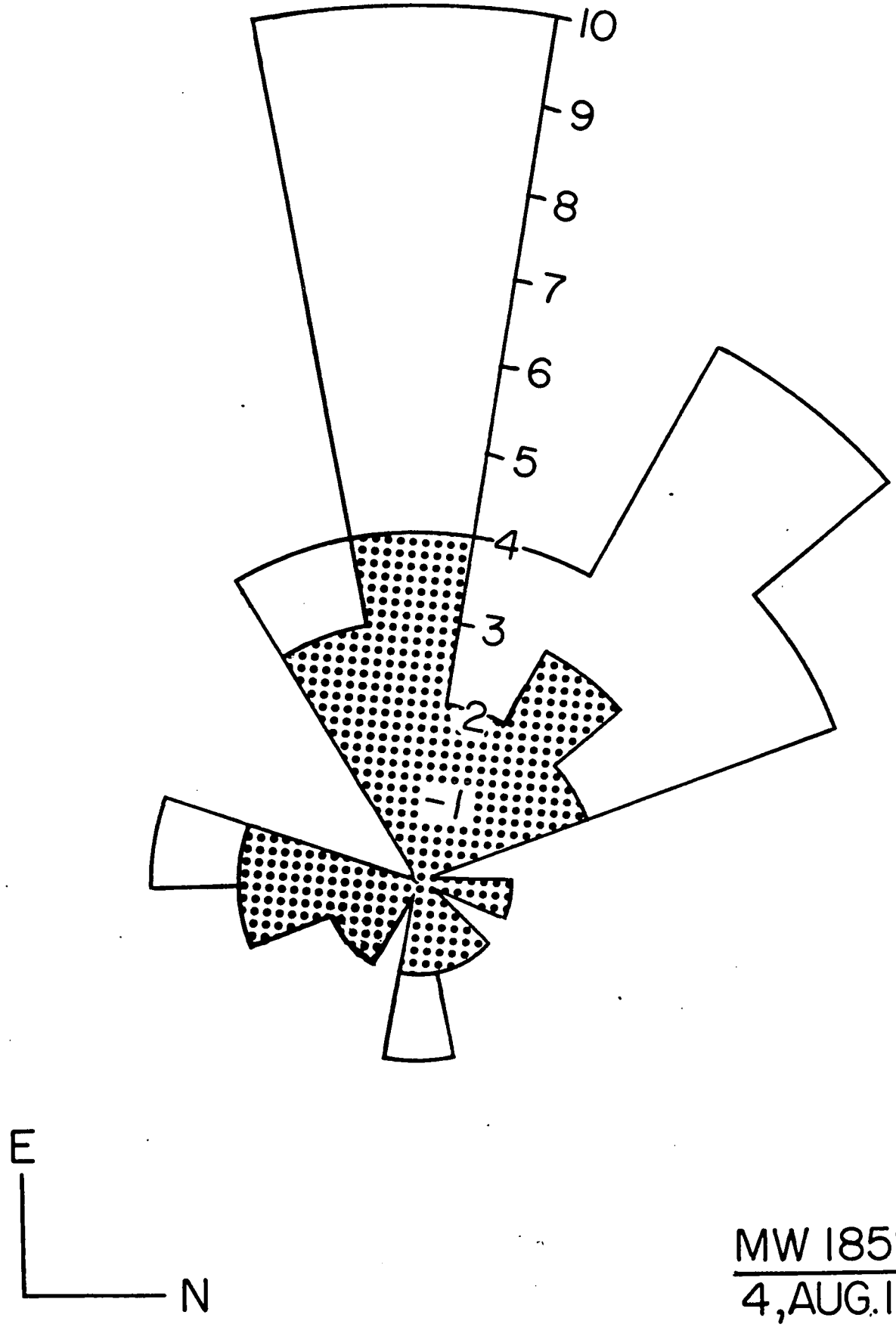

MW 18522
4, AUG. 1971

a portion of missing and disturbed penumbral filaments. The larger number of bombs with respect to bomb locations is due to the proliferation of homologous events. In Figure 5.9 of region MW 18538 (20 Aug. 1971), the penumbral filaments of the leading spot are parallel to the spot border instead of being oriented radially as usual; it may indicate some perturbing magnetic structure or velocity field perhaps related to the surge activity. Moreover, it may be a good case where the major change in field configuration affected the transverse component. Figure 5.8 shows the same region the day before; the surge bases then apparently do not coincide with any visible satellite spot. Comparison of Figures 5.8 and 5.9 reveals that the penumbral structure of the leading spot (northern side) evolved drastically.

Conversely, not every satellite spot shows activity. Some of them (in Figure 5.11, region E for example) are relatively inactive, indicating that a peaceful equilibrium has been established with the master polarity. Therefore, the existence of a satellite is not a sufficient condition for bomb and surge activity. As we will see, change in the surface flux appears to be required in the form of evolving magnetic structures. Naturally, young developing regions provide ideal conditions, explaining their well known association with surge production. Figure 5.10 shows a case among many of an arch filament system (AFS) in MW 18468 where I detected sporadic little surges along the same trajectories as the AFS; on 30 June, I detected seven

Figure 5.8. Region MW 18538 (E58 S13) on 19 August 1971. (i) Hα-5/8 Å, (first to the left), 1655 UT; (ii) Hα-2 Å, 1655 UT and (iii) Hα+5/8 Å, 1515 UT. North is at right; east is at top. Surges in their initial phase originating from the penumbral region in the leading spot (i) and at the end of a light bridge in the following spot (iii). There is hardly any sign of satellite spots at Hα-2 Å (ii). Notice the brightenings along the edges of the light bridge in the leading spot.

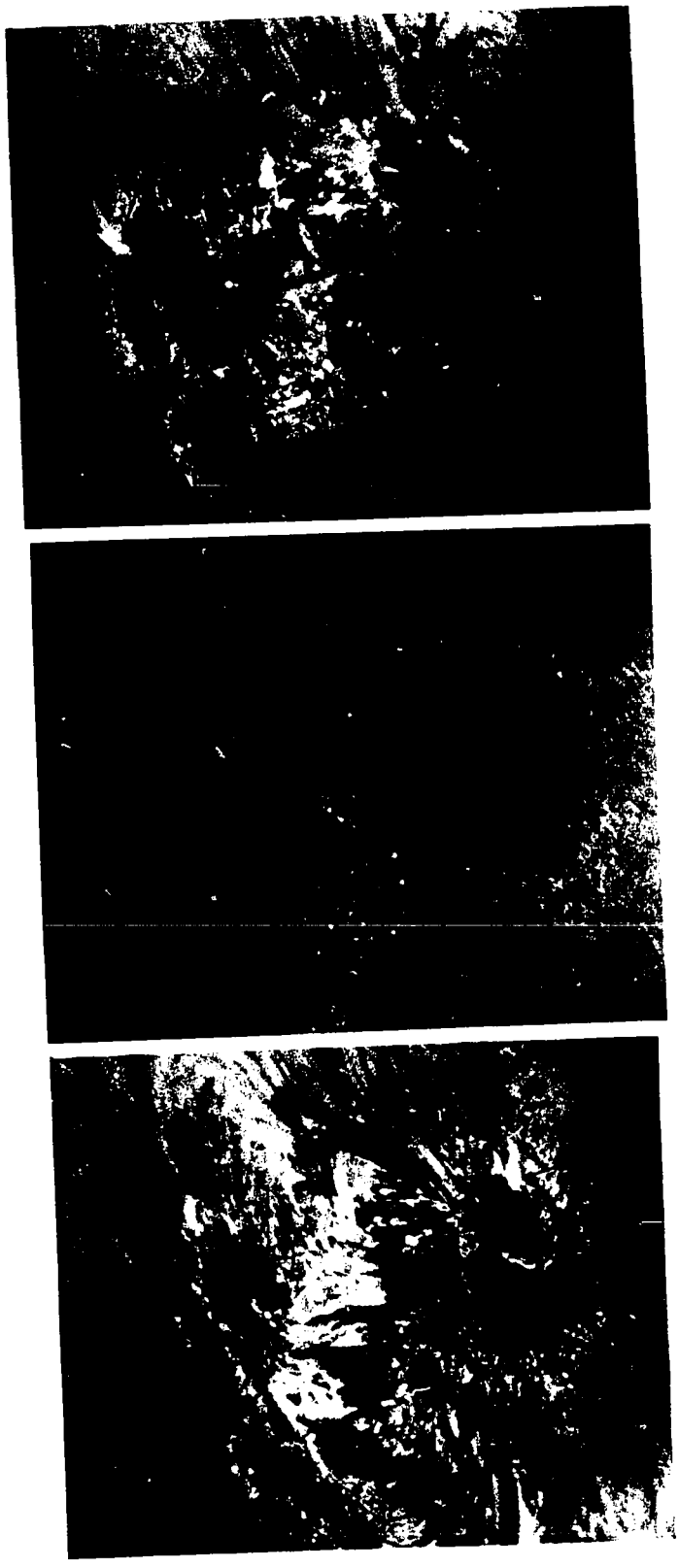

Figure 5.9. Region MW 18538 (E42 S13) on 20 August 1971, 1634 UT. The views are at Hα-1 3/8 Å (left) and -5/8 Å (right). The arrow points to penumbral filaments with an orientation making a sharp angle to the undisturbed radial direction at the base of ejections in the leading spot. The filtergram at -5/8 Å includes only the right end of the filtergram at -1 3/8 Å. The same region on the preceding day is shown in Figure 5.8.

Figure 5.10. Region MW 18468 (W27 N15) on 30 June 1971, 1559 UT. This view of the arch filament system (AFS) at Hα+5/8 Å shows some ejections (arrows) taking place along the dominant falling flow of the arch filaments. These little surges are easily detected because of their foot maximum visibility on the blue side of Hα contrary to the AFS feet.

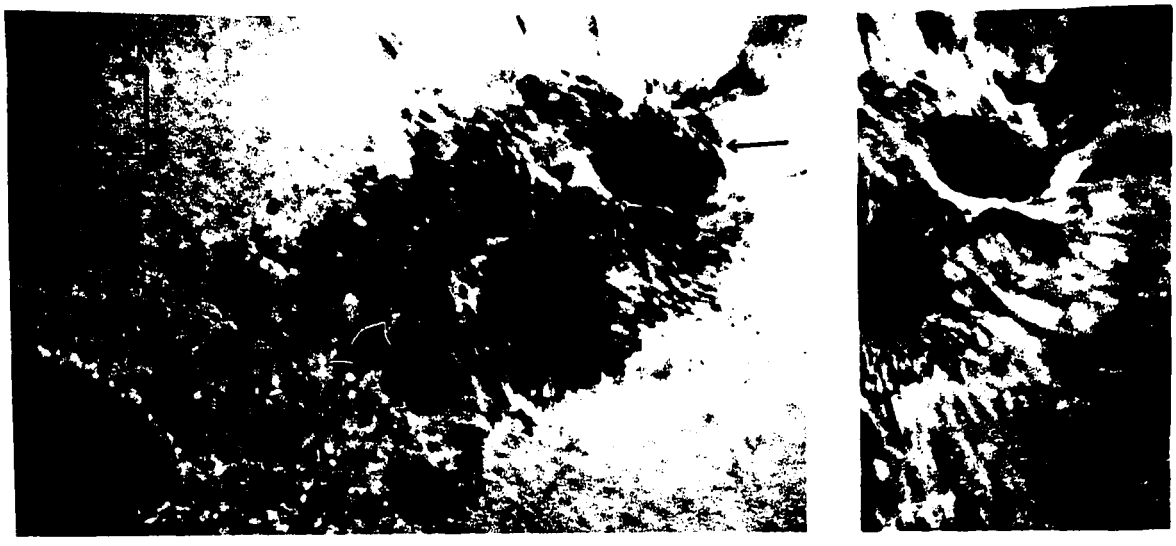


E

small bombs which were followed by ejecta over a period of only 34 min and on 29 June, 14 over 48 min.

Region MW 18594

Although some small surges are associated with AFS, I find a larger number of more spectacular ones near evolving satellite polarity coinciding with compact spots or pores; the epithet 'evolving' applies to an area showing magnetic flux change by a factor of 10 or more over a period of less than 24 hours.

The magnetic fjord of opposite negative (-) polarity intruding in the following parent positive (+) polarity of MW 18594 (Figure 5.11) was the site of many homologous surges on 23 Oct. 1971. Figure 5.12 displays phases of the activity observed in Hα between 1412 UT and 2100 UT. The off-band filtergrams taken at Hα-2 Å reveal the photospheric pattern. Some magnetograms for the same period are included in Figure 5.13; these maps are enlarged sections of the more complete maps such as the one of Figure 5.11 and show the satellite polarity and its immediate surroundings.

The satellite (-) pole, south of the big (+) spot, corresponds to the seat of bomb and surge activity. This island of negative flux coincides with pores which materialized in the photosphere earlier, between 1500 UT and 1900 UT; however, the magnetograph resolution is too low to decide which pore is which polarity. Hα filtergrams obtained around 1412 UT show some activity indicating that (-) flux has started to emerge, but none of the pore is yet visible.

Figure 5.11. Magnetogram of region MW 18594 (W05 N19) at 1918 UT on 23 October 1971. Contours levels are ±10 G, ± 20 G, ± 40 G, ... Solid contours enclose positive field; dashed contours enclose negative field. The box encloses the region shown at successive times in Figure 5.13. Circle D indicates the satellite polarity associated with bomb and surge activity (Figure 5.12). A, B, C and E represent regions used as comparisons in order to compare their flux time behavior with region D.

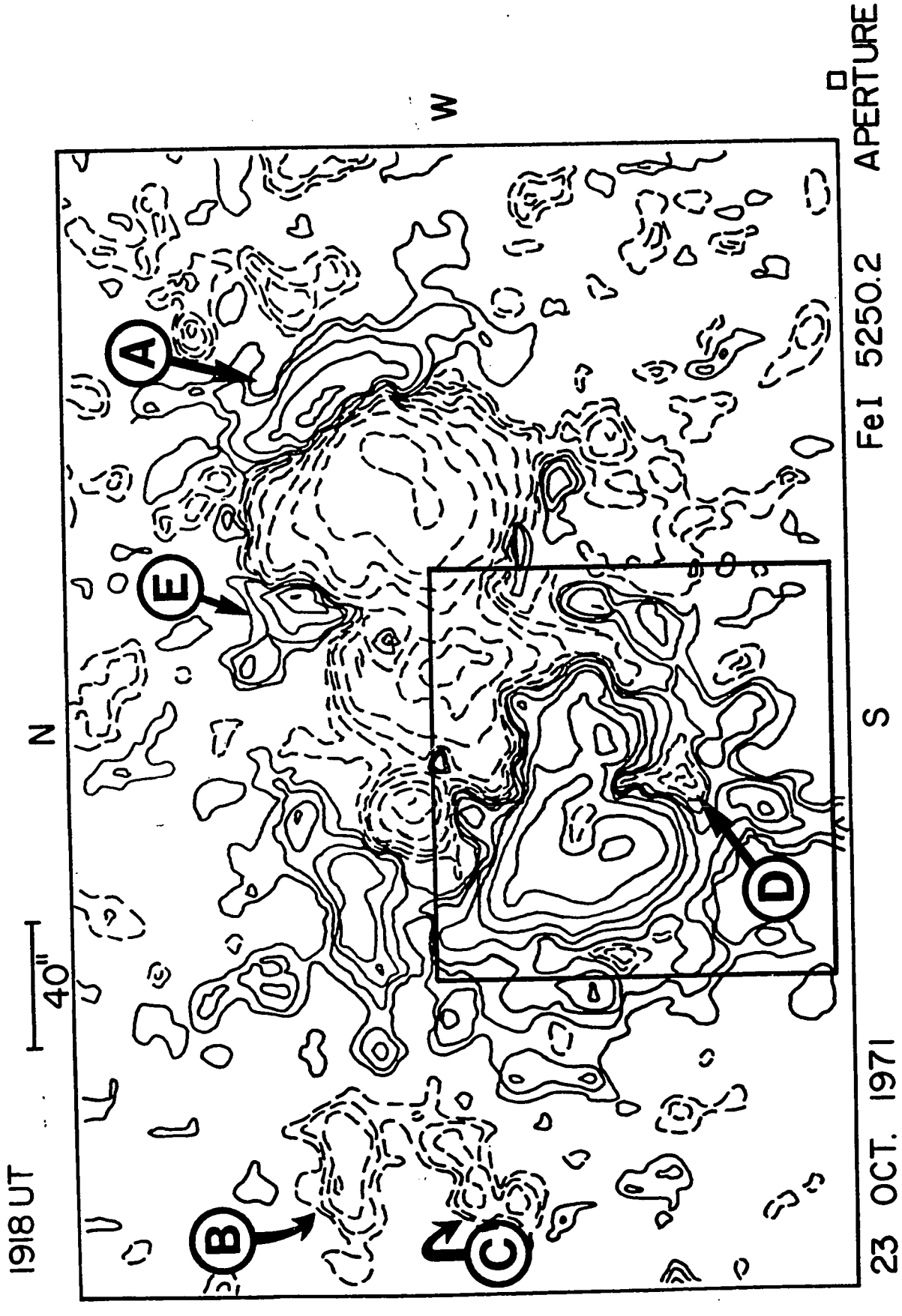
W
N
S
E
A
B
C
D
E
40"
1918 UT
23 OCT. 1971
FeI 5250.2
APERTURE

Figure 5.12. Bomb and surge activity in region MW 18594 on 23 October 1971. North is at top; east is at left. (i) Hα+1 3/8 Å, 1412 UT; notice the absence of the two tiny pores which have become visible in the later filtergrams at the seat of the bomb activity. (ii) Hα-2, -7/8 and ±0 Å, 1913 UT, shortly after the rapid ignition of a bright triangular bomb which develops into an extended surge seen later (1922 UT) at Hα-5/8 Å; notice in the frame at 1922 UT the fine thread structure connecting to the cluster of bombs. (iii) Hα-1 3/8, -5/8 and +5/8 Å, 2046 UT in the later phase of a successive event. A third pore (arrow) may have appeared in the interval following the preceding filtergram.

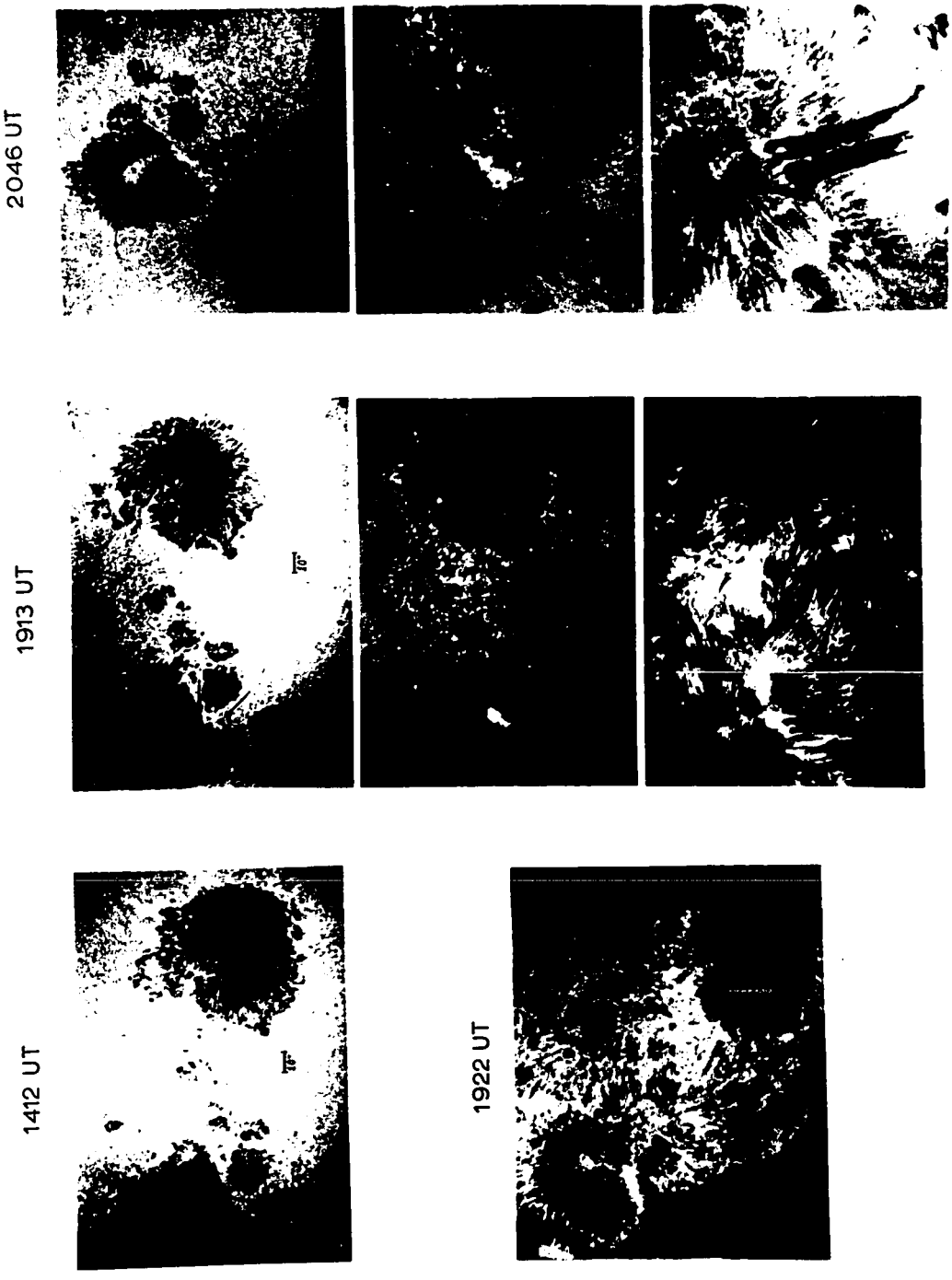
2046 UT
1913 UT
1412 UT
1922 UT

a

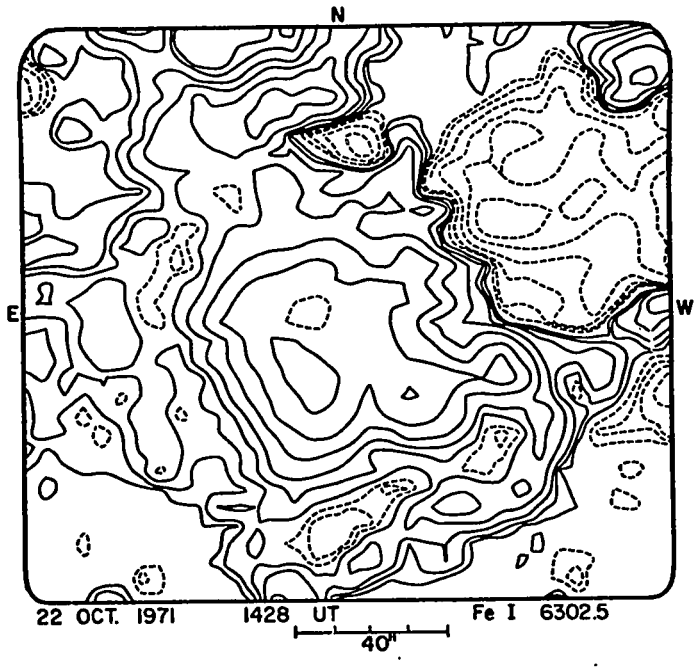

Figure 5.13. (a) Magnetogram of the following portion of MW 18594 (W07 N02) at 1428 UT on 22 October 1971 before the intense bomb and surge activity of the 23 October.

(b) Time sequence of magnetograms of MW 18594 on 23 October 1971 showing the boxed region of Figure 5.11 where activity is concentrated. Notice the weakening of the negative magnetic flux of the satellite polarity D. Contours follow the same conventions as Figure 5.11.

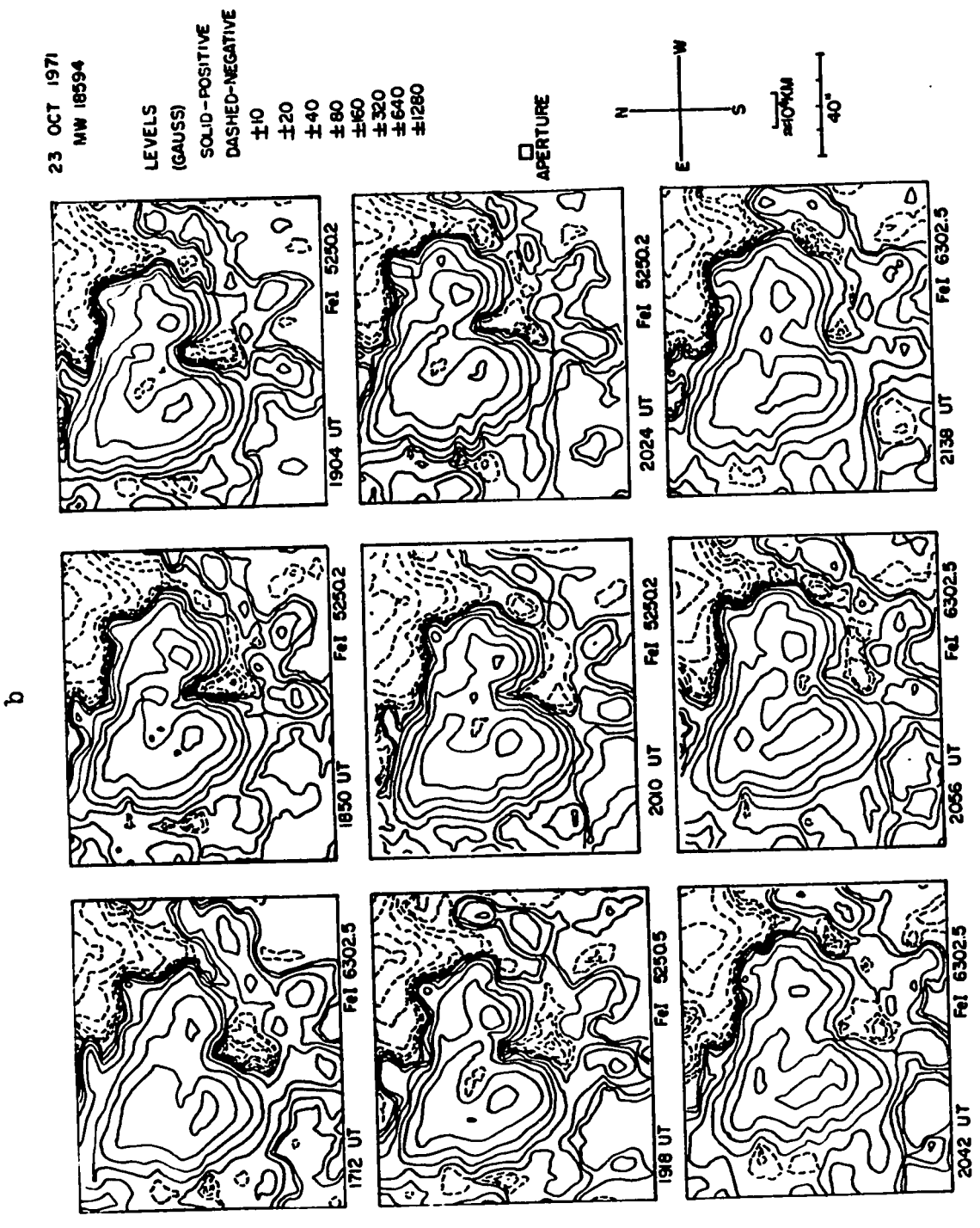
23 OCT 1971
MW 18594
LEVELS
(GAUSS)
SOLID-POSITIVE
DASHED-NEGATIVE
±10
±20
±40
±80
±160
±320
±640
±1280
APERTURE
N
S
E
W
≈10^4KM
40"
1712 UT
FeI 6302.5
1850 UT
FeI 5250.2
1904 UT
FeI 5250.2
1918 UT
FeI 5250.5
2010 UT
FeI 5250.2
2024 UT
FeI 5250.2
2042 UT
FeI 6302.5
2056 UT
FeI 6302.5
2138 UT
FeI 6302.5

b

The magnetograms of Figure 5.13 show the size and strength of the (-) satellite pole D (Figure 5.11) dwindling with time. Figure 5.14 gives the value of the flux with respect to time of the satellite D located at the bomb site in MW 18594; as comparison, the fluxes of four other poles identified as A, B, C and E on the magnetic map of Figure 5.11 are given. These apparently stable comparisons were chosen because the magnitude of their perturbation in the surrounding field is similar to region D.

The field intensity between contour levels i and i+1 is by definition, $B_i < B \leq B_{i+1}$, where $B_1 = 10$ G, $B_2 = 20$ G, $B_3 = 40$ G, etc. The flux corresponding to the longitudinal component of a feature of area A is given by

$$F = \int_A B_\ell \, ds \qquad 5.1.$$

I have approximated the average flux over the area enclosed by two adjacent contours where A_i is the area enclosed by the i^{th} contour, by

$$F_i = A\left[(i+1)-i\right] \times \frac{B_i + B_{i+1}}{2} \qquad 5.2.$$

Therefore, the total flux through an area of one polarity is

$$F = \sum_i A\left[(i+1)-i\right] \times \frac{B_i + B_{i+1}}{2} \qquad 5.3.$$

While the absolute value of the magnetic flux in the comparisons stayed roughly the same at about 50×10^{19} Maxwells (Mx) in region A, and about 16×10^{19} Mx in regions B, C and E, it droped from 2.8×10^{19} Mx to no measurable flux in region D within three hours. This

Figure 5.14. Time behavior of the positive flux in comparison region A and E, of the negative flux in comparison regions B and C and of the negative flux in the satellite region D (regions located in Figure 5.11) of MW 18594 on 23 October 1971. The phase of the main bomb flashes recorded between 1900 and 2100 UT is shown. The error bar results from the imprecision in evaluating the surface enclosed by isogauss lines. Notice change of scale between top and bottom parts of the figure.

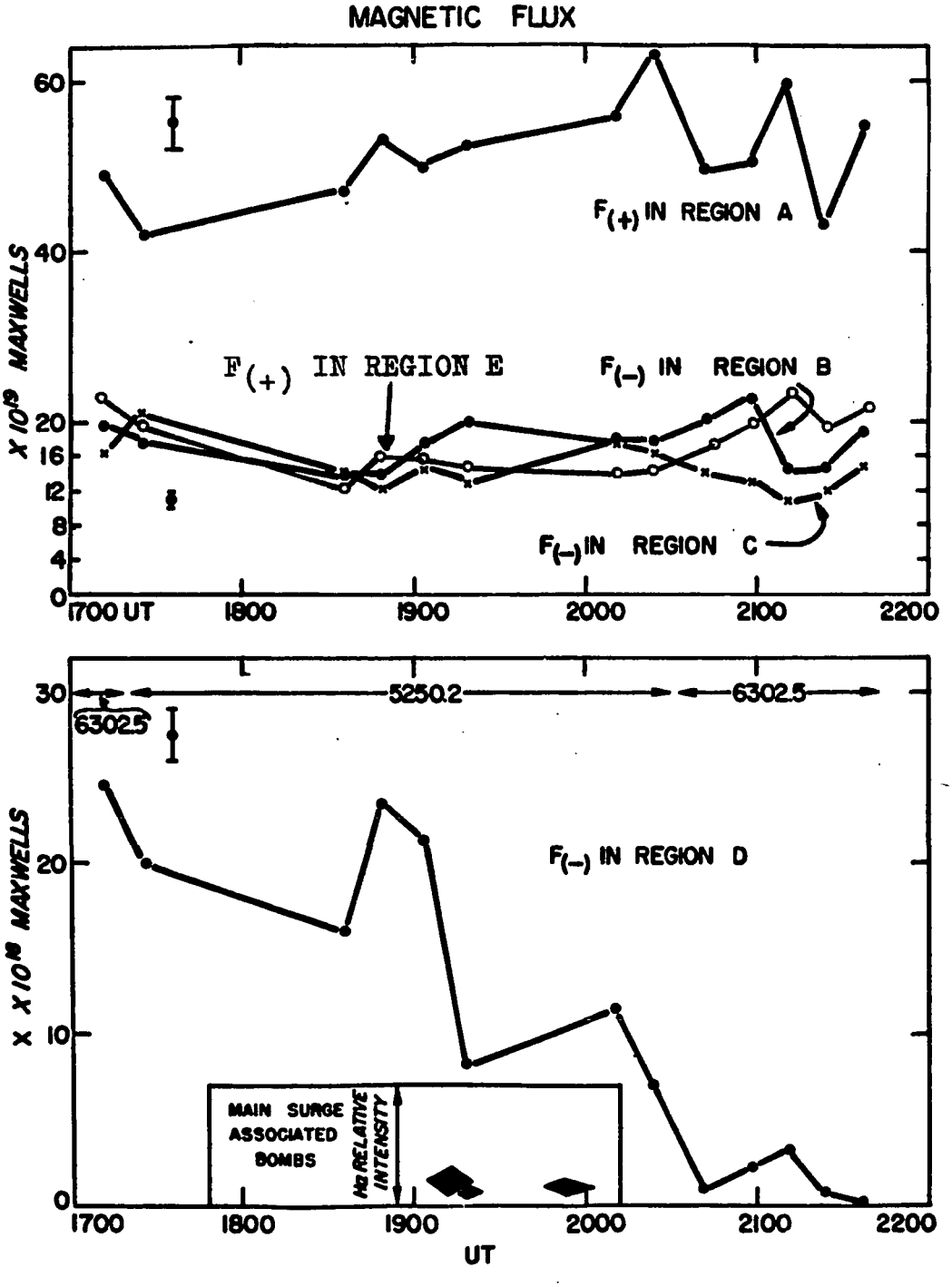
MAGNETIC FLUX
60
40
20
16
12
8
4
0
X 10^19 MAXWELLS
F(+) IN REGION A
F(+) IN REGION E
F(-) IN REGION B
F(-) IN REGION C
1700 UT
1800
1900
2000
2100
2200
30
20
10
0
X X 10^18 MAXWELLS
5250.2
6302.5
6302.5
F(-) IN REGION D
MAIN SURGE ASSOCIATED BOMBS
Hα RELATIVE INTENSITY
1700
1800
1900
2000
2100
2200
UT

corresponds to a changing rate of 3×10^{15} Mx/s. The change measured in region D is only 5% of the flux in region A, and 20% of the flux in regions B, C and E. Figure 5.14 shows that the flux in region A did stay constant only within 20×10^{19} Mx. Between 1900-2200 UT, the flux stayed constant within $2\text{-}3 \times 10^{19}$ Mx in region C and increased by about $4\text{-}6 \times 10^{19}$ Mx in regions B and E. Seeing smearing may be responsible for part of the flux weakening in region D. Since a parallel increase in flux is measured in regions B and E, the dissolution of the satellite spot D is probably real. The last map in Figure 5.13 b at 2138 UT shows at the satellite location a relaxed configuration not unlike the one at 1428 UT on 22 Oct. 1971, the day before (Figure 5.13 a).

From the quality of filtergrams made simultaneously to the magnetic maps, it appears that the seeing quality was fair over the observatory; off-band Hα views show the granulation implying that the seeing disk was then probably smaller than the magnetograph scanning aperture of 5"x5". Despite possible smearing by seeing and problems discussed in section 3.2, I consider that the series of magnetograms of Figure 5.13 represent a candidate for a relationship between activity and magnetic flux variations.

Figure 5.15 gives the value of the longitudinal field along a roughly north-south line passing through the satellite polarity. The rather sharp (+) peak south of the satellite remains identical throughout the sequence,

Figure 5.15. Time behavior of the longitudinal field component versus position along a roughly north-south line crossing the evolving (-) satellite polarity south of the parent (+) spot in Figure 5.13b. The shaded area represents the negative field of the satellite.

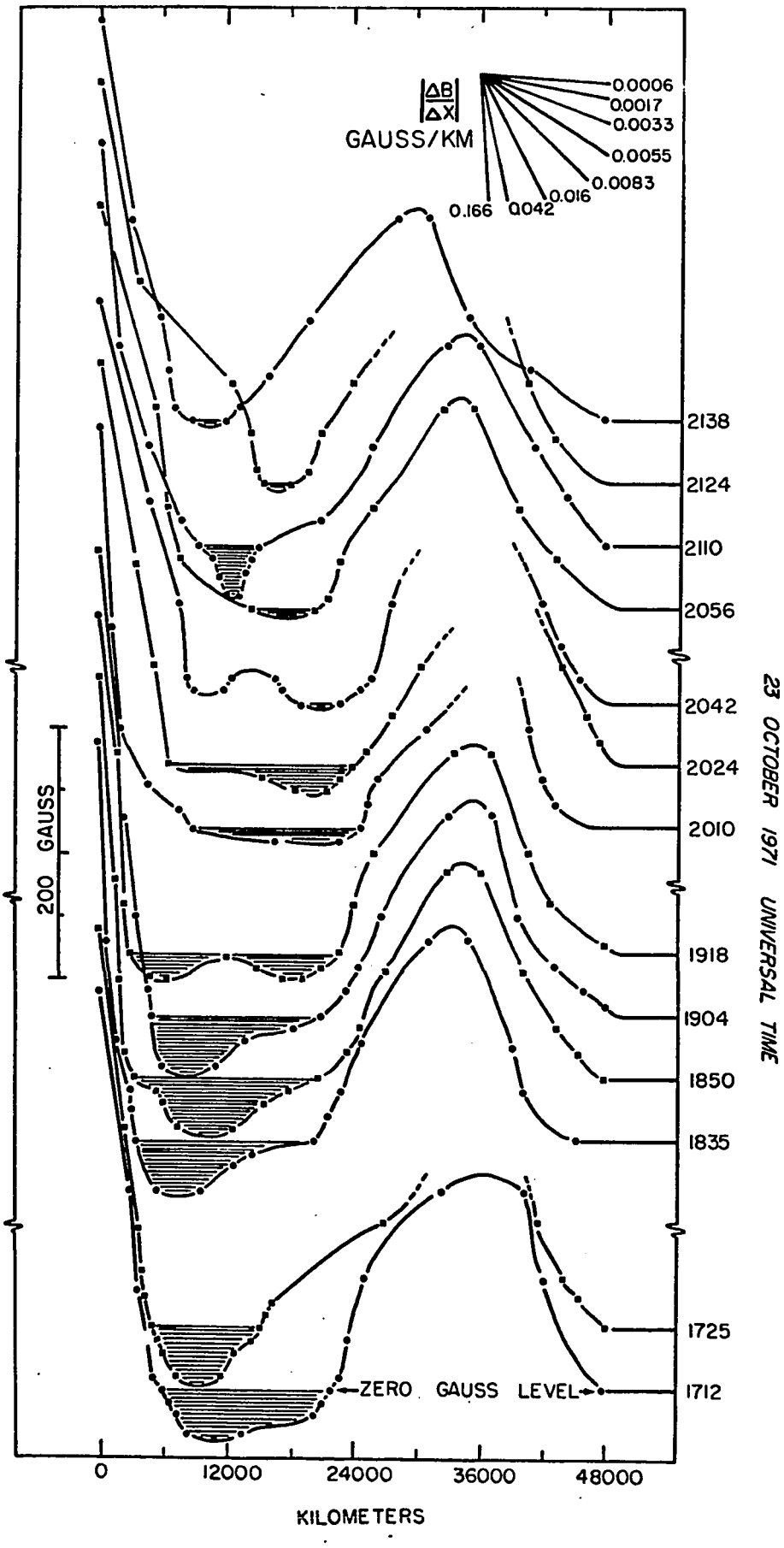
|ΔB/ΔX|
GAUSS/KM
0.0006
0.0017
0.0033
0.0055
0.0083
0.016
0.042
0.166
2138
2124
2110
2056
2042
2024
2010
1918
1904
1850
1835
1725
1712
200 GAUSS
ZERO GAUSS LEVEL
0
12000
24000
36000
48000
KILOMETERS
23 OCTOBER 1971 UNIVERSAL TIME

except for 5 maps (1725, 2010, 2024, 2042 and 2124 UT) where seeing might have smeared it. The distribution of the longitudinal field as a function of position shows more clearly than maps the slow dissolution of the recorded (-) flux as time goes on. Since the identation in the (+) region remains strong, it means that smaller unresolved tiny (-) features may still be present but weaker. At the top of Figure 5.15, I have indicated the values of the longitudinal field gradient in G/km corresponding to the different slopes in the graph B_ℓ vs position. The field gradient on the side of the big spot north of the satellite gets smaller with time; it corresponds to the location of most intense bomb activity. It also reflects the weakening of the (-) inclusion followed by the straightening of the boundary neutral line. Finally, strongest support for possible change comes from the appearance and increase in size of pores, between 1400-2100 UT. This brings evidence without which magnetograms would have only a marginal value in demonstrating rather small scale change over a period of a few hours.

The following spot of MW 18594 shows a subflare accompanied by surge ejections on 19 Oct. 1971 (Figure 5.16). Comparing the magnetograms of 19 and 20 Oct., one sees that in the magnetic depression of the local (+) field, new flux has made its way to the surface. Table XIII summarizes data on four evolving satellite magnetic structures associated with bomb and surge production; the reader should refer to Table VII for more details on the activity.

Figure 5.16. Magnetogram of region MW 18594 on 19 October (E26 N10) and 20 October (E17 N10) 1971. The shaded area on 19 October corresponds to a subflare with surge activity overlapping a developing satellite polarity. Contours follow the same conventions as Figure 5.11.

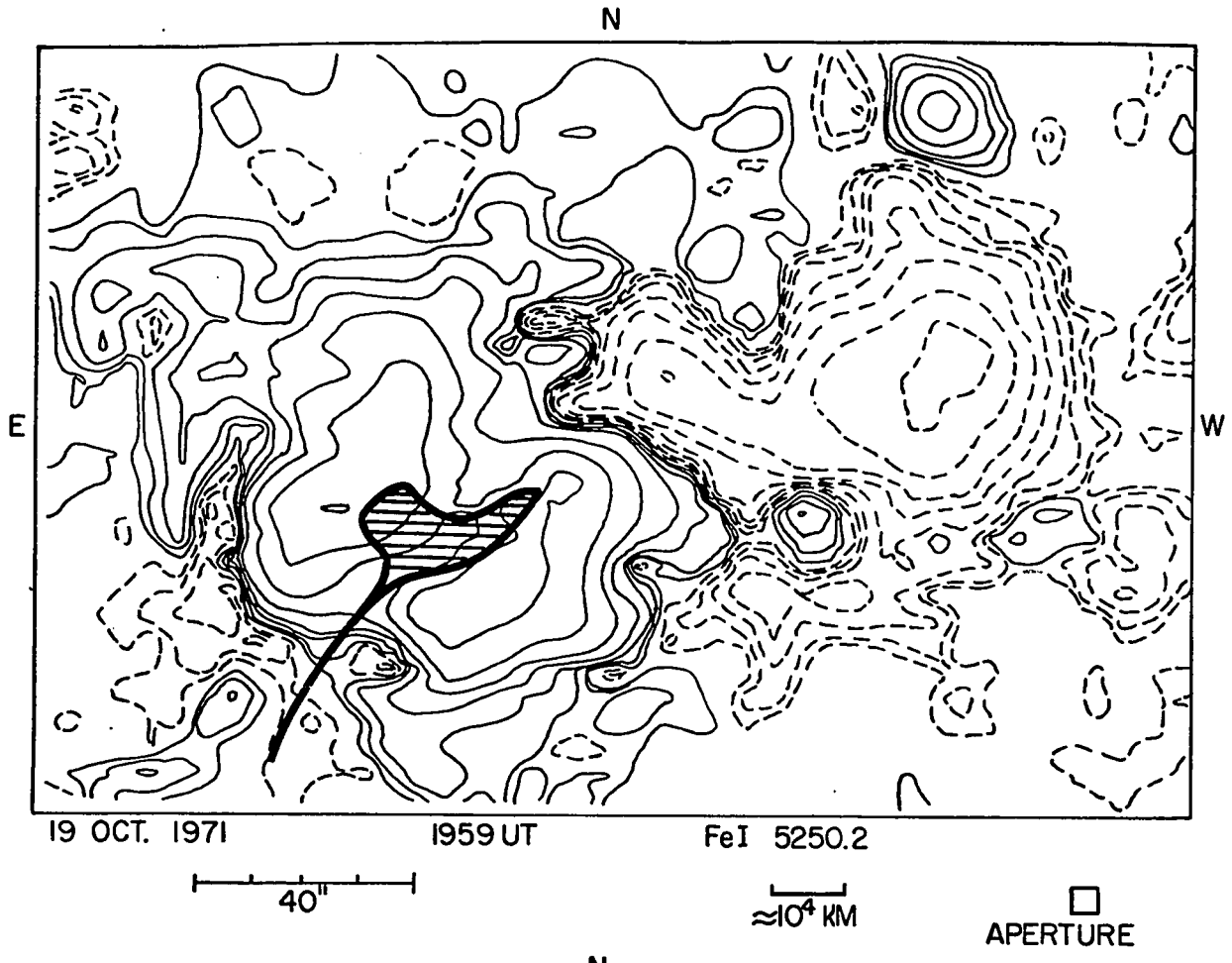
N
E
W
19 OCT. 1971
1959 UT
FeI 5250.2
40"
≈10⁴ KM
APERTURE

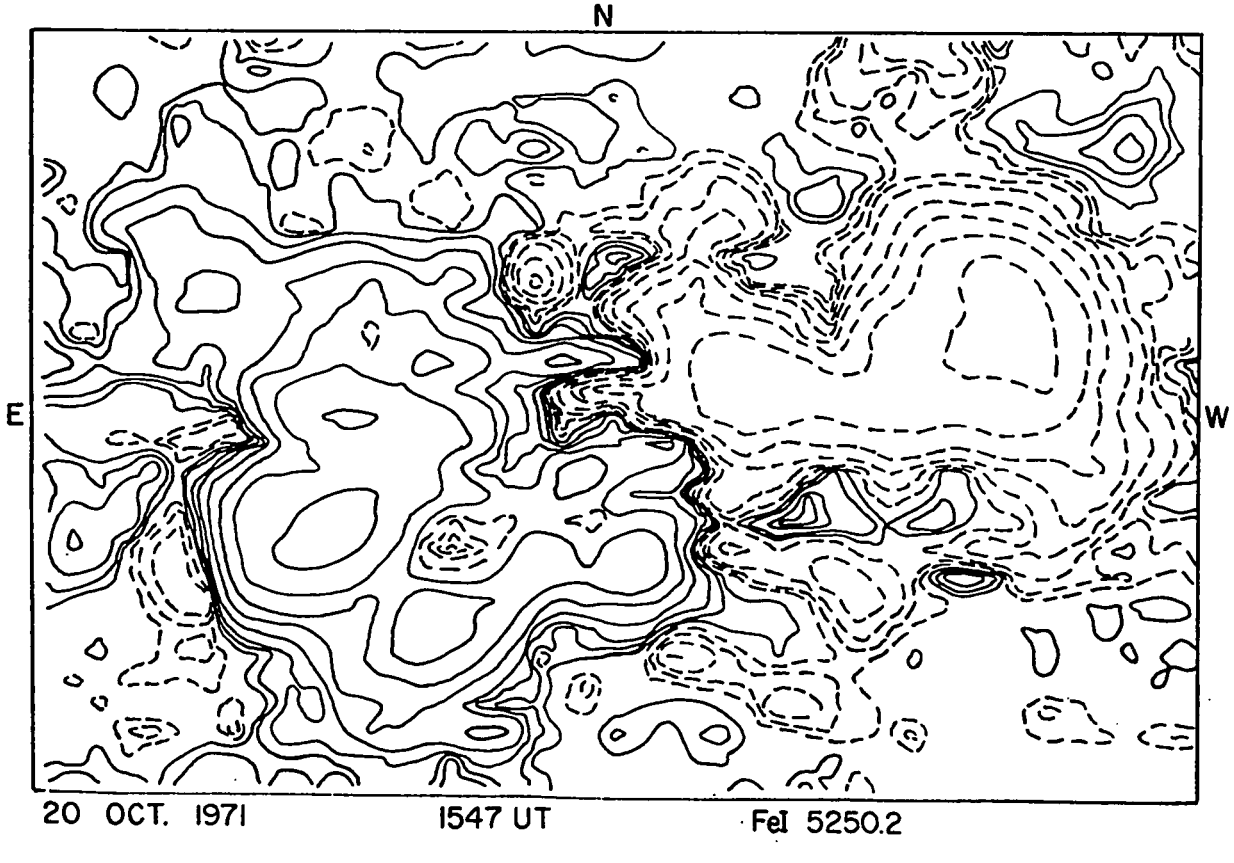
N
E
W
20 OCT. 1971
1547 UT
FeI 5250.2

Table XIII

Evolving magnetic structures

Mt Wilson region	Initial size of satellite (arcsec)	Date 1971	ΔF (Mx)	$\Delta F/F$ (%)	Δt (hrs)	$\Delta F/\Delta t$ (Mx/s)	Emf (V)	Remarks
18594	10	19/10 20/10	0.6×10^{19}	100	20	10^{14}	10^{6}	Comparison of two selected maps at 5250.2 Å. (*)
18594	12	23/10	2.5×10^{19}	100	3	3×10^{15}	3×10^{7}	Flux measured from 13 maps at 5250.2 and 6303.4 Å. (*)
18511	20	31/7 01/8	11×10^{19}	90	24	1.3×10^{15}	1.3×10^{7}	31/7: average of 4 maps at 6303.5 and of one map at 6332.7 Å. 01/8: average of 2 maps at 6332.8 Å. Surges within 10" of evolving satellite flux values based on changes in pores: 2 pores with area of 20 arcsec^2 with max. field of -1400 G evolved into 6 pores (14 arcsec^2, max. field -1000 G)
18468	10 (pores)	29/6 30/6	7.5×10^{19}	50	24	10^{15}	10^{7}	

(*) Surge and bomb activity overlying the region of evolving magnetic satellite polarity.

Table XIV gives the magnetic gradient near surge bases deduced from magnetic maps available at about the time of bomb-surge occurences. From these fragmentary data, no definite statement can be made about the behavior of gradients except for what I said about the well documented case of the 23 Oct. 1971 homologous surges in MW 18594 (Figure 5.15). The first three cases in Table XIV refer to events maybe originating in magnetic structures much smaller than the magnetograph resolution. On the other hand, the value of the gradient may have nothing to do with surge occurence; the figures themselves given in the table can be found on any magnetic map of active regions with no surge occuring near them. However, in three out four cases, the gradient along a line going through the surge base is stronger than along a line through a location 5" away on either side of the surge base. The existence of a very steep gradient on a scale of the order of 100 km cannot be ruled out.

Region MW 18468

Not related to any satellite spot as such, the disk surge which occured in region MW 18468 on 29 June 1971 featured activity associated with evolving magnetic structure. The non-availability of magnetic maps brought me to inspect sunspot pictures which revealed changing magnetic fields. Figure 5.17 displays Hα filtergrams of the event at 1551 UT, six minutes after subflare maximum.

Table XIV

Magnetic gradient at surge bases *

Mt Wilson region	Time of magnetogram	Importance of surge	Gradient	length of baseline used	Gradient steeper than surrounding	Evolving flux associated
18511	7/31/1971 1501 UT	S	0.011 G/km	5400 km	Same	Yes
18594	10/20/1971 1547 UT	S	0.055 G/km	6000 km	Yes	No
18594	10/21/1971 1442 UT	S	0.08 G/km	4800 km	Yes	Insufficient data
18594	10/23/1971	2	0.10 G/km	5000 km	Yes	Yes

* Resolution of magnetic maps used: 5" ≈ 3600 km.

Table XV

Surge base distance of nearest active features (arcsec)

Surge 1971	Mt Wilson region	From edge of pore	From penumbra photosphere border	From light bridge	From Photos. network
6/29	18468	3			
6/29	18479	4			
6/30	18468	4			
7/25	18511			1	
7/31	18511	1-4			
8/4	18522	2	7		3
8/19	18538		2		
10/19	18594		2		
10/20	18594		2		
10/21	18594		2		
10/23	18594	2-4	2		

Figure 5.17. Filtergrams of region MW 18468 (W13 N15) at 1551 UT on 29 June 1971. This is a typical eight-frame sequence obtained by stepping the filter passband across the Hα profile through -2, -1 3/8, -7/8, -5/8, ±0, +5/8, +7/8 and + 1 3/8 Å in 20 sec. The sequence shows the complex differential dynamics of the surge constituent threads. North is at top; east is at left.

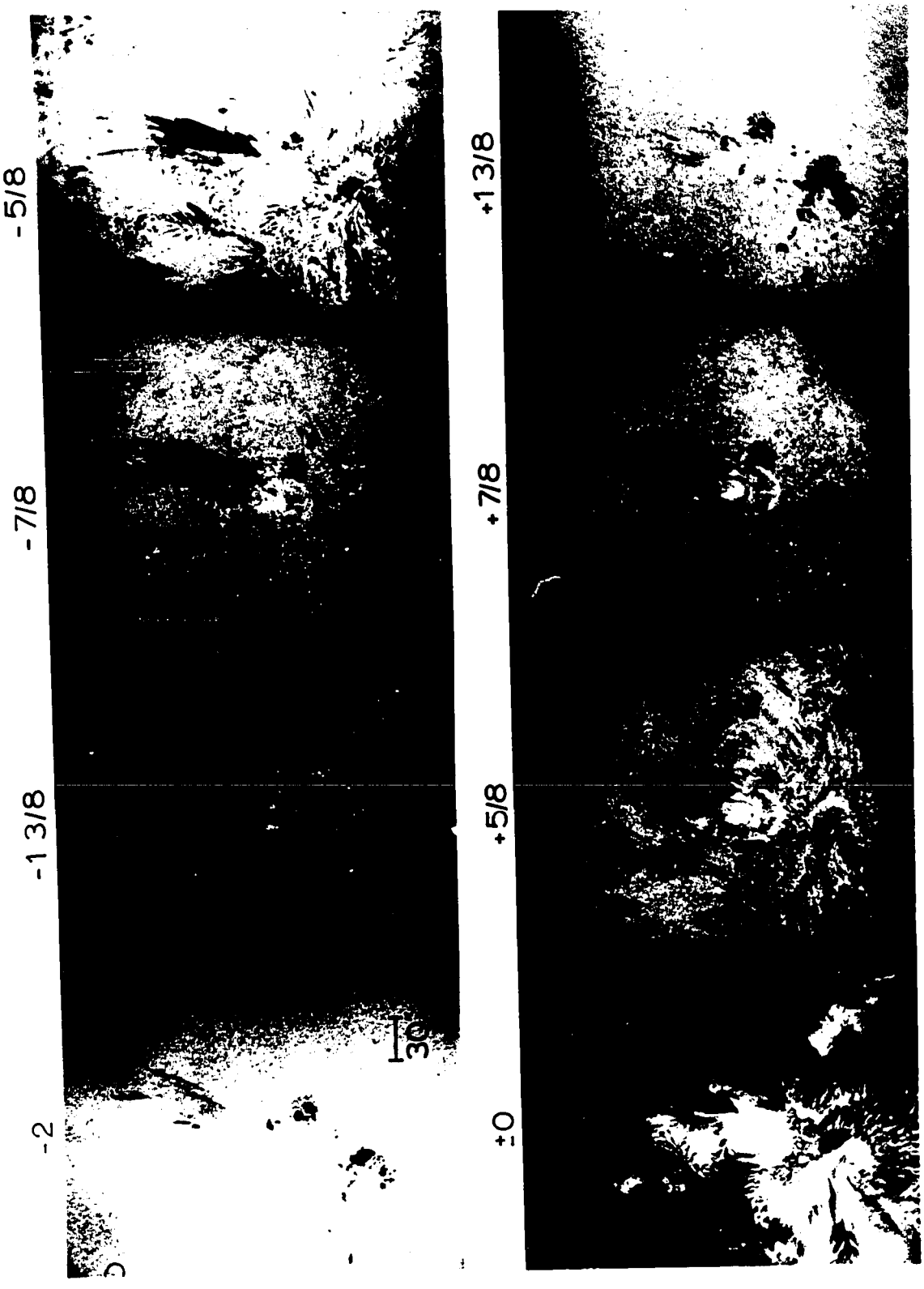
-2
-1 3/8
-7/8
-5/8
30
±0
+5/8
+7/8
+1 3/8

The horseshoe-shaped brightening, characterized by two intense kernels at either end, is still visible. The large surge originates at the one end of the brightening located near two small (-) pores. Although the flare encompasses a rather large area of the chromosphere, the most conspicuous ejective flow appears within 4" of the small pores. Study of the original 35 mm and of the 16 mm cinematographic copy reveals that each dark thread connects back to the surface at a bomb-like feature. The movie also discloses tiny ejections above the eastern kernel of the flare, where the Hα-2 Å (Figure 5.17) shows five tiny pores, having (+) polarity on Mt Wilson sunspot drawings; the ejections look poorly contained and their flare brightness implies high densities or temperatures.

Inspection of Mt Wilson sunspot drawings of MW 18468 discloses the sunspot evolution on 29-30 June in the area where the flare and surge took place; the point of maximum flare brightness on 29 June lies over an area of increasing (+) flux (1000 G up to 1800 G) while the two (-) spots between which most of the surge filaments were anchored, show sizeable shrinking and drop in intensity (-1400 G down to -1000 G) (Figure 5.18). The Hα filtergram (Figure 5.17) reveals in the region of the subflare the typical disturbed chromospheric structure associated with emerging new flux of opposite polarity.

5.2.2 SURGE ACTIVITY IN LIGHT BRIDGES

Surges originating from inside spots took place along

Figure 5.18. Filtergrams of region MW 18468 on 29-30 June 1971 at Hα-2 Å. Magnetic field values in hundreds of Gauss are from Mt Wilson sunspot visual field measurements and refer to maximum intensity. 29 June (1551 UT) is at top; 30 June (1554 UT) is at bottom. North is at top; east is at left. The dotted line is the position of the dividing line (neutral line) between positive and negative magnetic fields in the region as extrapolated from the sunspot field measurements and the chromospheric structure at H$\alpha\pm$0 Å.

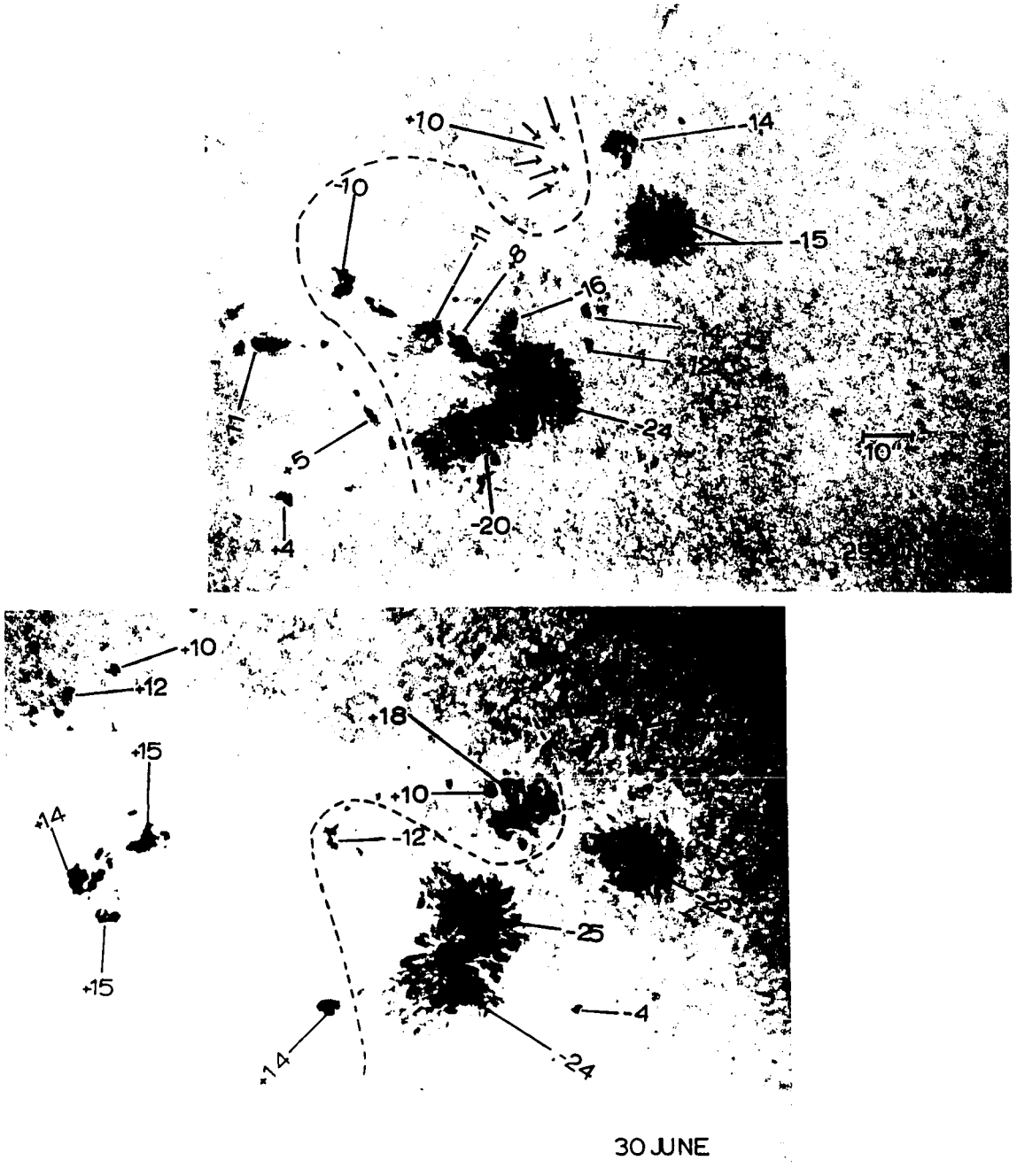

30 JUNE

light bridges; not a single case arose directly from the umbra. Although they rarely produce spectacular events, some light bridges are apparently rich producers of brightenings followed by ejections of all sizes. Table XVI lists cases of regions where bomb-surge events arise along light bridges. The reader is referred to Table VII for more details.

Table XVI

Surge activity in light bridges

Region	Date	Surge importance
MW 18235	12/6/1970	1
MW 18235	12/7/1970	1
MW 18511	7/25/1971	2, 1
MW 18538	8/19/1971	1
MW 18538	8/20/1971	S
MW 18594	10/27/1971	S

Region MW 18511

Because of its well-defined behavior, I describe the activity in MW 18511 in some detail. The region kept about the same spot configuration for all the time it spent on the disk. Nevertheless, activity happened in the neighborhood of the double umbra spot (+) during disk passage. The surrounding area was dominated by the appearance and disappearance of many pores every day between 25-31 July 1971. On 25 July, there was intense surge activity along the light bridge which splits the spot. A veil of surges (Figure 5.19) shot up from the eastern edge of the light

Figure 5.19. Filtergrams of region MW 18511 (E62 S15) at 1518 UT on 25 July 1971. Views are at Hα-2 (at left), -7/8 and -5/8 Å. North is at right; east is at top.


0001
1100
1100

bridge. Between 1500-1715 UT, six bursts of arrowhead-shaped brightenings, only a few thousands km long were seen as far as Hα-2 Å; out of them, bright but mostly dark filaments stretched out above the double umbra. Curiously most surge-generating bombs (~80%) appeared along the edge of the light bridge adjacent to the umbra with the strongest field, although all bombs were seen at various places along both edges of the bridge. At times, more than a dozen bombs decorated the edges. Around 1540 UT, a brief brightening appeared along the chromospheric structure connecting the bridge to the eastern portion, which the Mt Wilson large scale magnetogram indicates as (-) polarity. On 26 July, three pores of (-) polarity with maximum field strength of -800 G had emerged east of the double umbra spot.

5.2.3 A CASE OF ERUPTIVE FLARE: MW 18522

A most disturbing fact about surge and spray production is provided by region MW 18522, which produced five flares on 3 Aug. 1971: 1355, 1550, 1857, 1913 and 1928 UT. I recorded completely the first event which occured just ahead at the single visible sunspot of the region and which was accompanied by a spectacular eruption (Figure 5.20) fulfilling most of the characteristics of flare sprays stated by Smith (1968). Later events were similar although less grandiose. The point to stress is that absolutely nothing peculiar is noticeable in the spot on 3-4 Aug. 1971 when the center produced eruptive flares like a machine gun! It implies that very small scale

Figure 5.20. Filtergrams of a flare spray in its initial phase in region MW 18522 near the limb (E77 S10) on 3 August 1971 (1406 UT) at Hα-7/8 (top) and Hα±0 Å (bottom).

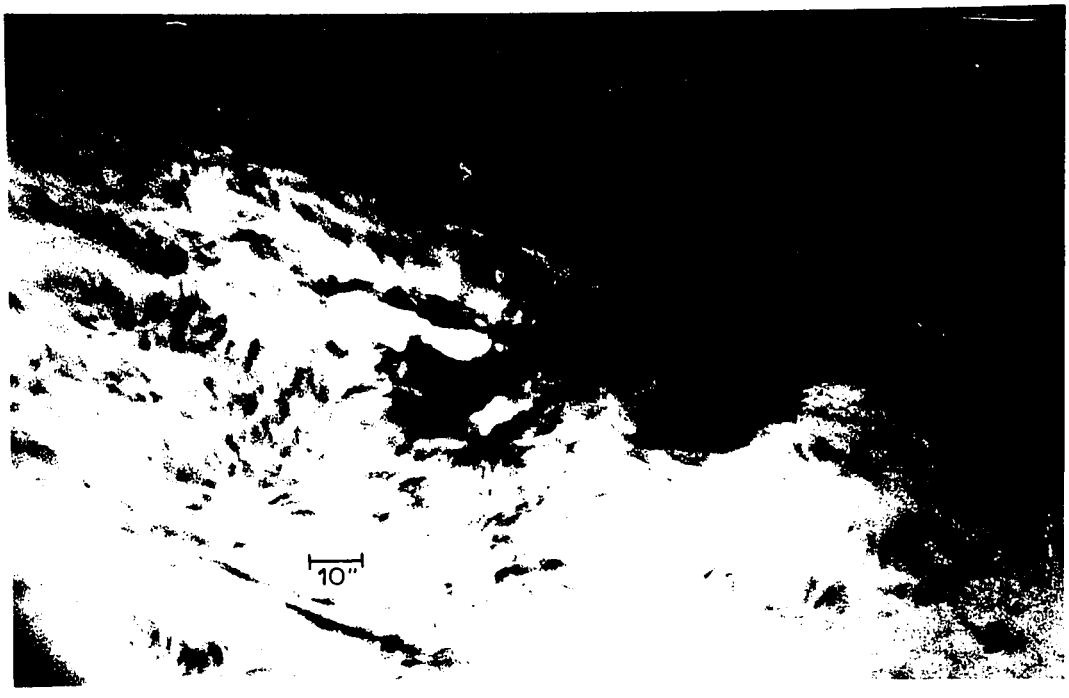
10"

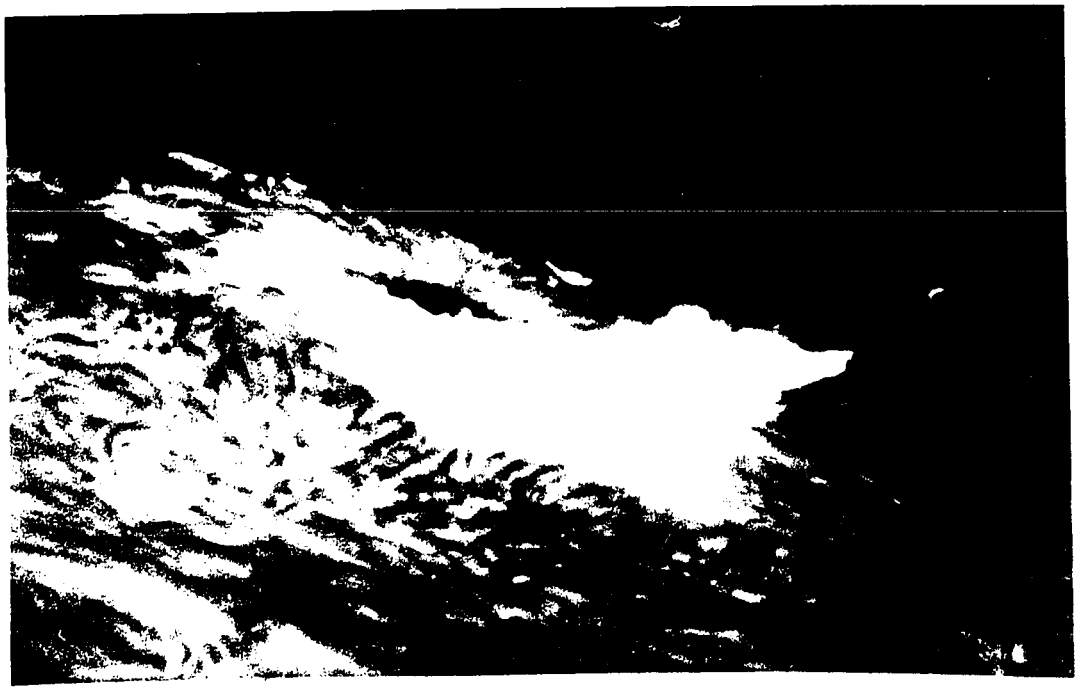

features (< 200 km) may trigger major perturbations, or that ejection of material from flares, such as sprays, has nothing to do with magnetic satellites at all.

Summarizing the material presented so far, one sees that surges and their associated bombs originate very near the boundaries of strong magnetic field concentrations. In cases where detailed magnetic mapping is available, magnetic flux changes were seen to occur at an average rate of about 10^{15} Mx/s over area roughly 10^{4} km across.

5.3 LINES OF FORCE

I computed magnetic lines of force using the Schmidt analysis (Schmidt, 1964) of the potential field approximation; the method has been described in detail by Rust (1966, 1970), Harvey (1969), Rust and Roy (1971) and Roy (1971, 1972). The Schmidt analysis, which assumes that there exists no electric current above the photosphere, computes magnetic field intensities above the photosphere by taking the measured longitudinal component of the field near the center of the disk as a boundary condition. Each point of the magnetic map corresponds to a unique fieldline which is integrated from the equation $\underset{\sim}{B} \times d\underset{\sim}{s} = 0$, where $d\underset{\sim}{s}$ is an element of length along the line. Fieldline calculations are intended to test whether the current-free approximation remains valid in evaluating coronal fields when surges take place. It also provides a rough estimate of the field intensity at various distances

along the surge trajectory (but maybe not in the surge material itself). Moreover, calculated fieldlines proved to be an almost indispensable tool for constructing the corrected space geometry of surge trajectories. Footpoints for computed fieldlines are set on the magnetograms to coincide with the observed bases of surge filaments.

Generally, the surge filaments follow closely trajectories determined by the magnetic lines of force computed from a potential field (Table XVII); this confirms the results of Rust (1968) and Harvey (1969) and indicates that the current-free analysis is an adequate tool to investigate coronal magnetic fields; if the current-free fieldlines nearly fit the trajectories of surges, the true fieldlines cannot be much different in shape. At low heights (<5000 km) calculated fieldlines fail to match the complex structure of the surge material which appears in emission. This is probably due among others to the following causes:

(1) The computation method assumes a flat distribution of monopoles situated at the photospheric level; in reality, one should expect to have sources in the chromosphere which violate the approximation (Dravins, 1972).

(2) The low resolution of the magnetic map smooths out small-scale features; this leads to calculated lines of force less intricate than the real ones must be. At heights greater than 10^4 km, the field configuration is mostly determined by the strongest features of the underlying spots (Rust and Roy, 1971) and agreement is fair.

Table XVII

'Current-free' lines of force and surge trajectories

Mt Wilson Region	Time of magnetogram	Center of magnetogram	Line FeI	Surge activity	Quality of fit	Comments
18511	7/29/1971 1759 UT	E15 S15	6302.5	7/25/1971 1518-1739 UT	Excellent Fig. 5.21	Shape, inclination, direction of surge are matched.
18511	7/31/1971 1501 UT	E08 S08	6336.8	7/31/1971 1300-1540 UT	Good & failed	Half of filaments matched correctly; remaining threads point 180° away from direction of computed fieldlines.
18594	10/20/1971 1547 UT	E17 N10	5250.2	10/20/1971 1935 UT	Excellent Fig. 5.22	Same comment as for MW 18511, 7/25/1971 surges.
18594	10/21/1971 1442 UT	E07 N03	6302.5	10/21/1971 1450 UT	Excellent	Same comment as for MW 18511, 7/25/1971 surges
18594	10/23/1971 1918 UT	W20 N08	5250.2	10/23/1971 1900-2055 UT	Good Fig. 5.23	Agreement is good except for deviation of 10-15° between filaments and computed fieldlines. Surges do not curve back to opposite polarity as sharply as computed lines of force.

In his comprehensive observational survey of active prominence magnetic fields, Harvey (1969) found the polarization signals of surges to be very noisy; he interpreted this as due to the complex nature of the field. I believe the field structure is no more complicated than in any other prominences; indeed the large scale field structure appears much more orderly, since with loop prominences (Roy, 1972), no other prominence is better fitted with potential fields than surges. Table XVII summarizes the results of calculated current-free lines of force compared to observed surge trajectories; Figures 5.21-5.24 show some examples. For the 25 July 1971 surge veil (Figure 5.21), I used a magnetogram taken when the double umbra spot was at E15 S15 (29 July), and for the 23 Oct. 1971 surges (Figure 5.22), the following spot of MW 18594 was at W20 N08. Since the region needs to be at the center of the disk for the measured longitudinal field to coincide with the normal component of the field, this step leads to underestimate the normal component by about 30%; moreover the geometry of the computed fieldlines may be slightly distorted. The homologous surges of 25 July and 23 Oct. 1971 followed exactly the same trajectories indicating that the main field responsible for collimating the ejected plasma remained unchanged. On 20 Oct. 1971 (Figure 5.23), the calculated fieldlines describe a full arch closing back about 100" away south

Figure 5.21. Computed current-free fieldlines matching the surge veil of 25 July 1971 (Figure 5.19). I used a magnetogram of the region obtained by R. Sinha in the line of FeI 6302.5 on 29 July 1971, 1758 UT.

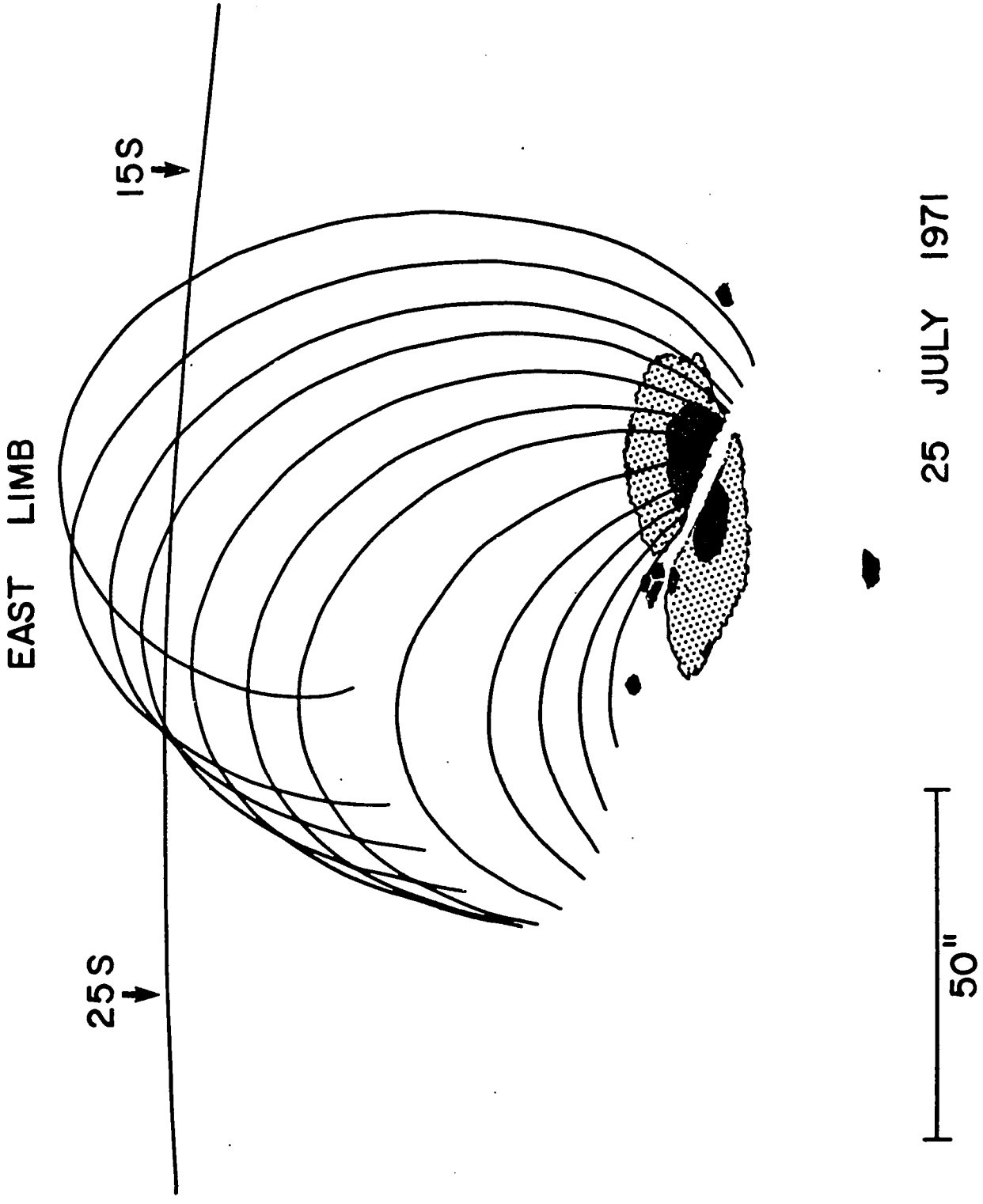
15S
EAST LIMB
25S
25 JULY 1971
50"

Figure 5.22. Computed current-free fieldlines matching the homologous surges of 23 October 1971 (Figure 5.12). The magnetogram used was taken on 23 October at 1918 UT (Figure 5.11).

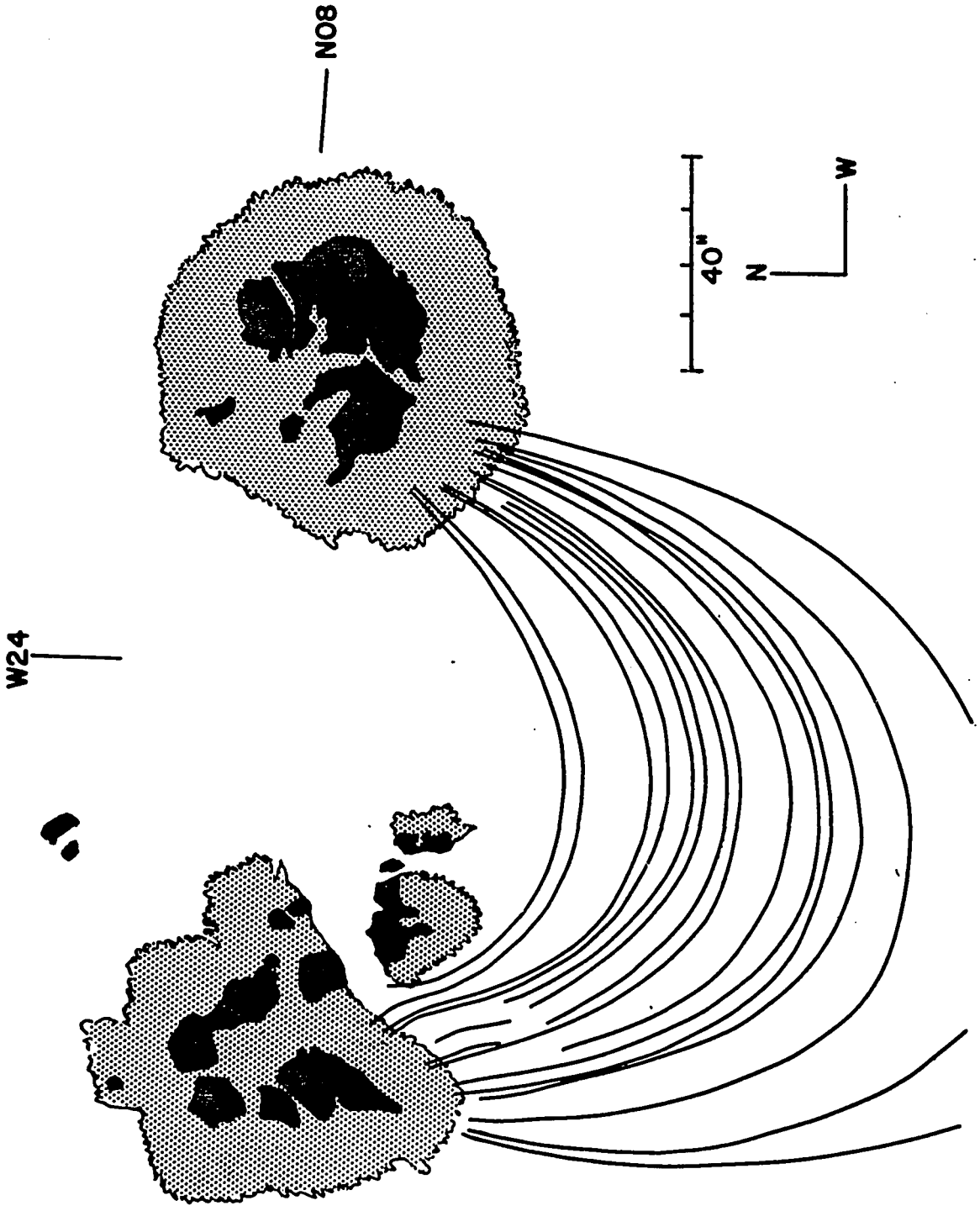
N08
W24
40"
N
W

Figure 5.23. Computed current-free fieldlines matching the surge of 20 October 1971 in MW 18594. The magnetogram used was taken on 20 October, 1547 UT (Figure 5.16). The small surge veil originates ahead of the leading spot which is shown without the fieldlines below a later filtergram of the whole region. The dotted ends of the fieldlines indicate that the calculated lines of force closed back to the surface slightly south of the mark indicating the scale.

20 OCT. 1971

Hα - 7/8 Å

Figure 5.24. Computed current-free lines of force of Figure 5.22 viewed through the plane of the region from a south-east direction. Due to obvious limitations of the current-free method, it produces very low closing fieldlines near the satellite spot; therefore, I reproduce them by expanding the vertical scale generously.

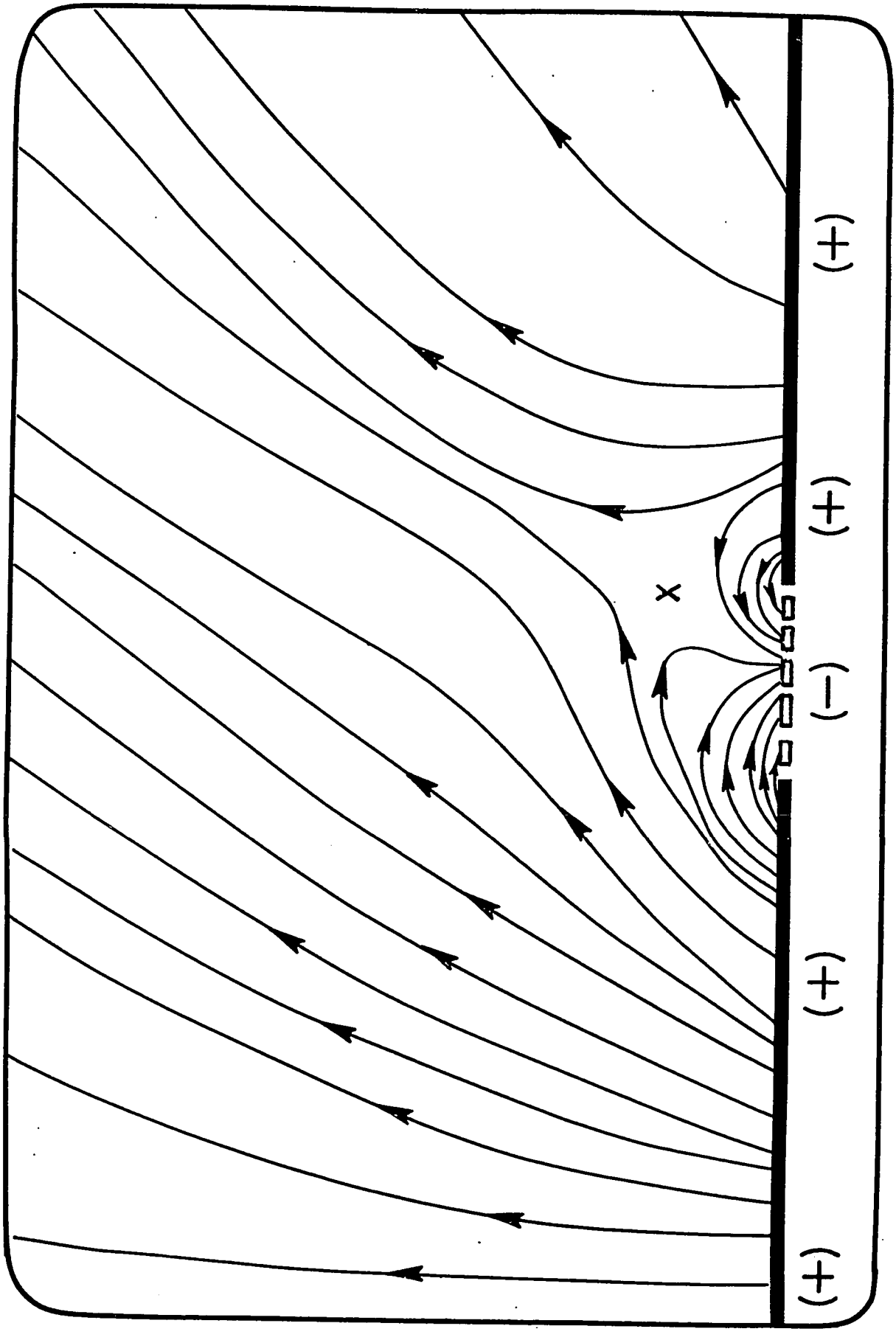
±
±
I
±
±

of the following polarity main spots. The surge threads about 40" long originate slightly ahead of the leading spot of MW 18594.

Curiously, Harvey (1969) measured different field strengths in three homologous surges, i.e. 87 ± 15, 40 ± 15 and 17 ± 6 gauss. An explanation is that Harvey may have measured different threads of a surge which appeared in the same projected position in the sky or that the surge differential dynamics may have affected his time-averaged polarization signal: I found that surge material often moves in completely opposite directions in adjacent channels separated by a few seconds of arc, a scale unresolved by the magnetograph. Stenflo (1968) has shown how 'multi-stream' models where streams are assigned different velocities, areas, intensities and magnetic fields, lead usually to observed average field strength smaller than the true average field strength.

I have been able to reproduce a set of fieldlines with a neutral point overlying the satellite polarity of MW 18594 on 23 Oct. 1971. Obviously, the set of current-free fieldlines of Figure 5.24 has only a qualitative value. But it points out the relationship between intense bomb and surge activity and the probable existence of a neutral point as suggested by Rust (1968). This configuration is of extreme importance for theoretical considerations discussed in section 1.4.2.

5.4 TRIGGERING OF INSTABILITIES IN THE SOLAR ATMOSPHERE

If each thread of the surge connects to a tiny bomb somewhere in the chromosphere, what mechanism triggers their almost simultaneous flaring? Some threads are squeezed out of isolated bombs earlier or later as lonely ejected filaments, but most of the surge ejection occurs in phases. Figure 5.25 illustrates this by showing the successive bursting of surges along the light bridge in region MW 18511 (Figure 5.19); the number of dark surge threads longer than 10 arcsec versus time emphasizes that four main events occured during the 40 min period. Because of the more or less solid sheet appearance of surges at maximum visibility, the actual number of threads may be greater than shown by a factor of 1.5 or 2 for frequency values larger than 10. It explains why low resolution and wide passband filters tend to show surges as huge growing tongues which distend and retract coherently. A surge is actually a phalanx of jets less than one arcsec across originating at a set of bombs in the low chromosphere, triggered outward more or less simultaneously. Nevertheless, the chain reaction of bomb brightenings remains unexplained.

I have also investigated whether Ellerman bomb producing areas tend to travel in a systematic pattern. For MW 18594 five bomb producing locations apparently stayed stationary within one arcsec; some finer structures apparently 'moved' in a definite pattern; because they appeared as well in

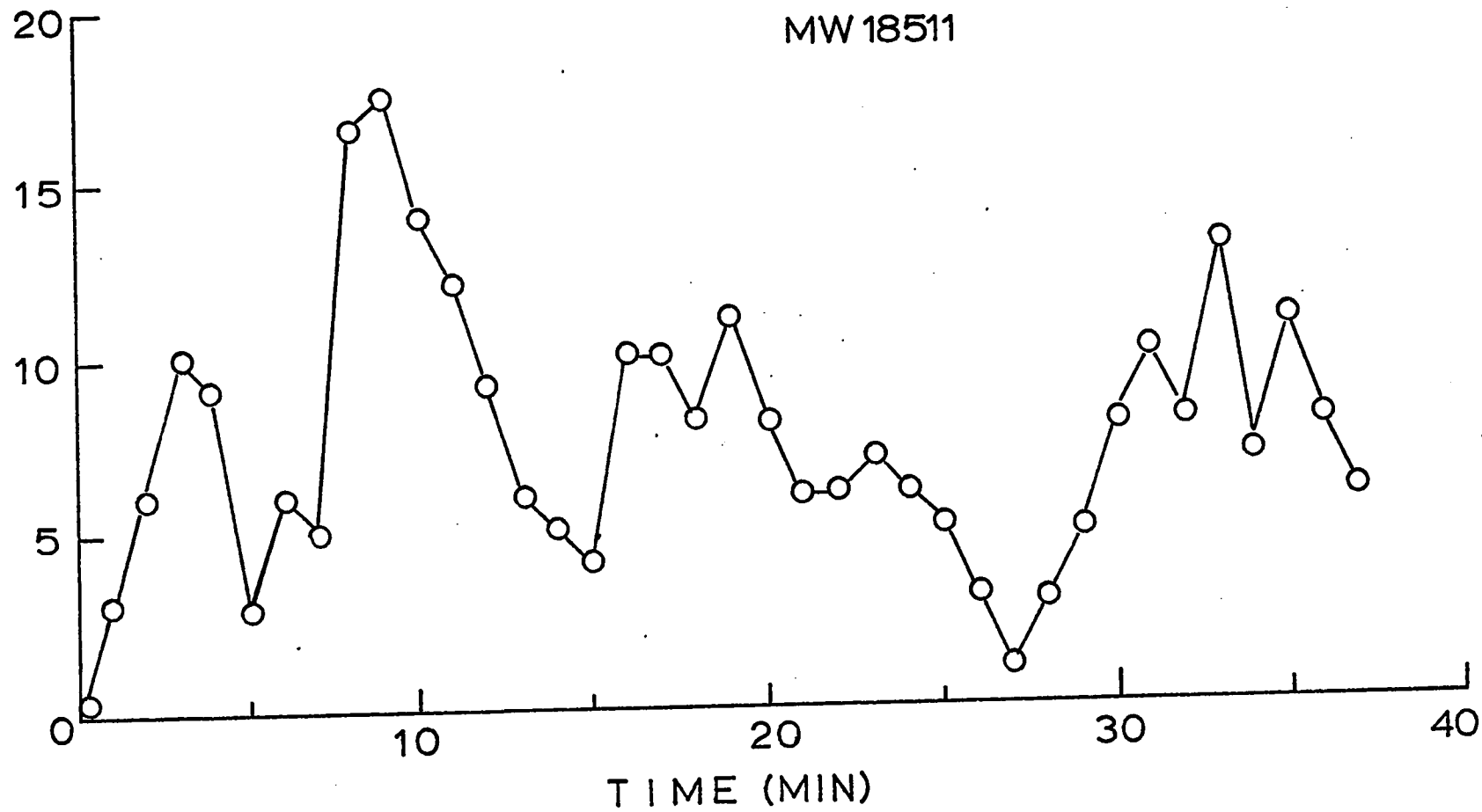

Figure 5.25 Number of dark surge threads longer than 10 arcsec in MW 18511 (Figure 5.19) vs time (25 July 1971).

the red and the blue wings of Hα, they are likely to be some excitation fronts. Figure 5.26 shows the position of Ellerman bombs along the light bridge in MW 18511 as a function of time; bomb producing areas present no systematic displacement along the light bridge over periods longer than four minutes; at times 15 min and 30 min in Figure 5.26, velocities of 0.017 arcsec/s ($\gtrsim$12 km/s) over a period of 100 s can be deduced; most of the small shifts are probably due to the birth or disappearance and shrinking of bombs. One should note that in the sunspot region, the Alfvén velocity is about 11 km/s for a field intensity of 2000 G and a photospheric density of 2.7×10^{-7} g/cm^3.

I have not been able to determine if the field or photospheric changes are progressive or sudden, nor if sudden changes correlate with bomb activity. The phase of the most intense chromospheric activity is apparently shorter (a few hours) than the period (about 20 hours) over which satellite polarities are seen to evolve. It is interesting that the flux change rate recorded with bomb-surge activity amounted to $1 - 3 \times 10^{15}$ Mx/s, a value also obtained by Ribes (1969) and Rust (1972) for flare activity associated with evolving magnetic features. Either this is fictitious because we are simply measuring noise inherent to magnetic recording or, more probably, as the quality of the observations indicates, the flux change represents real magnetic energy dissipation

Figure 5.26. Position of Ellerman bombs or of clusters of bombs along the light bridge in MW 18511 as a function of time; t_o is 150924 UT, 25 July 1971. Slopes with their corresponding displacement velocity in arcsec/sec are given in the lower left corver; 10 km/sec (roughly the Alfvén velocity in the photosphere under a magnetic field of 2000 G) corresponds to 0.014 arcsec/sec under no projection effect.

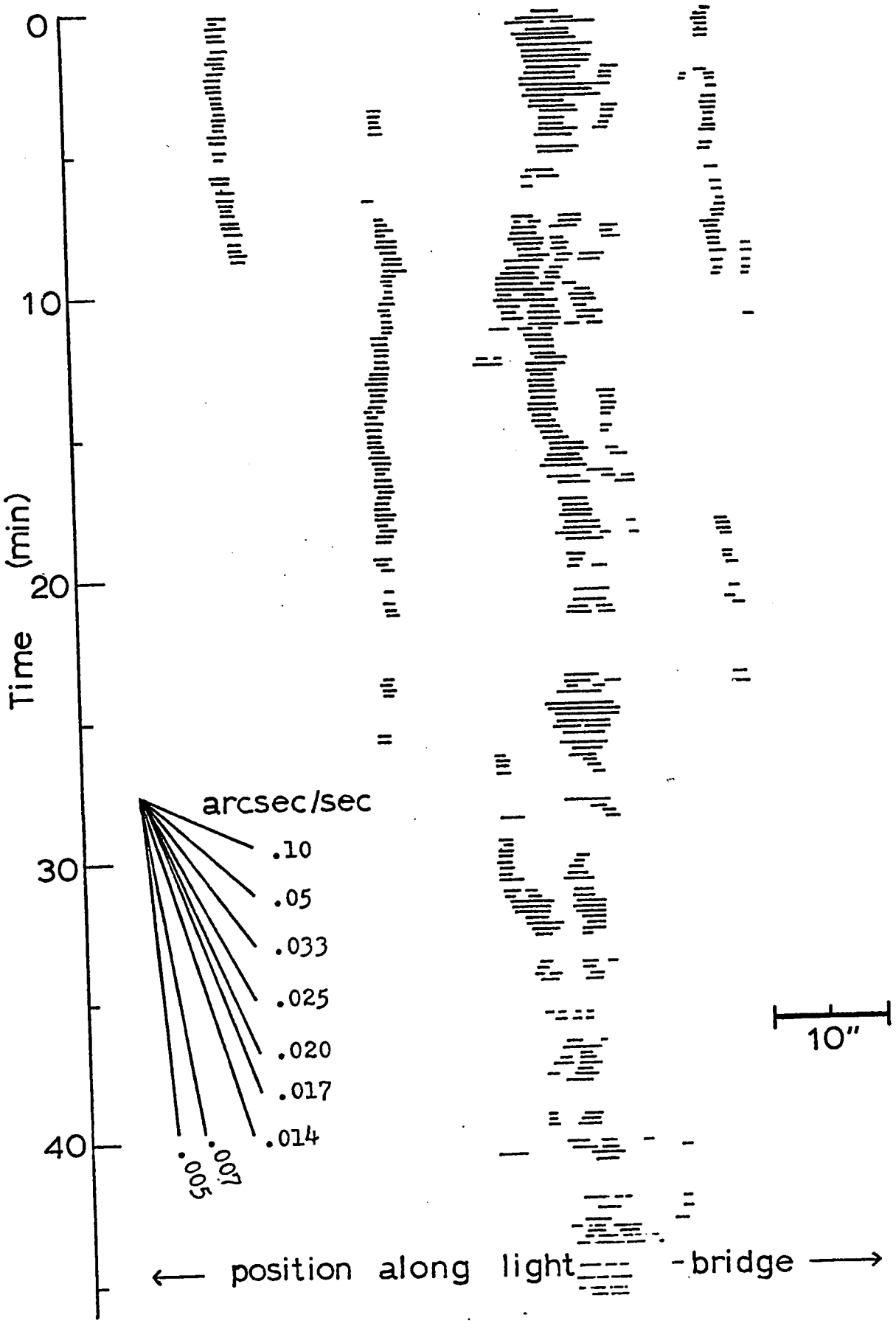
0
10
20
30
40
Time (min)
arcsec/sec
.10
.05
.033
.025
.020
.017
.014
.007
.005
10"
← position along light-bridge →

associated with evolving satellite spots. Since 1 volt= 10^8 CGSM, according to Maxwell's equation the emf induced in region MW 18594 by the flux change rate $\Delta F/\Delta t$ = -3×10^{15} Mx/s is

$$\oint E\, ds = -\, 10^{-8}\, \Delta F/\Delta t \qquad 5.4.$$

If $\Delta F/\Delta t$ is expressed in CGSM units (Mx/s), then

$$\oint E\, ds = 3 \times 10^7 \text{ volts.}$$

Since Ribes, Rust and I find a similar value for $\Delta F/\Delta t$ in evolving satellite polarities, it may represent a threshold in the electric field for flaring break-down to happen in the solar atmosphere. On the other hand, the given emf is an order of magnitude or more smaller than the values given by Zvereva and Severny (1970) for proton emitting regions. Those authors have concluded that the 10^7 volts also calculated for small flares are below the critical value for generating hard particles. It explains why surge events are not associated with proton emission detectable at one A.U.

5.5 ENERGY RELEASED THROUGH MAGNETIC FLUX CHANGE

Surges and bombs take place in regions of evolving satellite polarities in some cases. In MW 18594, with detailed magnetic coverage, the (-) flux diminished by 2.5×10^{19} Mx over a period of 140 min, i.e. a rate of 3×10^{15} Mx/s. If 2.5×10^{19} Mx of negative flux disappears, one should expect a parallel weakening of positive flux. However, it remains much easier to detect such a change in a small satellite spot than in the large

parent spot with extensive regions of strong field totalling a net flux of about 10^{22} Mx.

The available magnetic energy density given by a change in the magnetic field is

$$\Delta E = \frac{B_{ini}^2}{8\pi} - \frac{B_{fin}^2}{8\pi} \qquad 5.5.$$

One needs to assume something about the height in the atmosphere above the photospheric magnetic polarity to get the total output. This is hard to determine; certainly a good portion of the chromospheric levels is involved. Let us assume that the annihilated flux extended upward to a height of 2000 km. In MW 18594, the change involved an average field change of 40 G to zero over an initial area of 6000 km square

$$V_{ini} \times \Delta E \approx 5 \times 10^{27} \text{ ergs} \qquad 5.6.$$

(The true field change was probably larger over a smaller area). Therefore, at least 10^{27} ergs were available for each of three surge events in MW 18594. The nature of Ellerman bombs points out that this release is usually impulsive (over about 10 min). From the data provided by Severny (1964), the bomb thermal energy content can be calculated assuming a particle density of $n_e = 10^{13}$ cm^{-3} and $T = 10^4$ K.

$$N\,kT \times \text{Volume} = 1.4 \times 10^{27} \text{ ergs} \qquad 5.7$$

for one Ellerman bomb of the size seen in MW 18594; there were three of these large bombs and a few smaller ones. The energy content of a bomb which develops a large

surge is of the same order of magnitude as the energy available from the magnetic annihilation. The amount of flux annihilated is measured from the longitudinal component of the field only; therefore, the true total amount of energy is likely to be larger. For smaller and more common events, like those studied in section 5.1, the energy content is about 10^{26} ergs due to their smaller volume (Bruzek, 1972). We find the total energy required to produce a surge from an estimate of the kinetic energy of the outward moving material. The velocity of surges is about 100 km/s. The 23 Oct. 1971 surges in MW 18594 consisted of a 10^4 km wide sheet of surge filaments of the order of 10^3 km in diameter and extending up to 5×10^4 km from their associated bombs. The density in surges has been estimated to be between 10^{11} and 10^{12} cm^{-3} (Tandberg-Hanssen, 1967; see Table I) assuming a uniform distribution of the material. As we saw, large density fluctuations occur from inter-thread to thread regions. I assume the lowest value for the density in a uniform sheet. The kinetic energy of the surge is then

$$\tfrac{1}{2} Mv^2 \approx 5 \times 10^{27} \text{ ergs} \qquad 5.8.$$

These energies (eqs. 5.7 and 5.8) are of the same order magnitude and comparable to the vanishing magnetic energy (eq. 5.6).

CHAPTER VI

RESULTS II: VELOCITY CURVES OF SOLAR SURGES

6.1 SOME PROBLEMS

I measured the velocity of five different surges in regions MW 18511 (25 July 1971), MW 18594 (23 Oct. 1971) and SPO 2768 (31 May 1971). The measurements were done with superposed grids by following the position of the tops of surge threads with time. The center of the associated Ellerman bomb was taken as the origin. The position of another reference point, generally a small pore, was followed in order to remove spurious motions caused by seeing and image jumps. Plots of position of the top of surges as a function of time appear in Figure 6.1. Points were obtained for as many wavelength shifts as possible; although the surge can be visible over a spectral range of 2 Å in a same wing of Hα, the contrasts of surge features vary greatly with wavelength.

Problems in interpreting moving material in filtergrams were discussed in section 3.1.2. Changes in visibility tend to be most crucial in the first few thousand km from the bomb where the containing magnetic field often presents a sharp bend causing the moving material to appear or disappear suddenly. It is almost impossible to track down unambiguously motion of material

Figure 6.1. Position as a function of time of surge tops. (a) MW 18511 (25 July 1971), ejection A; t_o (-2 Å) 151336 UT, t_o (-7/8 Å) 151512 UT, t_o (-5/8 Å) 151400 UT and t_o (-¼ Å), 151436 UT. (b) MW 18511 (25 July 1971), ejections B and B'; t_o (-7/8 Å) 152200 UT, t_o (-5/8 Å) 152030 UT. (c) MW 18594 (23 October 1971); the surge filaments are inclined by 20-25° with respect to the solar surface; t_o (-2 Å) 190900 UT, t_o (-1 3/8 Å) 1908 UT, t_o (-7/8 Å) 190600 UT and t_o (-5/8 Å) 190620 UT. (d) Bright surge on the limb at position angle 80° in SPO 2768 (31 May 1971). Hand-fitted curves go through the points.

The error bars represent the uncertainty on the position of the tip of the surge thread followed: (i) even under good seeing the tip is not perfectly sharp but slightly diffuse; (ii) under bad seeing, the uncertainty is obviously larger; (iii) or the dark tip of a surge thread may be preceded by a diffuse or well defined independent knot whose visibility varies with time; for this case, I consider the center of the knot as the 'tip', and the error bar deli ne ates the whole knot. These comments apply to Figure 6.3 also.

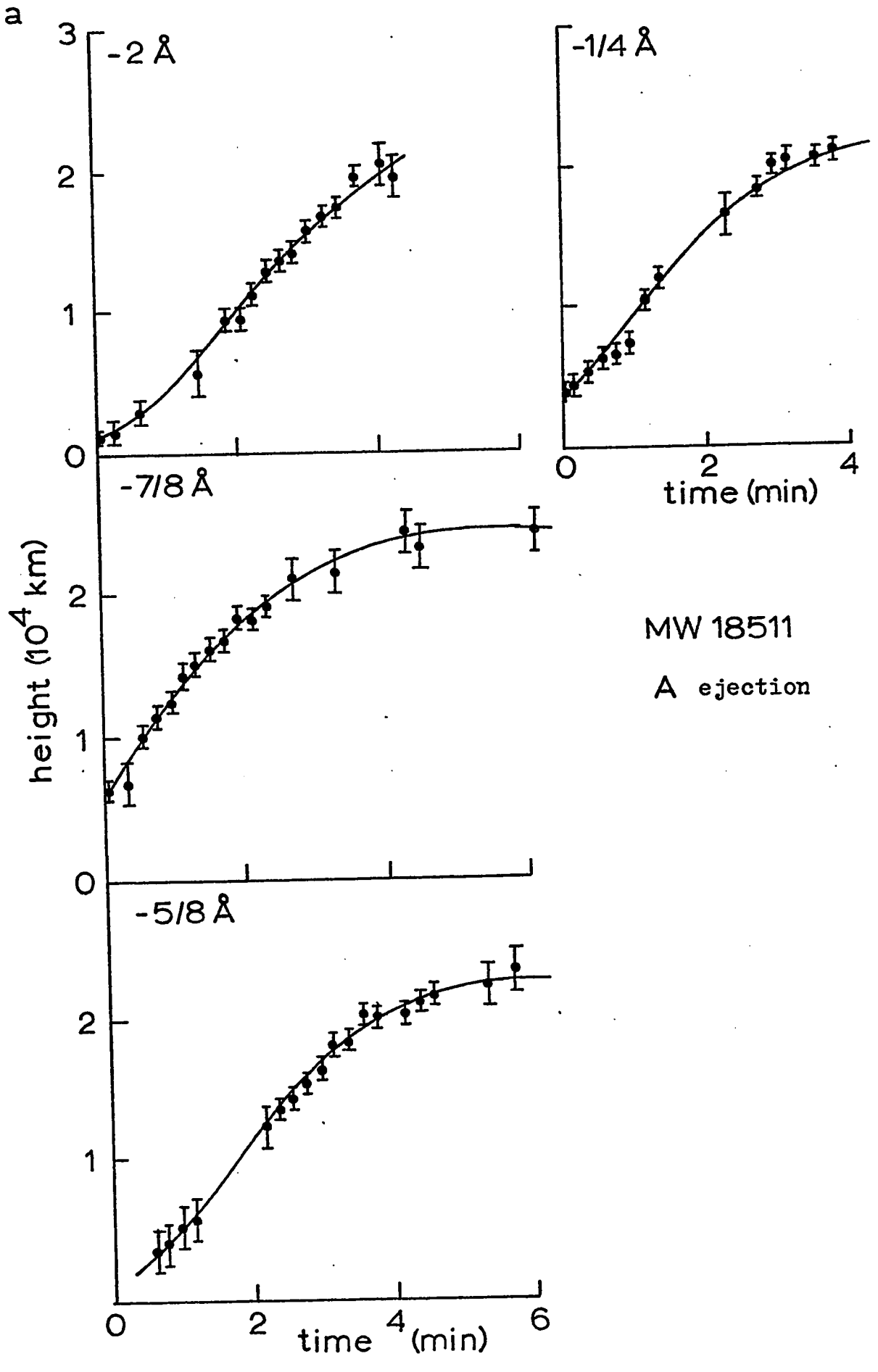
a
-2 Å
-1/4 Å
-7/8 Å
-5/8 Å
height (10^4 km)
time (min)
MW 18511
A ejection

a

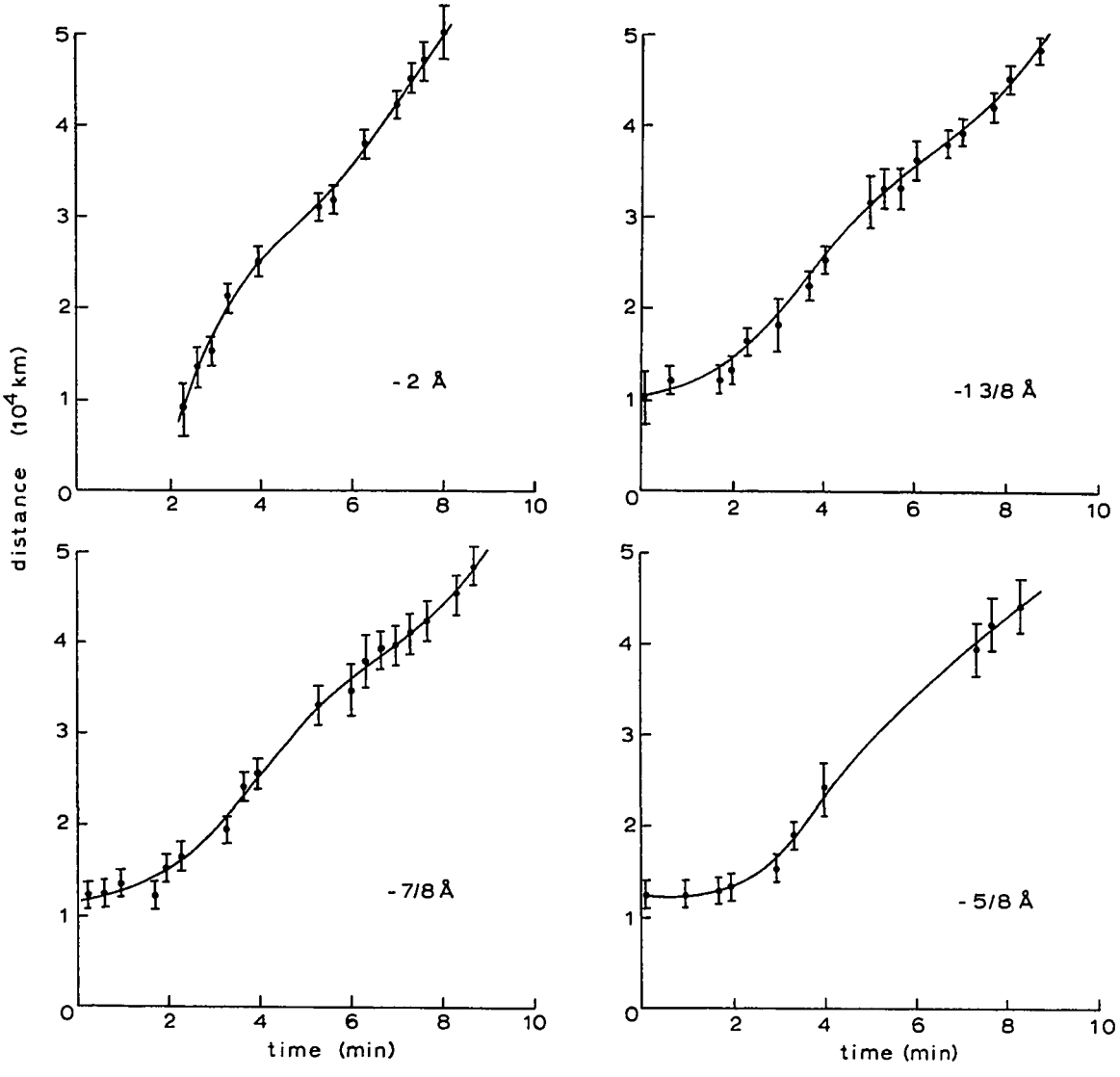
MW 18594
distance (10^4 km)
-2 Å
-1 3/8 Å
-7/8 Å
-5/8 Å
time (min)
time (min)

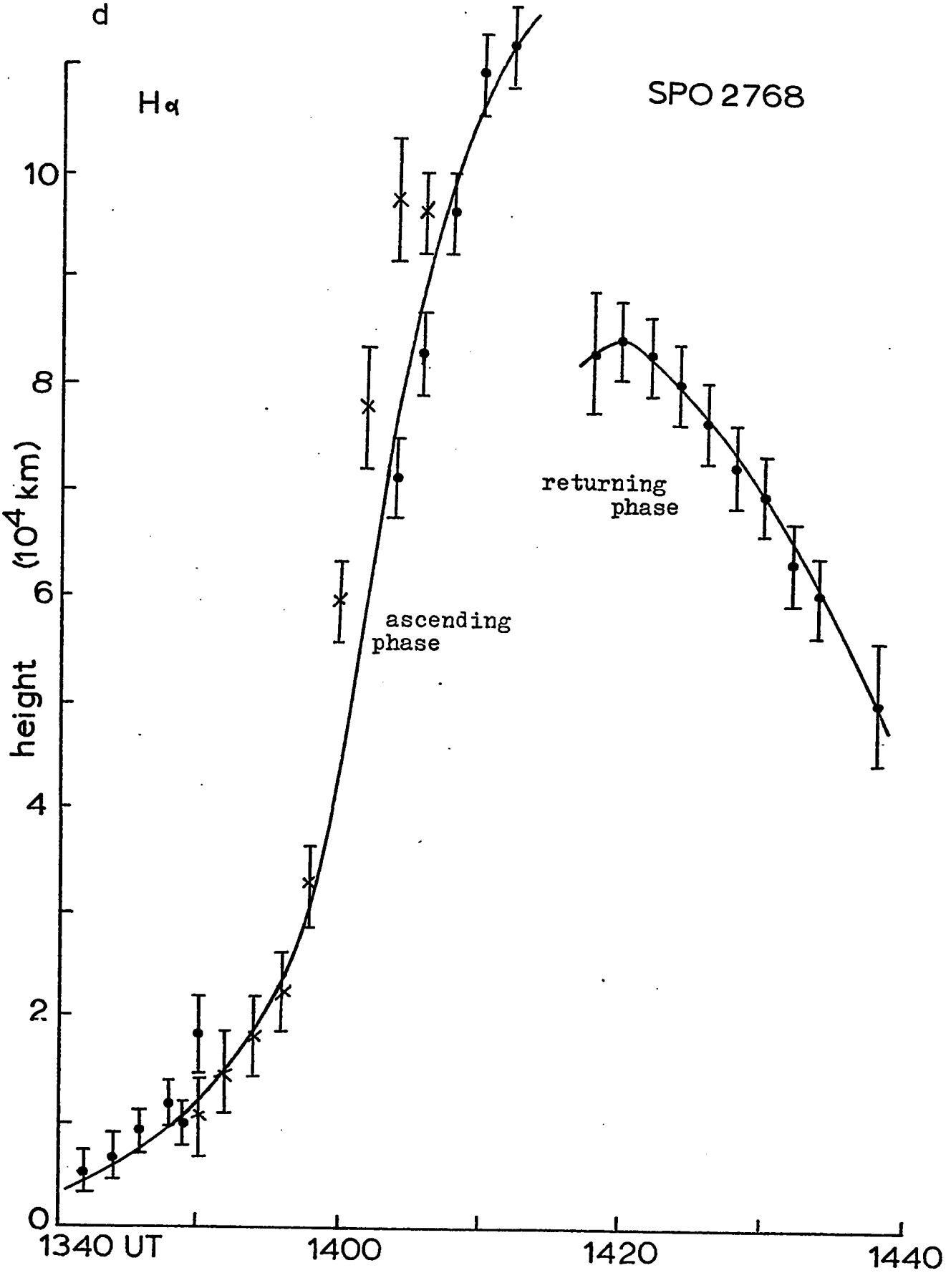
d
Hα
SPO 2768
height (10^4 km)
0
2
4
6
8
10
1340 UT
1400
1420
1440
ascending phase
returning phase

within 5 000 km of the bomb.

An important aspect is obtaining the full velocity vector. This is possible when one knows the exact geometry of the surge; the full vector is deduced from one velocity component and the trigonometric parameters; in section 5.3, I matched surge trajectories with current-free lines of force computed in three dimensions; such calculations provided geometrical models for the surge configurations in MW 18511 and MW 18594. For the veil of surges of MW 18511 and the surge of SPO 2768, I assumed the surge filaments to be normal to the surface; they were actually inclined by about 0-15° from the normal. The average inclination angle of 20° with respect to the surface of the surges in MW 18594 was taken into account. Extrapolated line-of-sight velocities from the measured normal line-of-sight velocities were entirely consistent with the observed Doppler shifts of the same features.

Since the acting force on the surge is not constant, I fitted a smooth curve by hand through the points of position of tops vs time. Thereafter, I deduced the velocity vs height (or vs distance from the bomb center) from the slope of the fitted curves; these curves are shown in Figure 6.2. The same procedure was repeated for the descending phase or returning phase of surges (Figures 6.3 and 6.4). Rough values of the net acceleration, g_{eff} in km/s^2 are indicated along the various phases of the evolving surge: (i) the fast ascending phase, (ii) the

Figure 6.2. Velocity vs height (or distance from the associated bomb for MW 18594) curves for the ascending phase of surges are determined from the slopes of the hand-fitted curves of Figure 6.1. The dashed curves are deceleration curves expected for solar gravity braking after the surge has reached its maximum velocity. Deceleration is stronger than solar gravity (-.27 km/s^2) alone in the two surges of MW 18511 (a and b) and in one surge of MW 18594 (c). Only for the limb surge of SPO 2768 (d) is the braking portion fitted by a gravity force only. The curves fitted through the points corresponds to an acting net specific force as indicated along the curves V vs height. The acceleration is in km/s^2; a (+) sign indicates that the acceleration is directed outward from the sun.

The 'dip' in the curve of MW 18594 (c) at about 40 000 km is probably real because it is also present during the returning phase of the surge (Figure 6.4 c); for this event, the dashed curve represent the deceleration for v_o = 150 km/s and $g_\odot \sin \theta$, where $\theta = 20^o$, angle of the surge with the surface.

Projection effects due to the inclination of the surge to the normal to the line of sight have been taken into account in deducting the velocities from Figure 6.1.

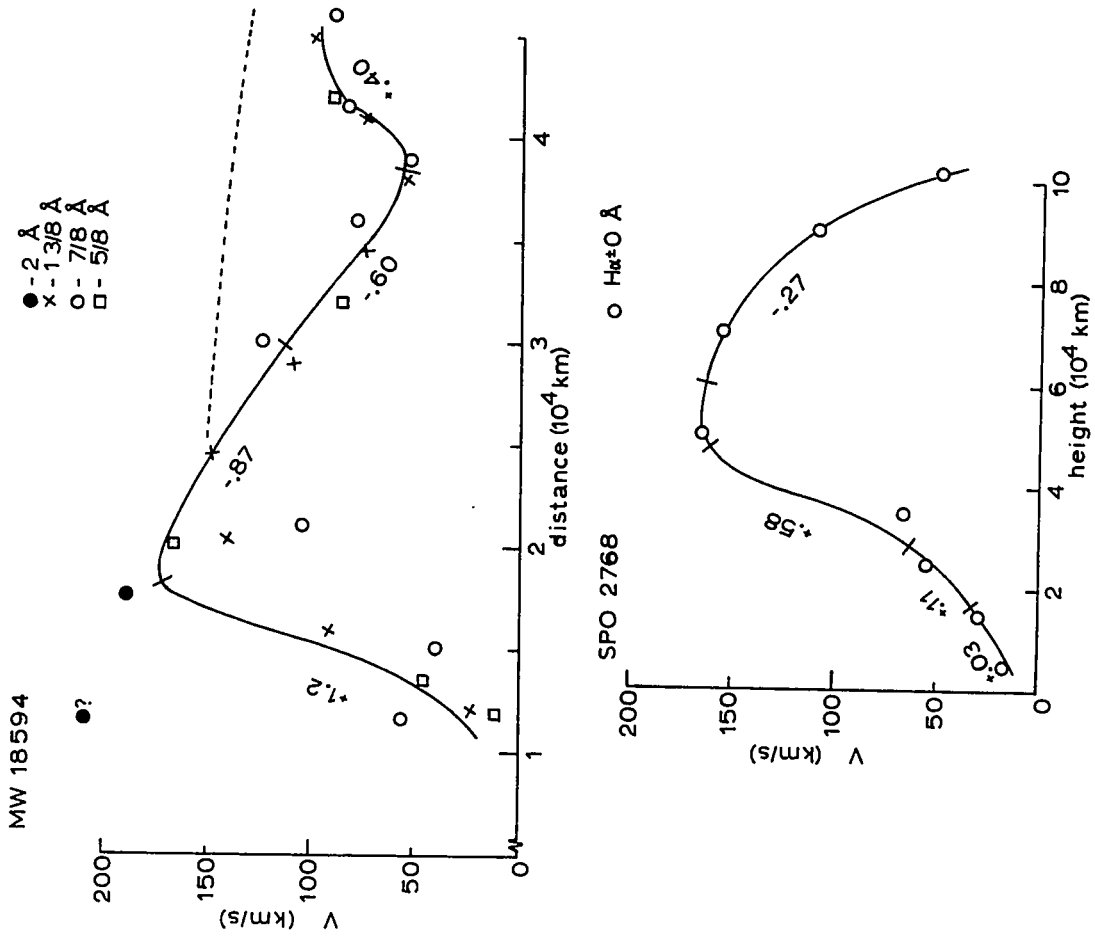
MW 18594
●-2 Å
×-1 3/8 Å
○-7/8 Å
□-5/8 Å
●?
V (km/s)
distance (10^4 km)
SPO 2768
○ Hα±0 Å
height (10^4 km)

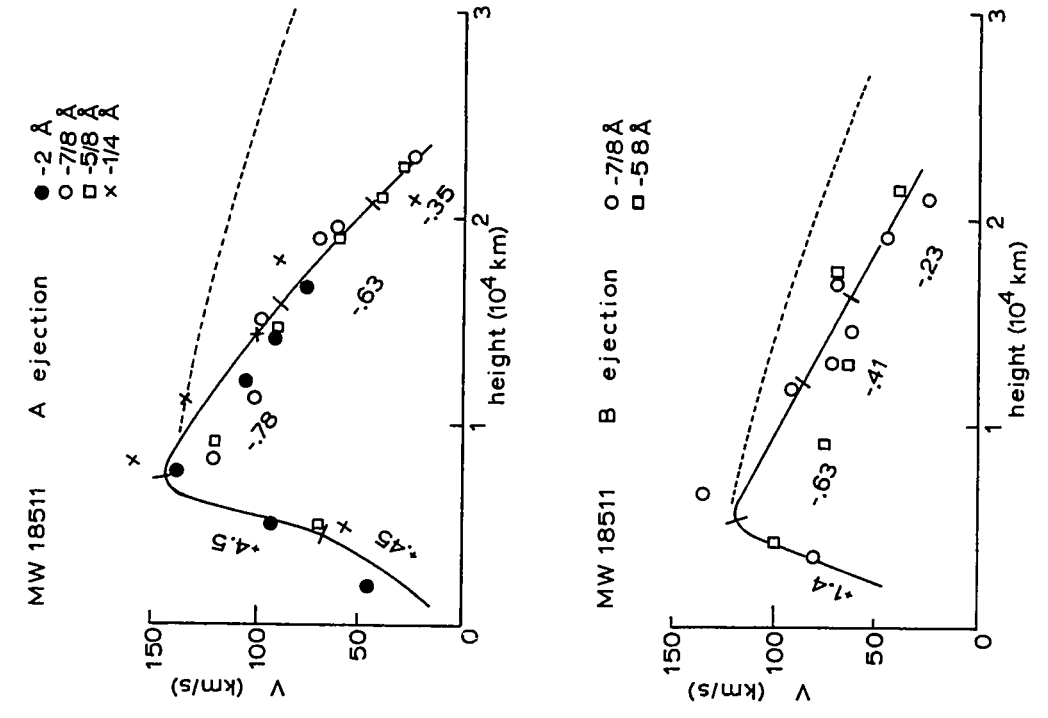
MW 18511 A ejection
●-2 Å
○-7/8 Å
□-5/8 Å
×-1/4 Å
MW 18511 B ejection
○-7/8 Å
□-5 8 Å
V (km/s)
height (10^4 km)

Figure 6.3. Returning phases of surges; curves of position of surge tops vs time. (a) MW 18511, ejection A: t_o (+5/8 Å) 152220 UT, t_o (+7/8 Å) 152120 UT. (b) MW 18594: t_o (+5/8 Å) 201200 UT, t_o (+7/8 Å) 201200 UT and t_o (+1 3/8 Å) 201130 UT; in this last case, five different threads were measured to complete the curves.

a

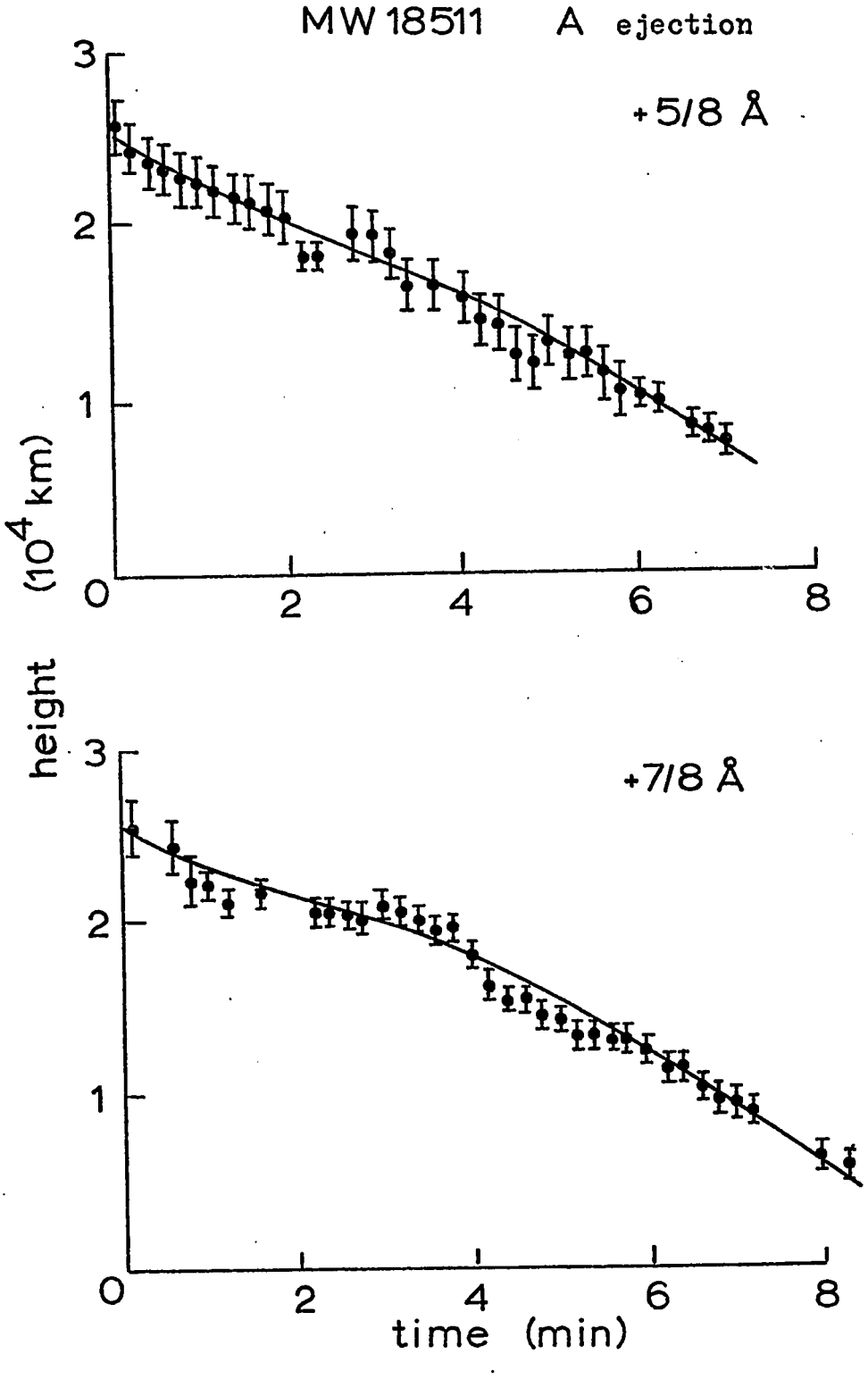

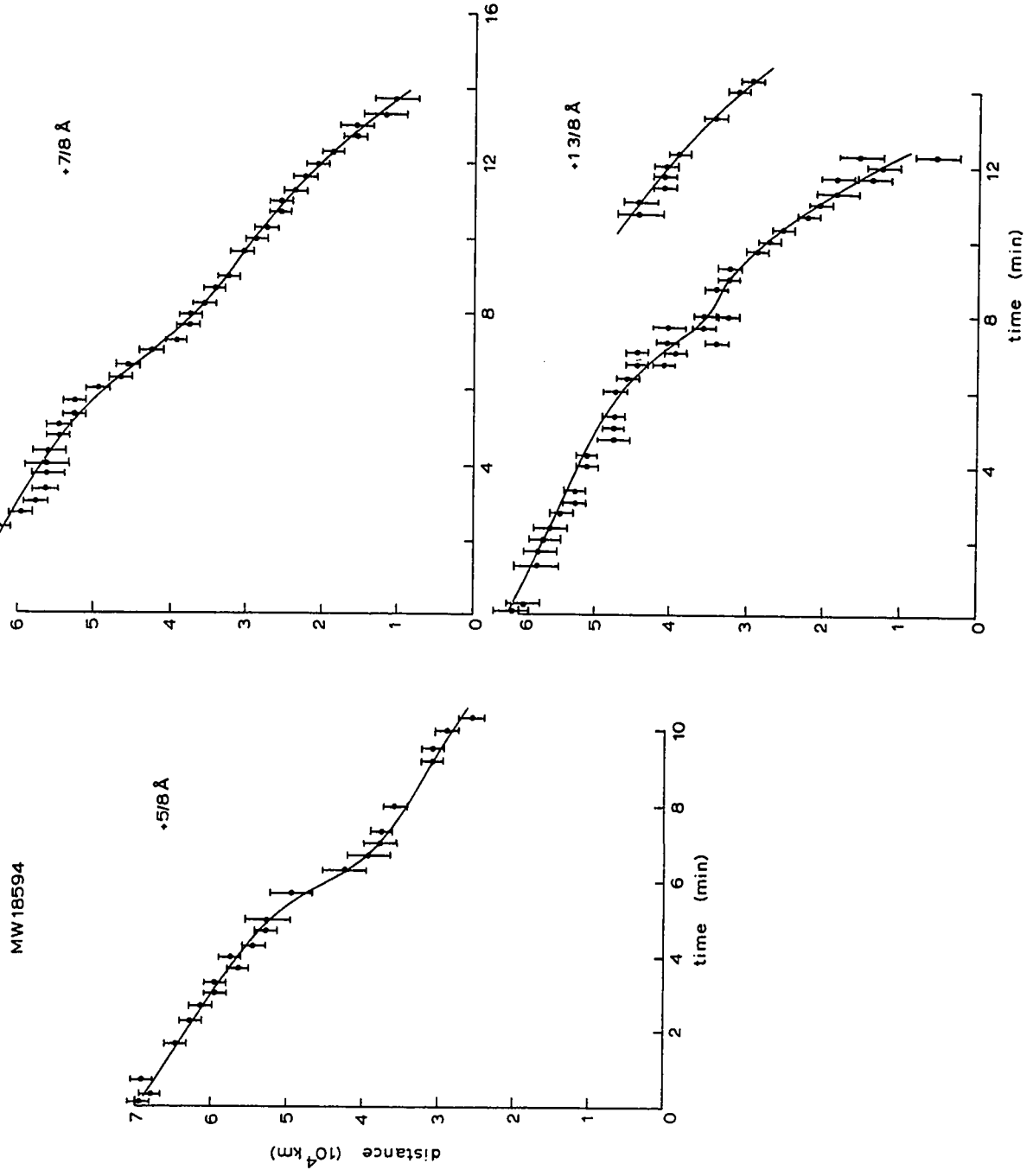
MW18594
+5/8 Å
+7/8 Å
+13/8 Å
distance (10⁴ km)
time (min)

Figure 6.4. Velocity as a function of height curves determined from curves in Figure 6.3, for the surge returning phases. Smaller accelerations than free-fall (dashed curves) are observed in two out of three cases. MW 18594 (b) shows a falling velocity larger than free-fall! This may be due to a wrong interpretation of the geometry added to visibility problems. If real a reasonable interpretation is not easy; the ascending phase of the same surge (Figure 6.2 c) was affected by a larger than gravity braking.

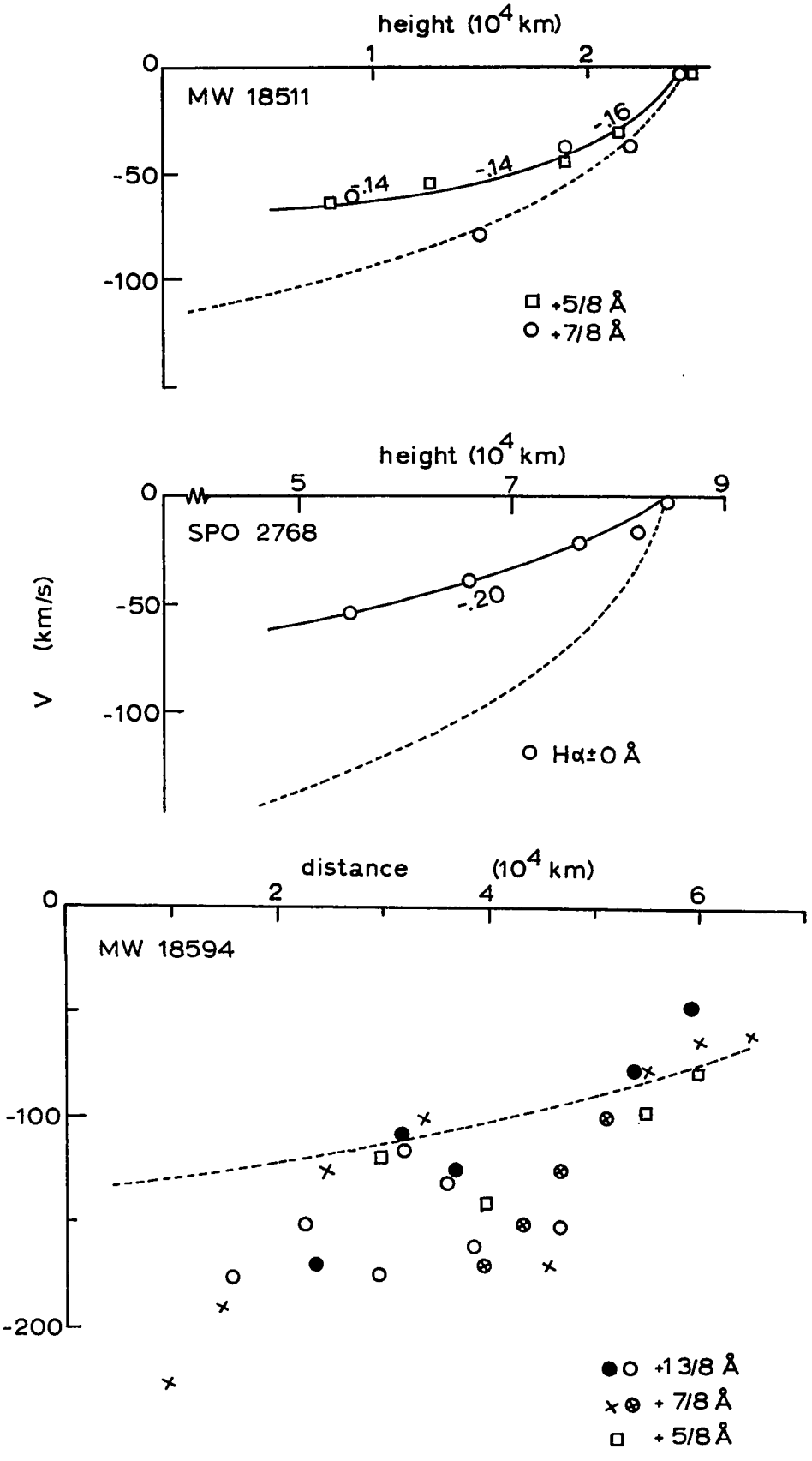
height (10^4 km)
0
1
2
MW 18511
-50
-100
-.16
-.14
-.14
□ +5/8 Å
○ +7/8 Å
height (10^4 km)
0
5
7
9
SPO 2768
V (km/s)
-50
-100
-.20
○ Hα±0 Å
distance (10^4 km)
0
2
4
6
MW 18594
-100
-200
●○ +13/8 Å
×⊗ + 7/8 Å
□ + 5/8 Å

decelerated ascending phase and (iii) the return phase.

6.2 THE ASCENDING PHASE

The fast ascending phase is the characteristic phase where solar surges rush out from the bomb region. The solid curves fitted through the points of velocity vs height in Figures 6.2 and 6.4 correspond to values of acceleration shown along the different portions of the curves. The outward acceleration takes place over a range of 0-50 000 km depending on individual surges, with a mean acceleration (g_{eff}) of 1.2 km/s^2, i.e. more than 4 times the solar gravity and opposite in direction; see Table XVIII. The general behavior of surge velocity indicates

Table XVIII

The ascending phase of surges

Region	g_{eff} (km/s^2)	Surge maximum apparent length (km)	Maximum velocity (km/s)	Height at max. velocity (km)
MW 18511	+2.10	50 000	150	7 000
MW 18594	+1.18	80 000	175	20 000
SPO 2768	+0.24	100 000	170	50 000

a slow initial acceleration rapidly increasing at a few thousand km above the bomb. The reality of an initial slow acceleration before the rush phase remains uncertain due to the difficulty in obtaining reliable velocities. However, the surge gains momentum progressively outside the associated Ellerman bomb itself. There is some evidence that the acceleration changes through time; I will return to this at the end of the chapter.

The second phase, the ascending decelerated phase, takes

place after the surge has reached a velocity of 100-175 km/s at a height of 7 000 - 50 000 km (Table XVIII). A characteristic of this phase is the stronger deceleration than if gravity alone were acting. The possibility of the material becoming optically thin near the top because of expansion could mimic a fast slowing down; however, the width of surge threads remains remarkably constant with height and any expansion would need to occur along the thread. The sharp drop in velocity at large heights could also be due to the disappearance of the material becoming excited by the hot ambient corona. This is also ruled out from the observation in the Hα red wing of the surge material returning to the surface along the same path slightly later, and showing still very strong contrast; it appears that very little material 'boils off' of the surge tip. The strong deceleration is probably real.

6.3 THE DESCENDING PHASE

Obviously from Figures 6.3 and 6.4, the acceleration toward the solar surface of returning material remains less than solar gravity, i.e. one does not have free-fall! A similar behavior was observed by Newton (1942) during the falling back phase of surges. Furthermore, Jefferies and Orrall(1965) and Roy (1971) observed that the velocity of falling material in post-flare loop prominences is also less than free-fall. However, in the case of MW 18594, falling velocities are larger than free-fall although braking was observed during the ascending phase (Figure 6.2).

Because of the large scatter in the points of Figure 6.4, this behavior remains difficult to analyse. One should keep in mind the possibility that the braking may not always be acting.

6.4 INTERPRETATION

Apparently, we are in the presence of a common behavior of active prominence material moving in a strong magnetic field. In addition to gravity, a force is acting which opposes the motion of the surge material (except during the initial uprushing phase). Moreover, the acting acceleration $|a| = |g_{eff}| - |g_{\odot}|$ is proportional to the velocity of the surge as depicted in Figure 6.5.

A surge moving into the corona, is not travelling in a vacuum but is ploughing its way through a medium having a finite energy density due to the thermal pressure of the gas. Could the gas pressure in the corona provide a resistance able to slow down the moving material of surges or loop prominences? One can look into this by comparing first the energy density in the flow of surge falling material, $\frac{1}{2}\, m_H v^2$ N, to the thermal energy density in the low corona, N kT. These are respectively about 100 ergs/cm^3 and 1 erg/cm^3 for surge density and velocity of 10^{12} cm^{-3} and 100 km/s, and coronal density and temperature of of 10^{10} cm^{-3} and 10^6 K. Second, because of the large scale height of the solar corona (~50 000 km above active region) the thermal energy density of the gas diminishes by only a factor of 3 or 4 over the height of a typical surge.

Figure 6.5. The net braking force is proportional to the velocity and directed against the motion. This diagram was constructed by using two ejections in MW 18511 (two rising and one falling phases), two ejections in MW 18594 (one rising and one falling phases), one ejection in SPO 2768 (one falling phase). The braking is acting as soon as the surge has reached its velocity maximum.

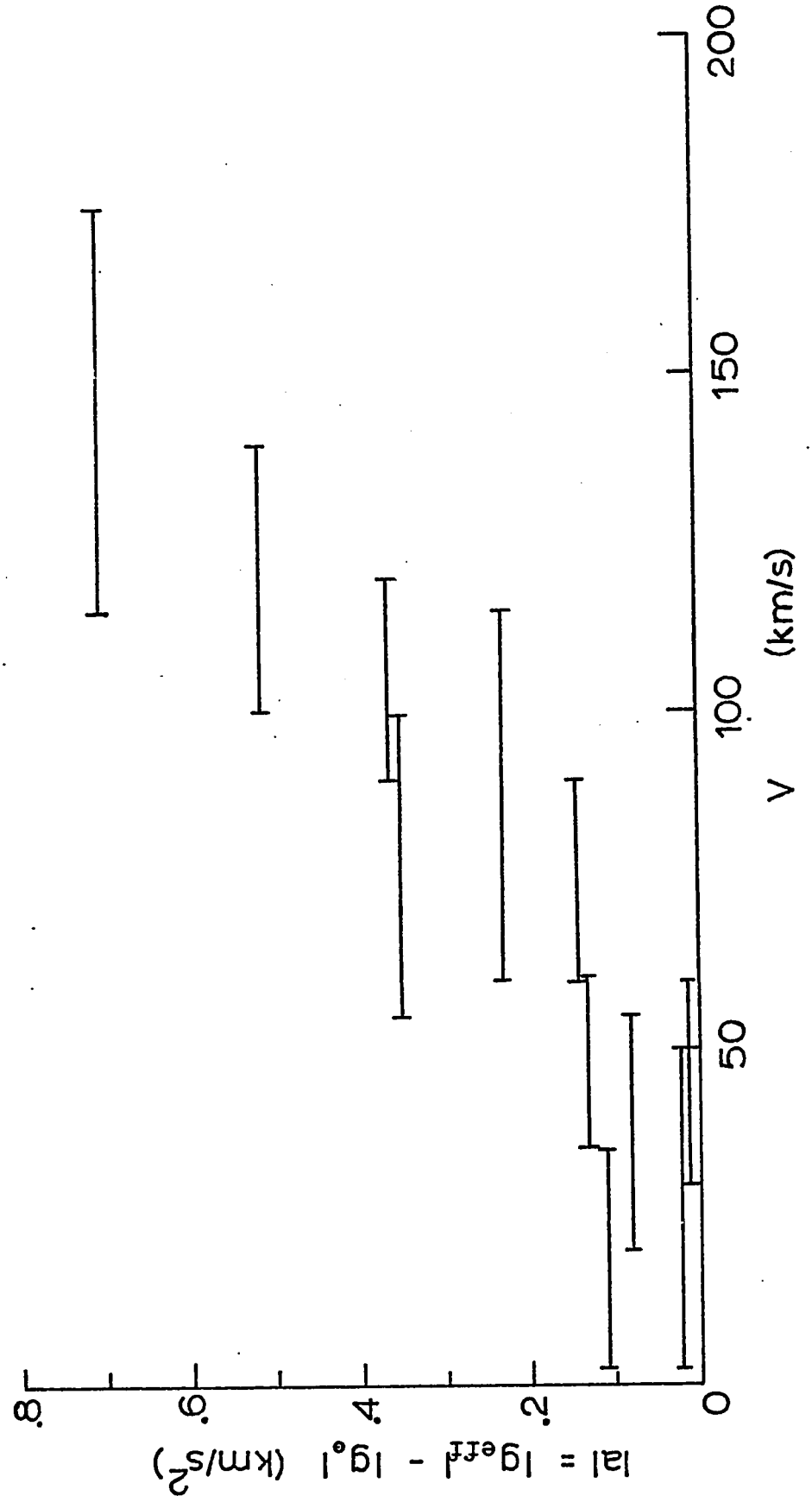
0
2
4
6
8
|a| = |g_eff| - |g_o| (km/s²)
0
50
100
150
200
V (km/s)

Therefore, at the top of a surge 50 000 km high, the thermal energy density due to the gas pressure will amount to about $\frac{1}{4}$ erg/cm^3; if the surge keeps about the same density with height, its velocity will need to be less than 5 km/s for the coronal energy density to be greater than the kinetic energy density of the flow. Because the kinetic energy density increases as v^2, only the material at the very end of the surge trajectory will be compressed by the coronal gas pressure. As seen in Figures 6.2 and 6.4, the slowing down is observed acting at velocities much larger than 10 km/s. Thence, I conclude that the thermal energy content of the coronal gas should not affect the surge motion by an observational amount in general.

Viscosity-type forces in the form of momentum exchange between surge threads moving in opposite directions along the same magnetic tube could perhaps imitate an opposing force; but it is hard to provide a continuous effect; the force is also acting on 'virgin' ejections where such momentum exchange should hardly be present because of no antecedent ejection. The force of a magnetic pressure is directed upwards (direction of weakening field) and cannot explain the braking during the ascending phase of the surge. The braking could be due to the effect of producing shocks in front of the flow in the existing tenuous coronal matter ahead of the flow. However, shock production may not be a heavy burden when the momentum of the flow greatly exceeds the pressure difference (Uchida, 1969). The braking

force would not then show the positive correlation with velocity as observed in Figure 6.5; the solar acceleration of $-.27$ km/s^2 was removed to obtain the absolute values of the braking force. The 'error' bars refer to the range in velocity of the corresponding acceleration for the fitted curves of Figure 6.2.

The best candidate is the Lorentz force

$$\underset{\sim}{f} = \frac{1}{c} (\underset{\sim}{J} \times \underset{\sim}{B}) \qquad 6.1.$$

$\underset{\sim}{J}$ is the electric current density and $\underset{\sim}{B}$ the magnetic flux density. Since the electrical conductivity in the surge plasma is large but not infinite, motion perpendicular to a magnetic field is resisted by induction drag.

The magnetic energy density $B^2/8\pi$ remains much larger than the surge kinetic energy density $\frac{1}{2}\rho v^2$ at all heights; typical values at a height of 5 000 km are $B^2/8\pi \approx 4 \times 10^4$ ergs/cm^3 for B=1 000 G, and $\frac{1}{2}\rho v^2 \approx 10$ ergs/cm^3 for $n \approx 10^{12}$ cm^{-3} and v=50 km/s; at about 50 000 - 100 000 km where the surge reaches its maximum velocity, these values 400 ergs/cm^3 for B=100 G and 50 ergs/cm^3 for v=100 km/s. Movies of solar surges, where the material falls back to its source along an extensive arch illustrate the control of the magnetic field over the material. It is likely that the field not only controls the direction of the surge but also affects significantly its dynamics whenever it deviates only slightly from a potential or force-free configuration.

Large scale surge trajectories are matched excellently

by current-free lines of force arising from the photospheric sources (section 5.3; Figures 5.21, 5.22 and 5.23). The magnetic energy is potential since there may not necessarily be a direct interaction between the prominence material and the field on a bulk scale; therefore no work can be done on the material. To accomplish the work of slowing down surges, the field must have some fine scale structure. Perturbations in the 'potential' field may arise from local electric currents as following:

1. Fieldlines are not infinitely rigid; the weight (and/or thermal pressure) of the traveling surge material creates a small dip along the supporting current-free fieldlines. This distortion corresponds to a local electric current source

$$\underset{\sim}{j} = \frac{c}{4\pi} \nabla \times \underset{\sim}{b} \qquad 6.2.$$

A slight twist of the magnetic lines of force anchored in the photosphere can assume a helical force-free configuration in the absence of material. However, injection of the rapidly moving surge may introduce local current sources.

2. Micro-instabilities between an internal surge magnetic field and the supporting coronal field may be sources of electric currents.

The most immediate model for a force opposing material motion is to postulate the existence of a magnetic field normal to the direction of the surge motion generating a

Lorentz force. The velocity vector $\underset{\sim}{v}$ is not exactly parallel to $\underset{\sim}{B}$ due to dynamic or gravity deformation. One divides $\underset{\sim}{B}$ into a component $\underset{\sim}{B}_o$ parallel to $\underset{\sim}{v}$ and a component $\underset{\sim}{b}$ perpendicular (Figure 6.6). Because of good agreement between observed structures and potential calculations, the $\underset{\sim}{b}$ component must amount only to a fraction of $\underset{\sim}{B}_o$ so that morphologically $\underset{\sim}{B}$ and $\underset{\sim}{B}_o$ are almost identical.

Material moving through a magnetic field experiences a drag due to $\underset{\sim}{j} \times \underset{\sim}{B}$, where $\underset{\sim}{j}$ is induced by the relative motion $\underset{\sim}{v} \times \underset{\sim}{B}/B$. If the induced current does not modify the field significantly, then

$$\underset{\sim}{j} = \frac{\sigma}{c}\ \underset{\sim}{v} \times \underset{\sim}{B} \equiv \frac{\sigma}{c}\, v\, b \qquad 6.3,$$

and if forces other than $\underset{\sim}{j} \times \underset{\sim}{B}$ are ignored for the moment, the equation of motion is

$$\rho \frac{d\underset{\sim}{v}}{dt} = \frac{1}{c}\ (\underset{\sim}{j} \times \underset{\sim}{B}) = \frac{\sigma}{c^2}\ (\underset{\sim}{v} \times \underset{\sim}{B}) \times \underset{\sim}{B} \qquad 6.4.$$

In the presence of a magnetic field, the conductivity is a tensor with components parallel and perpendicular to the magnetic field direction and perpendicular to both the magnetic field and to the component of the electric field normal to the magnetic field direction, i.e.

$$\sigma_o = \sigma = \frac{1.4 \times 10^8\ T^{3/2}}{\ln \Lambda}\ \text{e.s.u.} \qquad 6.5,$$

$$\sigma_1 = \sigma_o\ /(1 + \omega^2\tau^2) \qquad 6.6,$$

$$\sigma_2 = \sigma_o\ \omega\tau/(1 + \omega^2\tau^2) \qquad 6.7,$$

where ω is the Larmor frequency of the electrons and τ the collision period for electrons. For typical values of the conductivity in surge material, see Appendix II. When the

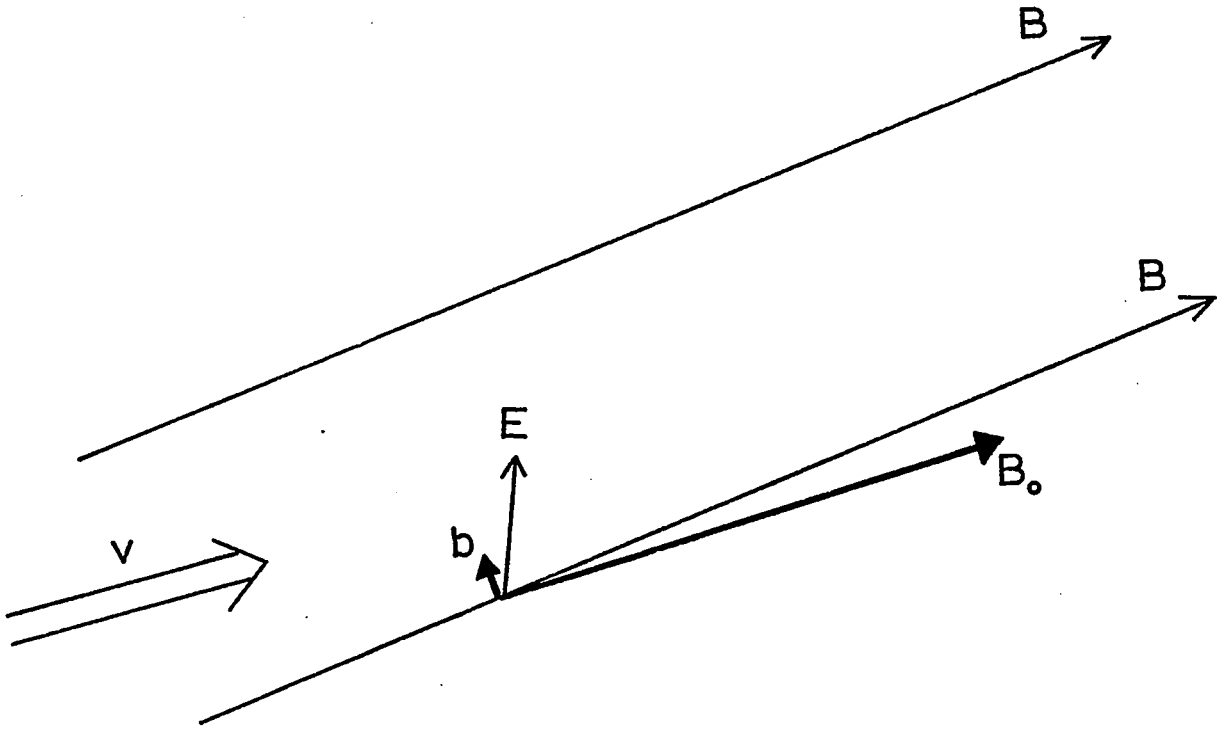

Figure 6.6. Model with braking due to the Lorentz force, $\underset{\sim}{f} = \frac{1}{c} \underset{\sim}{j} \times \underset{\sim}{b}$, arising from the surge material flowing with velocity $\underset{\sim}{v}$ in a direction normal to a small component $\underset{\sim}{b}$ of the magnetic field. The induced electric current is $\underset{\sim}{j} = \sigma_1 \underset{\sim}{E}$, where σ_1 is the conductivity of the material normal to the magnetic field $\underset{\sim}{B}$.

conductivity is anisotropic, the relative motion between the prominence material and the magnetic field is a difficult problem (Piddington, 1954).

Figure 6.6 depicts a possible configuration of a local field component $\underset{\sim}{b}$, responsible for the retarding force in in a surge where the dominant field configuration $\underset{\sim}{B}_0$ may be determined by photospheric sources. The σ component to be used is then mainly σ_1 because the current $\underset{\sim}{j} = \sigma_1 \underset{\sim}{E}$ will exert the net force $(\underset{\sim}{j} \times \underset{\sim}{B}) = \underset{\sim}{j} \times \underset{\sim}{b} \neq 0$, where $\underset{\sim}{E}$ is roughly normal to $\underset{\sim}{B}$. In reality the situation may be much more complex; see Ferraro and Plumpton, Magneto-Fluid Mechanics (1966), p. 206.

Equation 6.4 shows that the acting force should be proportional to the velocity of the surge material normal to $\underset{\sim}{b}$. This is the behavior shown in Figure 6.5 where the retarding force per unit mass, $|g_{eff}| - |g_0|$, is roughly proportional to the velocity; a v^2 dependence would still be consistent with Figure 6.5.

What is the value of b required to account for the observed retarding force? From eq. 6.4, one has

$$b^2 = \frac{\rho a c^2}{v \sigma_1} \qquad 6.8.$$

The electrical conductivity σ_1 perpendicular to the field B is of the order of 10^{10} e.s.u. (Appendix II), assuming a density of 10^{-12} g/cm^3 and T = 10^4 K. From Figure 6.5, with v = 100 km/s and a = 4 x 10^4 cm/s^2, $b \approx 0.01$ G. This value gives to the field an unnoticeable twist

amounting to a fraction of the field strength due to the photospheric sources which supply many tens of gauss up to 50 000 km above sunspot regions. From the point of view of the magnetic field configuration in the corona at the location of the surge, the current-free approximation remains valid and a most useful tool. When one considers the dynamics of a surge in detail, small non force-free effects may no longer be negligible because of the large ratio $(B^2/8\pi)/(\frac{1}{2}\rho v^2)$. This behavior is probably characteristic of surges well locked in strong active region field with closing magnetic fieldlines. Surges and sprays occuring in open field configuration (McCabe, 1971; Kirshner and Noyes, 1971) may present an outward acceleration up to much higher levels. The nature of the magnetic environment (ME to KE density ratio) is perhaps determinant for the dynamics of surges and sprays.

The qualitative agreement between curves of velocity vs height of surges and the predicted velocity under diamagnetic acceleration calculated by Livshits and Pikel'ner (1964) is fair; compare Figure 1.4 with Figures 6.2 and 6.7. The observations bring support to the mechanism of the 'melon-seed' effect. Still better data points along the fast ascending phase should be obtained; a combination of good spectra and current-free fieldline calculations providing the geometry is the most promising approach for that critical section of the velocity curve.

Ejection B in MW 18511, for example, behaves very much

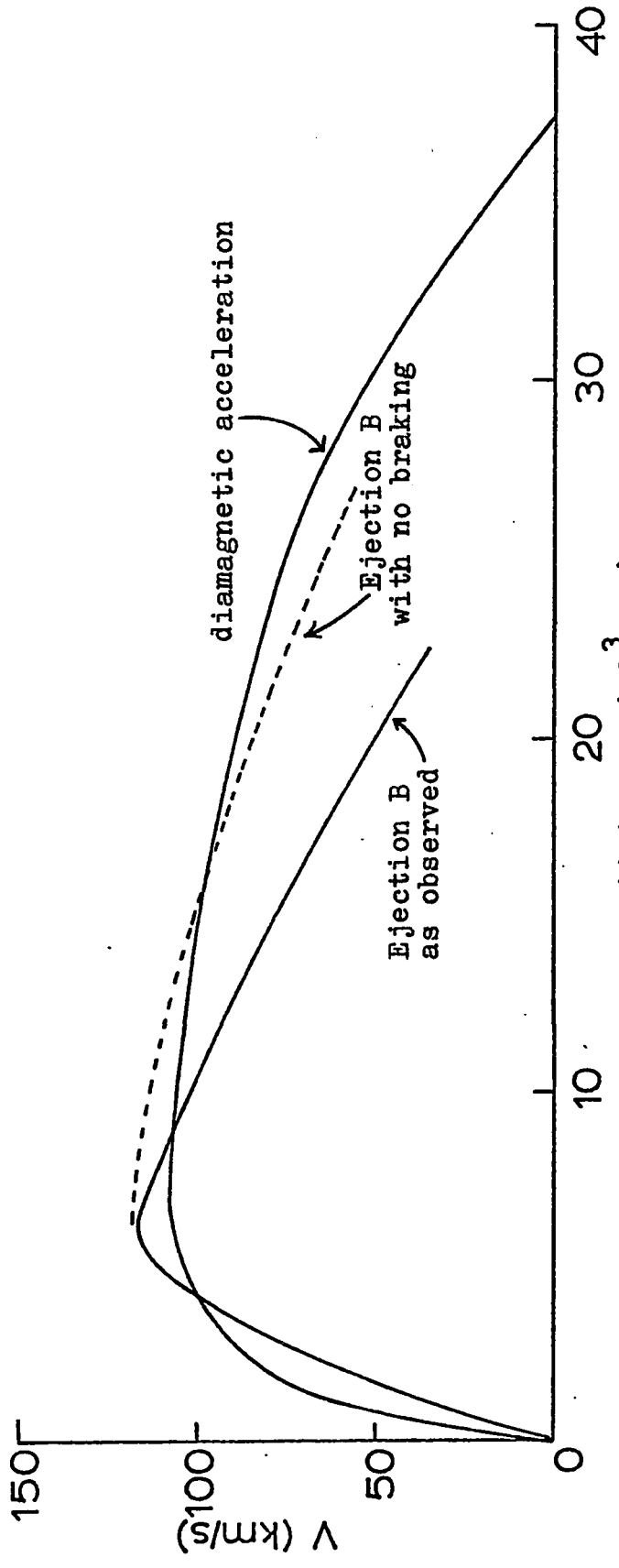

Figure 6.7. Comparison between diamagnetic acceleration (isotropic expansion, $n_o = 3 \times 10^{15}$ cm^{-3}; bottom curve in Figure 4.4b) and velocity vs height of ejection B in MW 18511 (Figure 6.2b). Differences between the observed and predicted curves at less than 10 000 km high, are meaningless because of the uncertainties in the observed curve of ejection B.

like the bottom curve of Figure 1.4 b (diamagnetic acceleration) under the assumption of isotropic expansion and $n_o = 3 \times 10^{15}$ cm^{-3} as shown in Figure 6.7; obviously, one needs to neglect the braking which is unaccounted in Livshits and Pikel'ner computations. The diamagnetic ejection model could possibly reproduce all ejection velocities by slightly varying conditions such as the initial density, the expansion law and by including a braking force.

Six successive bursts of surges were observed in MW 18511 between 1503-1715 UT. Of these, I have velocity curves for the 2 nd (A) and 3rd (B) ejections. The first ejection, already in progress, was seen as a fully developed arch, revealing the much higher initial kinetic energy of the surges compared to A and B, allowing it to escape from the magnetic potential well of the parent sunspot. Figure 6.2 also reveals that ejection A (2nd) was more energetic than ejection B (3rd); therefore, in the case of MW 18511, the successive bursts of surges are correspondingly weaker. If the ejection mechanism is diamagnetic acceleration which depends on the intensity of the magnetic gradient, the weakening of surge kinetic energy with time may reflect the weakening with time of the local magnetic field gradient.

CHAPTER VII

INTERPRETATION AND CONCLUSIONS

7.1 A PHENOMENOLOGICAL MODEL FOR SOLAR SURGES

The occurence of surges in sunspot light bridges and within a few arcsec of edges of a pore or of the penumbra-undisturbed photosphere boundary implies that a strong field (>1000 G) and/or a steep gradient is necessary for surges to occur. If associated with any detectable magnetic feature, surges are characterized by the presence of an evolving satellite polarity surrounded by flux of opposite polarity. The presence of a satellite is not sufficient; change in the surface flux is required in the form of evolving magnetic features. Evidence from the events taking place in regions MW 18235, 18468, 18511, 18538 and 18594 indicates that surge activity is favored in regions where the magnetic flux of a satellite polarity changes significantly over a period shorter than a day; this local flux increase, if occuring near low strength poles, may be paralleled by the weakening of the opposite sign polarity (MW 18468). Because the relevant magnetic flux changes are small, they probably can be detected only if the ratio $\Delta F/F$ is significant, i.e. in relatively small flux regions like satellites. The common absence

of strong opposite polarity at the origin of surges implies that their production does not require a high concentration of satellite flux but only enough magnetic 'fuel' to supply the surge kinetic and radiative energy. In order to collimate the flow and to squeeze out the energetic material, a pre-existent strong field is the needed matrix. After the occurrence of a surge, one may notice a simplification of the boundary (neutral line) between the two regions of opposite polarity: MW 18235, MW 18468 and MW 18594 (23 Oct. 1971). This apparent stabilization is not general. Because surge activity is an indicator of emerging flux, the resulting configuration may end up being more complicated than before, e.g. MW 18594 on 19-20 Oct. 1971.

A relationship between the occurrence of surge and evolving sunspot patterns was also found by Martres and Soru-Escaut (1971) who studied events similar to the surges described in this dissertation; however, they found these ejections to be seldom associated with flare occurence. This seems to contradict my finding that every single surge followed the evolution of an Ellerman bomb at its base. The observations of Martres and Soru-Escaut are affected by low resolution; most bomb brightenings show best as tiny points away from the Hα core. If the chromospheric features identified by Martres and Soru-Escaut are small surges identical to those I observed at high resolution, then the relationship between the occurrence of surges and the birth or further development of an active center

is confirmed. In summary, the presence of surges appears to be related to changes in the photospheric magnetic field distribution at sunspot locations.

As new flux is brought to the surface by buoyancy, annihilation and reconnection probably occur. Annihilation at the neutral point can heat the gas through joule heating; this may be the bomb flash. Perhaps a mechanism related to the reconnection of fieldlines or to a pressure gradient accelerates the heated material into a surge. The whole process appears to be similar to the rocket nozzle (Figure 7.1). The bomb acts as the seat of highly random motion of hot plasma. Close to the top of the chromosphere, the motion is converted into directed flow. The dominant surrounding field provides the containing force and perhaps the varying cross-section for the flow to expand and accelerate.

The lesson taught by region MW 18522 which produced the flare spray of 3 Aug. 1971, is that one should be very careful not to overinterpret or to rely heavily upon present longitudinal magnetic field data. The dynamics of spectacular phenomena must be determined by the evolution of very small scale magnetic features where the importance of dissipative processes is far from negligible. The dissipation of a magnetic field is described by the dissipative term of the MHD induction equation

$$\frac{\partial B}{\partial t} = +\eta \nabla^2 B \qquad 7.1,$$

which is a diffusion equation, with the magnetic diffusivity

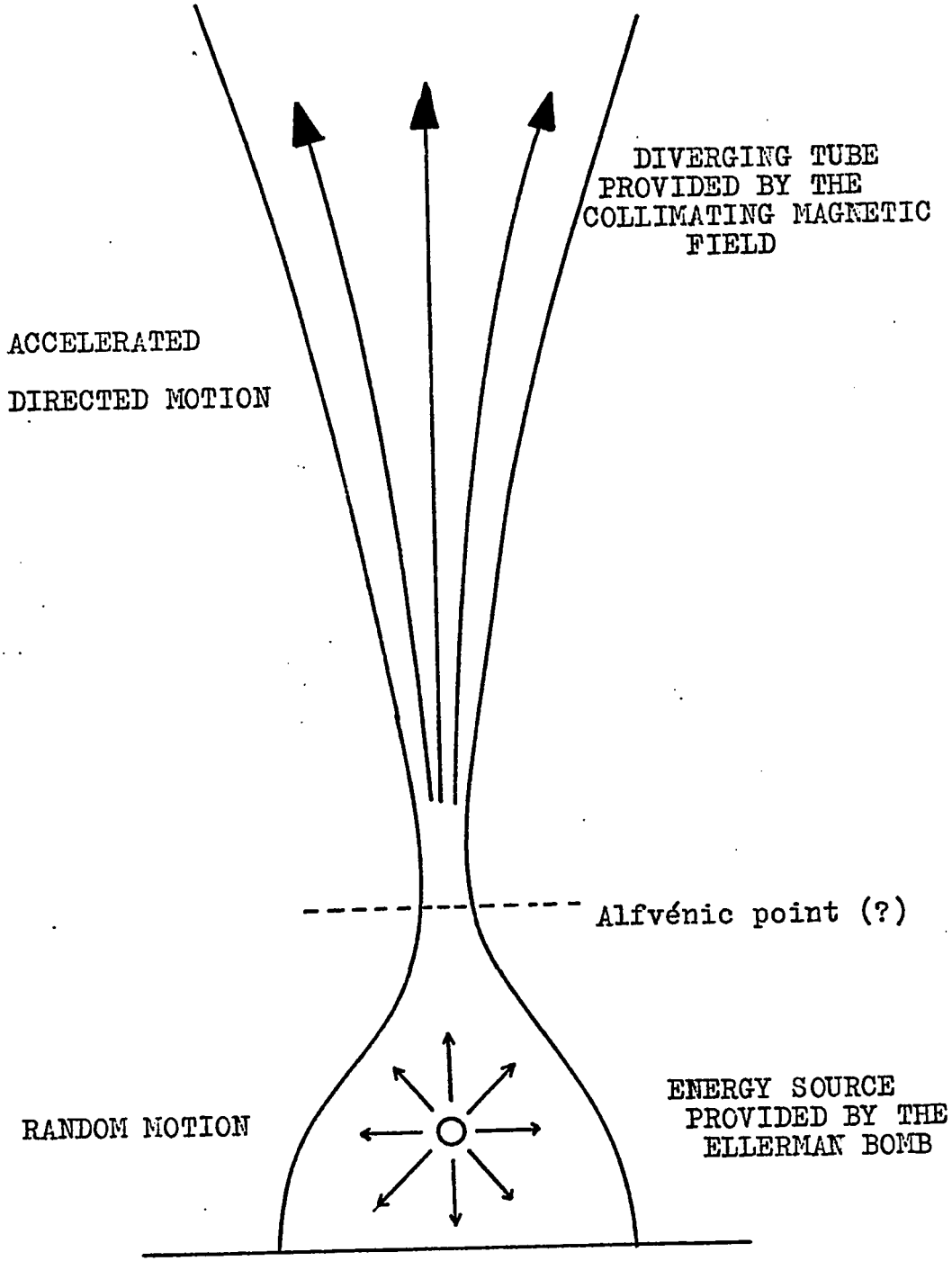

Figure 7.1. Phenomenological model of surges using the analogy of the rocket nozzle.

$\eta = c^2/(4\pi\sigma)$. From dimensional analysis, one sees that η has the dimensions of (L^2/T) where L is a length comparable with the e-folding length of the field and T is the characteristic relaxation time. Thus we may set

$$T = \frac{4\pi\sigma}{c^2} L^2 \qquad 7.2.$$

The rate of dissipation follows a L^{-2} law; thence it is very likely important at small scales. For example, changes in the sunspot configuration of an active center occur in a time of the order of a few days ($\sim 10^6$ sec). If one applies the diffusion equation to small features of the order of 100 km in size, i.e. 10^3 times smaller than sunspots, the characteristic relaxation time becomes of the order of 1 second; this allows a much faster rate of energy dissipation.

Activity along light bridges in spots is apparently associated with small features. This view is strengthened if we accept the presence of bombs as evidence for small scale opposite polarity features. Magnetic buoyancy forces could bring up some flux right through the sunspot at a weak resistance point such as a light bridge. The emergence of magnetic flux at the surface of the sun is explained by the mechanism of magnetic buoyancy proposed by Parker (1955); an horizontal magnetic flux tube in an electrically conducting atmosphere is buoyant and tends to rise. The magnetic buoyancy force is proportional to B_i^2 (B_i is the flux tube internal field) and is maximum when B_e, the external field, is the smallest. This explains

why emergence of secondary flux ropes (possibly associated with satellite polarities) may occur at weak points in the active center magnetic field, such as a region of missing penumbral filament or light bridges where I observe much bomb and surge activity apparently related to emerging flux. Recall that Beckers and Schröter (1969) found field intensities to be 300 G weaker in light bridges than in the surrounding penumbra.

7.2 PROPOSED MECHANISM

7.2.1 SUMMARY OF CRITICAL OBSERVATIONAL ASPECTS

(1) Except for three uncertain cases (beginning of surges not observed and one case where dark material originates some 10" off the nearest bomb with apparently no connection with it), some 180 surges ranging in size between 3"-200" are anchored to Ellerman bombs or to bomb-type brightenings ranging in size between a fraction of an arcsec and 5 arcsec.

(2) The short lifetime of Ellerman bombs (~12 min), in which 10^{26}-10^{27} ergs of thermal energy is liberated, necessitates a mechanism with sudden energy release. In the well documented homologous bomb-surges of 23 Oct. 1971, the thermal energy of the bombs, the kinetic energy of the surges and the energy available through changing magnetic flux are of the same order of magnitude, 5×10^{27} ergs.

(3) Surges appear within 5-10 min after the bomb starts.

(4) Thirty-four sets of observations in a region near the limb gave a significant positive correlation between

the size of the ejection and the size times the lifetime of its associated Ellerman bomb.

(5) Surges and their associated bombs originate within 7" of the boundaries of strong magnetic fields. The compact nature of Ellerman bombs reflects the work of a containing force, probably a suitable magnetic configuration.

(6) In four cases, magnetic flux as revealed by the intensity and size of magnetic contours and sunspot patterns underlying the activity, changes preceding and during the time of the bomb-surge event. The flux change rate averaged about $1 - 3 \times 10^{15}$ Mx/s in three cases.

(7) This changing flux occured at the location of satellite magnetic polarities; the satellite represents a region of roughly 10" having a polarity opposite to the dominant surrounding field. Because of the low resolution of the magnetograph, polarity reversals may be considerably stronger and of much smaller size. The magnetic field configuration is that of a neutral-X (or hyperbolic null) point or line with evolving magnetic flux locally (Figures 1.1 and 5.24). The mere existence of a satellite is not sufficient; the satellite must evolve!

(8) Sufficient non-force-free effects act on the moving surge to affect its dynamics; on the other hand, the field morphology does not deviate much from a current-free configuration because the magnetic energy density remains many times greater than the kinetic energy density of the surge for the five events I studied.

(9) Velocity curves of four surges with well-known geometry show an initial accelerating phase up to 10 000 - 30 000 km above the surface, followed by a deceleration phase and return. The deceleration is faster than if gravity alone is acting; during the falling back phase, the surge velocity is less than free-fall.

The similarity in the development and structure of bomb-surge events of all sizes suggests that a single mechanism is responsible for the phenomenon. The major drawback complicating the generalization of large surge features to smaller events, arises from the poor resolution of magnetic data; magnetic structures at the root of most importance 1 and S surges remain generally unresolved. I will assume that bomb activity is a signature of emerging flux opposite to that already present with annihilation and realignment of magnetic field going on. This is in part justified by the observations of section 5.1. The model must then include the following features:

(i) Evolving magnetic satellite flux imbedded in strong opposite sign field whose configuration acts as a collimating and possibly accelerating force;

(ii) onset of a plasma or MHD instability with the impulsive release of energy in a time of a few tens of seconds;

(iii) the Ellerman bomb rooting the surge must be an integral part of the phenomenon.

7.2.2 SELECTION OF A MECHANISM

Two basic approaches are possible and are briefly discussed in the following.

7.2.2.1 MODEL I: PASSIVE MAGNETIC FIELD

The energy is stored in non-magnetic forms such as excess gas pressure (Carmichael, 1964; Sturrock, 1968), or pressure of accelerated protons trapped in a closed magnetic field (Elliot, 1969). An instability of some sort arises and the energy is released through the rupture of the field. This approach suffers from a crucial deficiency: there is no observational evidence for accumulation of the energy before the Ellerman bomb or the flare.

7.2.2.2 MODEL II: MAGNETIC ENERGIZATION

The energy is extracted from the electromagnetic energy reservoir through mechanisms converting magnetic energy into thermal energy and mass motion. The energy comes from the excess above a purely potential magnetic energy. Two magnetic configurations can produce such an excess:

A. Because

$$B^2/8\pi \gg n\,kT \qquad \text{and} \qquad B^2/8\pi \gg \tfrac{1}{2}\rho v^2 \qquad 7.3$$

in the chromosphere and low corona, we have $(\underset{\sim}{\nabla} \times \underset{\sim}{B}) \times \underset{\sim}{B} = 0$ and the excess energy may be contained in one (Alfvén and Carlqvist, 1967) or two (Gold and Hoyle, 1960) isolated force-free twisted tubes of magnetic flux. However, these configuration were shown to be unstable from the beginning (Syrovatsky, 1969a).

B. A more successful approach uses the excess energy related with the appearance of strong currents in a plasma embedded in the potential magnetic field (Syrovatsky 1966, 1969b, 1970). If equations 7.3 are fulfilled in the genesis of such a region, it is natural to connect the deformation of the field with changes in its sources, like protruding new magnetic flux such as evolving satellite polarities. This is the approach which is supported observationally by the best documented bomb-surge events studied in section 5.2. The coming sections summarize the main aspects of the dynamic dissipation of magnetic energy in the vicinity of a neutral line as proposed by Syrovatsky (1966, 1969b, 1970).

7.2.3 FORMATION OF A CURRENT SHEET

If neutral points (see section 1.3.2) are present in the initial potential magnetic field as suggested by the observations reported in Table XIII and by Rust (1968), Syrovatsky's mechanism leads to the formation of current sheets *. Literature is abundant for explaining the appearance and behavior of current sheets: Giovanelli 1946, 1947, 1948; Sweet, 1958; Dungey, 1958; Petschek, 1964; Syrovatsky, 1966, 1969a, b, 1970; Baum, 1971; Stevenson, 1971, 1972.

* Current sheet formation at hyperbolic nulls has been considered for flare mechanisms by connecting the flare with a strong current near the neutral line of the magnetic field. Because of less stringent requirements, it seems that it is even more applicable to the bomb-surge phenomenon.

The originality of Syrovatsky's approach (Syrovatsky 1966, 1969b, 1970) is to study numerically the energy dissipation and the mass motions at a neutral line above an evolving polarity reversal. The field responsible for the polarity reversal emerges as a bipolar feature; one polarity mixes with the identical parent polarity while the opposite forms the reversal. Syrovatsky represents the magnetic field configuration near a neutral line (assumed to be a straight line directed along the z axis going through the neutral point in Figure 1.1) by a vector potential which is also function of time.

Evolving satellite polarities correspond to a change of the sources of the magnetic field which produces a change in the vector potential propagating to the neutral line in the form of a wave; this wave propagates with the Alfvén velocity and rearranges the field in conformity with a new value of the potential (Figure 7.2). A uniform electric field arises in the vicinity of the neutral line; it produces a drift motion of plasma outside the neutral line and strong electric currents near this line. In a few seconds, the disturbance reaches the neutral line and creation of a current sheet follows (Sweet, 1958; Dungey, 1958; Syrovatsky 1966, 1969). The flow is such that the current density j, plasma density n and specific current density j/n go to infinity in a finite time.

This unstable configuration may be grasped schematically from Figure 7.3 showing the direction of the electromagnetic

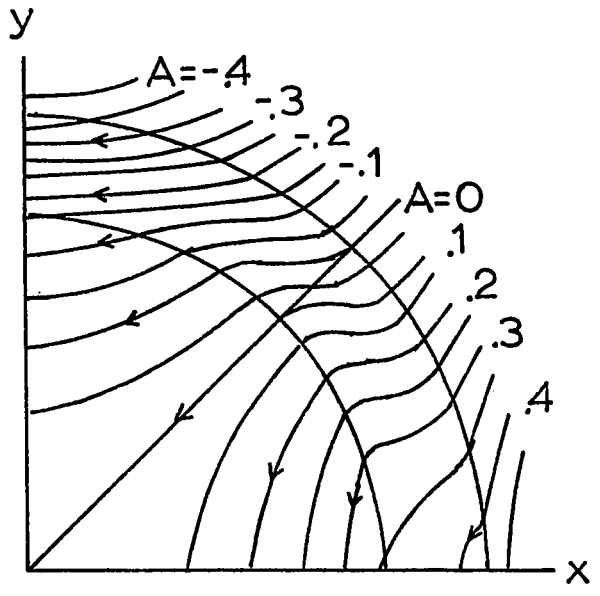

Figure 7.2. A change in the photospheric sources underlying a field configuration with a neutral line (Figure 1.1), propagates upward as a converging cylindrical wave near the neutral line (Syrovatsky, 1970). Syrovatsky assumes that the neutral line coincides with the z-axis; the picture is symmetrical with respect to x- and y-axes. The magnetic fieldlines and the forward and back wave fronts are shown. The values of the vector potential A, used by Syrovatsky, at a given magnetic line of force are given. The change in the field potential gives rise to a very strong current at the neutral line.

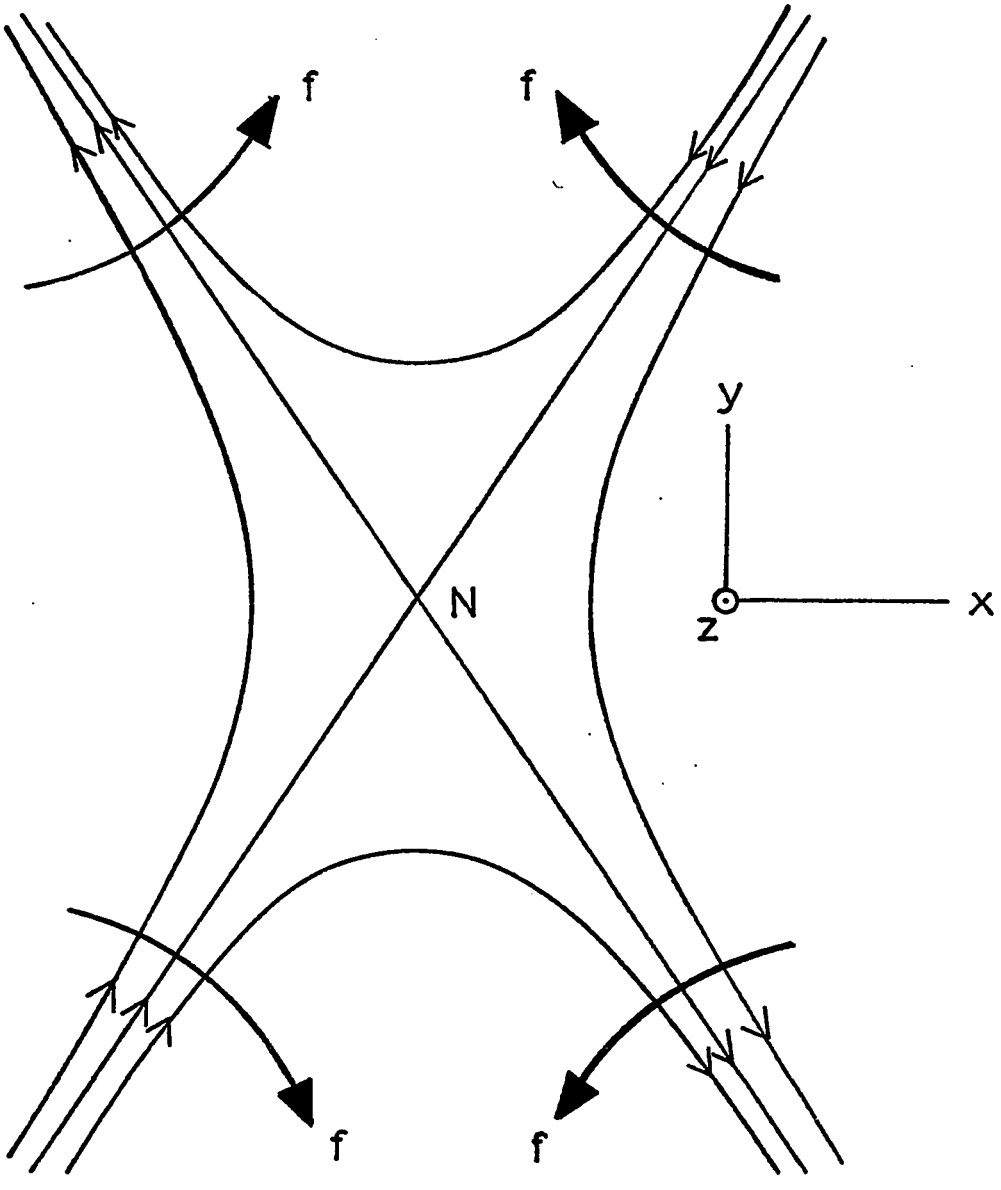

Figure 7.3. The direction of the electromagnetic force, $\underset{\sim}{f} = \frac{1}{c} \underset{\sim}{j} \times \underset{\sim}{B}$, near a neutral point N in an evolving magnetic configuration.

force at an hyperbolic null point. Electric currents are perpendicular to the paper. The gas must flow in the same direction as the acting force which stretches the gas in the vertical direction. Because of frozen-in conditions (this breaks down at the neutral point where lines of force can be regarded as broken and reconnected), the principal axes of the magnetic field (the two straight lines intersecting at N in Figure 7.3) rotate toward each other. The current density increases because $\nabla \times \underset{\sim}{B}$ increases. Therefore, a small initial current density causes motion which in turn increases the current density. The current density reaches the breakdown level where a discharge happens.

To solve the general boundary problem for a given change in the field outside the vicinity of the neutral line, one must integrate the full system of MHD equations. Results of such numerical integration by Syrovatsky (1969) are shown in Figures 7.4 and 7.5. Syrovatsky also obtains the width of the current sheet which is of the order of the diameter of the region of cumulation, i.e. only a few hundred km. In a region of this radius near the neutral line, the magnetic field is nearly uniform with a strength of a few hundred gauss and its sign changes abruptly inside the current sheet. Applying the relations given by Syrovatsky (1970) to the bomb-surge activity in MW 18594, one obtains that the surplus of magnetic energy over the energy of the initial potential field ranges between 10^{26}-10^{28} ergs, depending the parameters used; this is

Figure 7.4. Example of numerical computations of MHD flow. The values of the vector potential A, used by Syrovatsky (1970), at a given magnetic line of force are shown near the circumference. The regions of compression and of rarefaction of plasma are shown by double and single hatching respectively; for comments on the presence of a rarefaction zone, see Sweet (1969).

Figure 7.5. The behavior of the plasma at a neutral line as implied by Figure 7.4 is shown here in more detail. A current sheet develops at the place of the initial neutral line (Figure 1.1) following changes in the field sources at the photospheric level (after Syrovatsky, 1970). The arrows show the direction of the plasma flow initiated by the interaction between the strong current and the magnetic field. Double hatching denotes the predicted location of the high density plasma; y_c and $f^{\frac{1}{2}}$ are the thickness and the width of the sheet and are of the order of 10^3 km and 1 m respectively depending on the physical conditions used in the model.

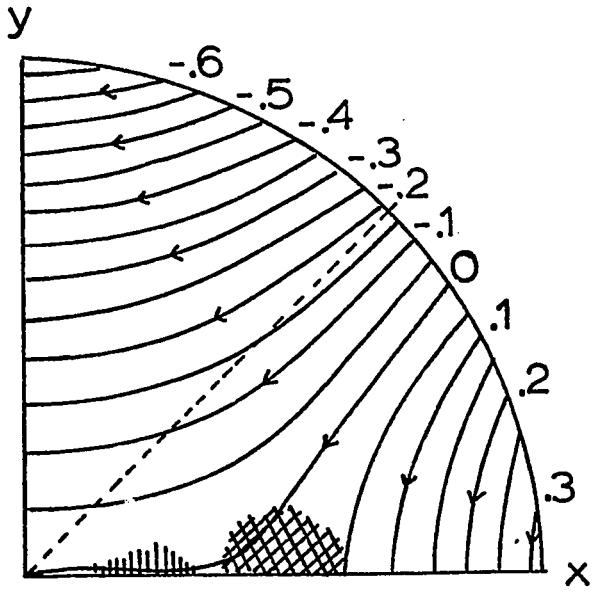
y
-.6
-.5
-.4
-.3
-.2
-.1
0
.1
.2
.3
x

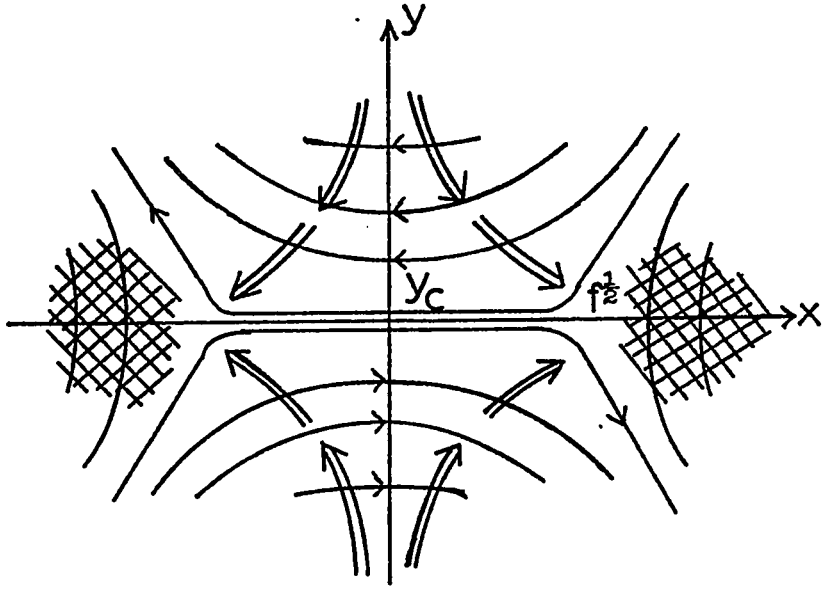
y
y_c
$f^{\frac{1}{2}}$
x

consistent with the values quoted in section 5.5.

The existence of strong plasma turbulence in the current sheet (Syrovatsky 1966, 1969 a, b, 1970; Friedman and Hamberger, 1969) facilitates the rapid heating of the plasma. This could explain the many extreme spectroscopic properties of Ellerman bombs. The core of bombs is probably very hot (10^6 K) as predicted by theory and suggested by some possible observed emission of soft X-rays (Teske, 1971). Many Ellerman bombs observed near the limb reveal a very thin hair-shaped core 2-3 arcsec long and about ½-1 arcsec wide; one wonders if those might not constitute the cooler envelopes of discharges at a neutral line. Thermal conductivity along magnetic lines of force can heat adjacent cooler regions giving rise to line emission. It would explain the crowding of Hα emission along the neutral lines delineating the satellite polarity. Indeed I observed Hα brightenings at the points where lines of force connect to the surface in the satellite of MW 18594.

Figure 7.6 shows the numerical calculations of Stevenson (1972) illustrating the lateral steepening of the pressure profile in a region of hyperbolic null as time progresses. The isobaric contours are consistent with the evolving shape of the fast growing phase of Ellerman bombs, before surge material erupts from the bomb. From the analysis of line asymmetries in a time sequence of spectra of a few Ellerman bombs, Severny (1968) suggested the presence of an initial expansion phase at 200 km/s; after a few minutes

Figure 7.6. Numerical calculations by Stevenson (1972) showing the steepening magnetic (a) and gas (b) pressure profile as time increases. The abscissa is the distance from the hyperbolic null point in arbitrary units; ten units is the distance to the boundary of the numerical model.

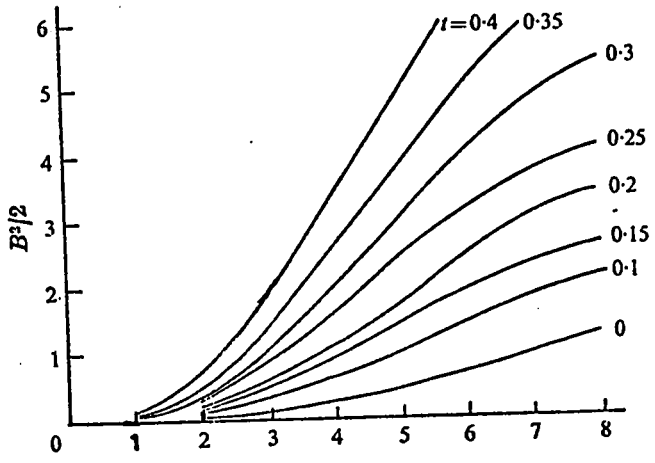
$B^2/2$
t=0·4
0·35
0·3
0·25
0·2
0·15
0·1
0
0
1
2
3
4
5
6
7
8

a

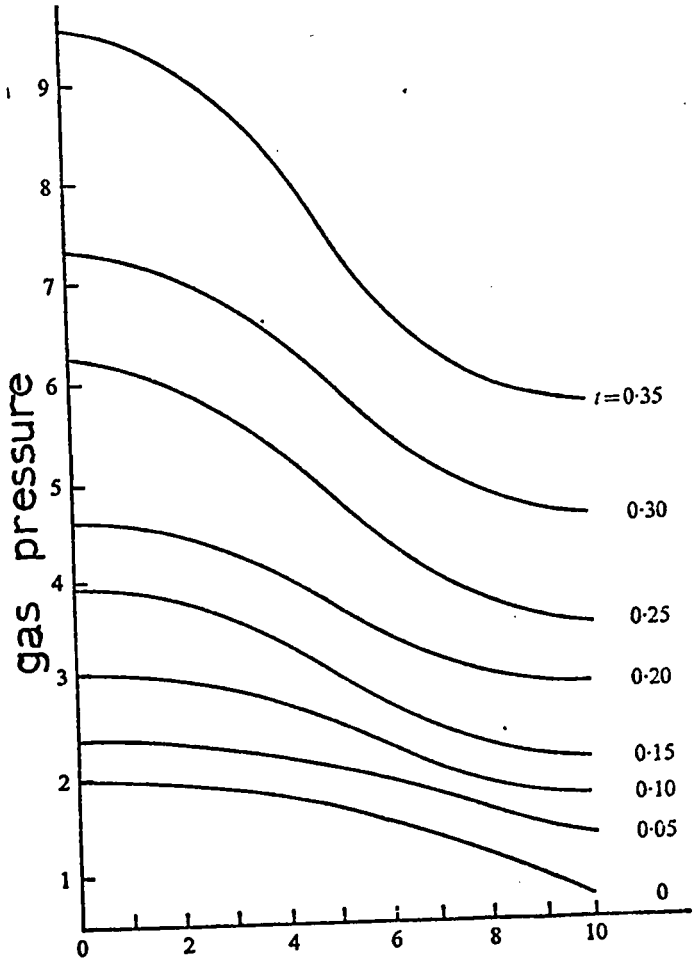
gas pressure
t=0·35
0·30
0·25
0·20
0·15
0·10
0·05
0
0
2
4
6
8
10
1
2
3
4
5
6
7
8
9

b

the asymmetry shifts to the red wing, indicating a motion reversal, as if the bomb 'deflated'.

In brief, theories of the development of current sheets at a neutral point above an evolving polarity reversal provide figures of the right order of magnitude and explain qualitatively the sudden energy release, the positional and morphological evolution of the Ellerman bombs or bomb-type brightenings in the low chromosphere associated with surge producing regions.

7.2.4 PLASMA FLOW NEAR THE MAGNETIC NEUTRAL LINE

Syrovatsky's (1966, 1969a, b, 1970) and Stevenson's (1971, 1972) numerical work produce near the current sheet steep gradients of the magnetic field, plasma density and velocity as well as intermittent areas of plasma condensation and rarefaction. Syrovatsky has investigated a case of emerging flux in the form of a bipolar group in an inhomogeneous field. Figure 7.5 depicted the situation and the properties of the plasma flow near the zero line; from this, one can infer that material will appear to emerge near the top of the bomb to flow downward as well as outward (Figure 7.7). The outward flow is the surge. The downward flow remains hard to identify observationally; its material probably remains hot when compressed by the field and mixes with the bomb emission; it could be in part responsible for the red asymmetry of the later phase of Ellerman bombs. Otherwise, one could visualize the field acting as a container of the hot gas, a kind of magnetic

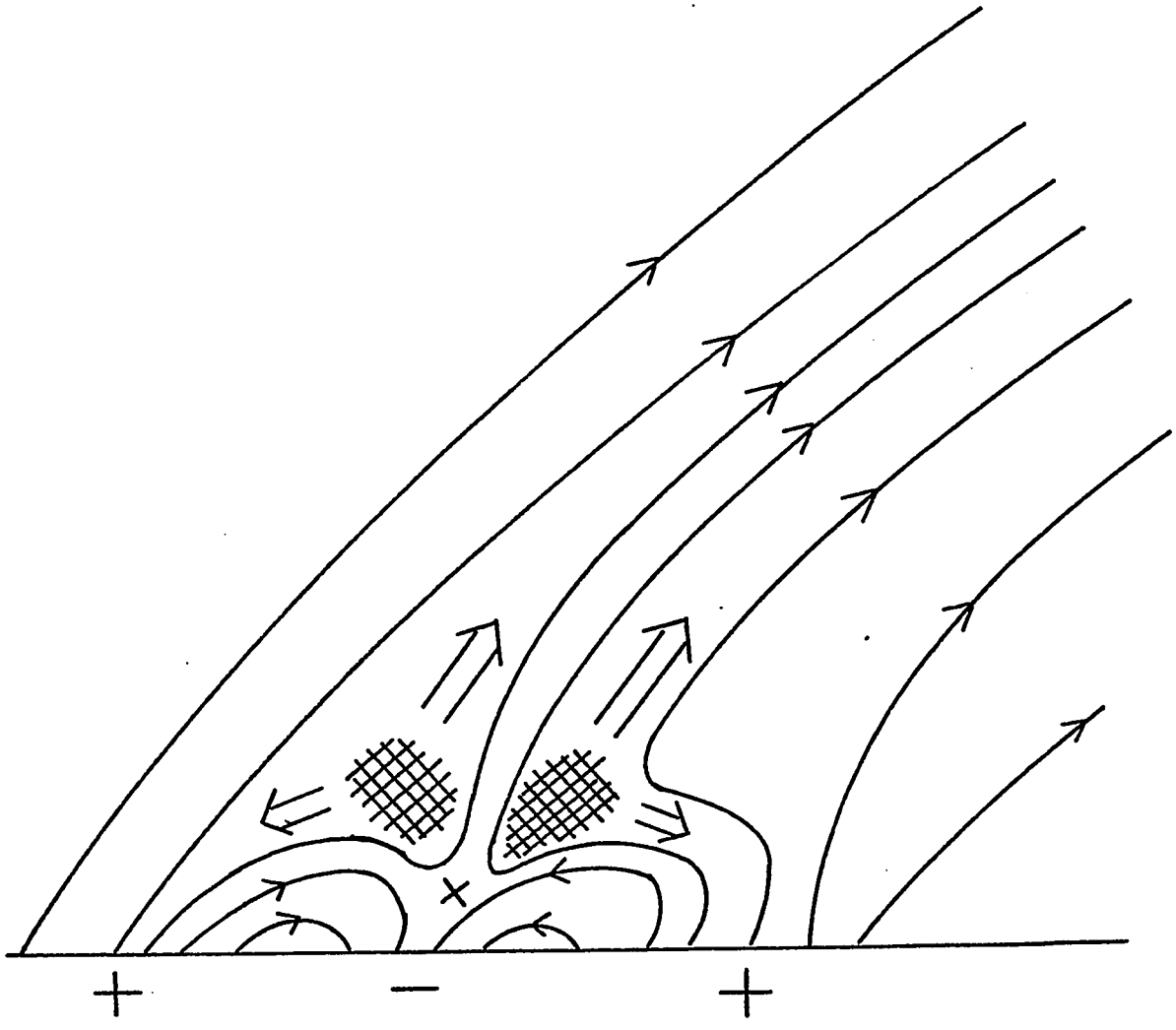

Figure 7.7. Development of a plasma flow at the location of an evolving satellite spot as implied by Syrovatsky's numerical calculations. The large arrows show the direction of the ejected material. One expects most of the flow to move upward instead of downward because of the favorable magnetic gradient.

trench, and the pressure becoming so great to rupture the field at the weaker top; the gas could burst out along the collimating external field as implied by Stevenson's work.

After the motion of the plasma flow has been initiated by heating at the current sheet, observations require a mechanism of acceleration which provides strong momentum gain in the collimating field of the parent polarity to account for the observed increase in velocity with height. Curves presented in Chapter VI best support the mechanism of diamagnetic ejection proposed by Livshits and Pikel'ner (1964), and included in spicule models (Uchida, 1969; Pikel'ner, 1969). These were described in some detail in Chapter I. Let us recall that Stevenson (1972) could not reproduce the Petschek type of flow out of the neutral point region through recession of reconnecting fieldlines; if this proves correct, acceleration by 'sling-shot' effect of relaxing reconnected fieldlines would not be dominant. Diamagnetic acceleration requires a strong magnetic gradient which is observed; it also needs a very hot initial condensation which is provided by intense heating in the associated current sheet possibly responsible for the associated bomb.

7.3 FUTURE INVESTIGATIONS

(1) Investigate in detail the evolution of Ellerman bomb and surge base fine structures and compare them to detailed high resolution magnetic maps.

(2) Determine the electron density in surges.

(3) Establish the correlation between the energy of the associated Ellerman bomb, surge and obtain more values and rate of change of satellite magnetic flux.

(4) Establish the correlation of evolving satellite polarity position in the active center with their production of bomb-surge events.

(5) Obtain time sequences of spectroscopic observations of Ellerman bombs at intervals of 10 sec or less.

(6) Obtain surge velocity curves in the first 5 000 km above its associated bomb.

(7) Establish the correlation of the explosive phase of Ellerman bombs with soft X-ray emission and Type III radio events.

(8) Investigate the time and spatial behavior of surges in the EUV and X-ray region as well as their optical counterpart.

(9) Compute theoretical curves of velocity vs height assuming diamagnetic ejection plus a braking force directed against the motion, to match the observed velocity vs height curves of the surges of Chapter VI.

(10) Study the velocities in the photosphere that accompany the emergence of satellite spots. Determine whether material motions compress the fields or push opposite polarities together.

APPENDIX I

Magnetic classification of sunspots *

Main class	Finer subdivision		Percentage occurence
	Symbol	Description	
Unipolar	α	Distribution of faculae symmetrical around spot	15
	αp	Spot followed by faculae	28
	αf	Spot preceded by faculae	3
Bipolar	β	Preceding and following spots of approximately equal area	11
	βp	Preceding spot is the principal member of group	29
	βf	Following spot is the principal member of group	10
	$\beta\gamma$	Bipolar characteristics present, but dividing line between polarities not well marked	3
Complex	γ	Polarities irregularly distributed	1

* after Tandberg-Hanssen, 1967

APPENDIX II

Electrical conductivities in surges

Parameter	i	ii	iii
T	10^4 K	10^4 K	10^4 K
n	10^{11} cm^{-3}	10^{12} cm^{-3}	10^{12} cm^{-3}
B	10 G	10 G	100 G
σ_0	10^{13} esu	10^{13} esu	10^{13} esu
σ_1	6×10^9 esu	7×10^{11} esu	8×10^9 esu
σ_2	2.5×10^{11} esu	3×10^{12} esu	3×10^{11} esu

APPENDIX III

CATALOG OF OBSERVATIONS [a]

Date 1971	Time UT	Region SPO	Region MT WILSON	Position	Comments [b]
10 June	1424-1507	2763		W50 N00	A
11 June	1547-1601	2775		E15 N15	A
12 June	1417-1800	2775		E02 N15	A, 16 mm, AFS
13 June	1323-1615	2775		W10 N15	A, very good AFS
17 June	1322-1542	2784		W45 N12	A, small surges
18 June	1347-1559	2782		W10 S08	A
19 June	1446-1601			E50 S10	A, quiescent prom.
		2782		W23 S08	A
20 June	1517-1556	2785		W58 N10	A, very poor seeing
28 June	1606-1812	2792-2795	18472-73-76	E58 S14	A, 16 mm
29 June	1518-1549	2795	18476-18479	E54 S14	A, EB's & surges
	1550-1638	2789	18468	W13 N15	A, surge, 16 mm, AFS
	1640-1739	2795	18476-18479	E54 S14	A
30 June	1553-1702	2789	18468	W27 N15	A, AFS, small surges
		2795	18476-18479	E40 S14	A

01 July	1521- ?	2796	18476-18479	E27 S12	A, very poor seeing
10 July	1505-1724	2799			A, poor seeing
		2795 ?			A, poor seeing
		2799			A, poor seeing, AFS
		2801	18489	E77 N15	A, poor seeing
11 July	1504-1651	2799		W04 S07	A, subflare
	1654-1715	2801	18489	E65 N15	A
	1715-1759	2802	18488	E90 N00	A, surge
12 July	1511-1706	2802	18488		A, poor seeing
		2800			A, poor seeing
		2799			A, poor seeing
		2801	18489		A, poor seeing
13 July	1447-1715	2802	18488		A, poor seeing
		2801	18489		A, poor seeing
14 July	1504-1610	2802	18488	E52 N04	A
17 July	1535-1613	2802	18488	E12 N05	A, manual run
		2804	18491	E30 S05	A, manual run
		2801	18489	E24 N10	A, manual run

25 July	1503-1623	2820	18511	E62 S15	B, 16 mm, bombs & surges
	1623-1638	2811		W55 N12	B
	1638-1645	2816	18502 ?	W05 N12	B
	1645-1715	2820	18511	E62 S15	B, bombs & surges
30 July	1404-1505	2820	18511	W03 S13	A
	1505-1510	2823-2826	18514-18515	E40 N08	A
31 July	1258-1512	2820	18511	W18 S13	A, surges and bombs
	1528-1531	2829	18520	E60 S25	A, surges
	1655-1800	2829	18520	E60 S25	A
1 Aug.	1321-1330	2823	18514	E16 N08	A
	1330-1504	2820	18511	W25 S12	A
	1504-1530	2829	18520	E45 S25	A
	1531-1601	2820	18511	W25 S13	A
2 Aug.	1305-1445	2829	18520	E31 S25	A
	1448-1456	2823-2826	18514-18515	W02 N08	A
	1459-1521	2820	18511	W39 S14	A
	1522-1529	2830	18521	E55 S08	A

3 Aug.	1324-1335	2830	18521	E39 S08	A
	1337-1345	2829	18520	E20 S25	A
	1347-1353	2820	18511	W53 S13	A
	1355-1528	2831	18522	E77 S10	A, 16 mm, flare-sprays-surges
4 Aug.	1311-1416	2831	18522	E63 S10	A, 16 mm, surges & bombs
9 Aug.	1642-1650	2832		W23 N12	A
	1656-1659	2831	18522	E04 S10	A
	1659-1712			W40 S07	A, subflare & surge
	1713-1728	2831	18522	E04 S10	A
17 Aug.	1538-1621	2845	18538	E85 S13	A, surges, clouds
19 Aug.	1514-1723	2845	18538	E58 S13	A, bombs-surges-subflare, clouds
20 Aug.	1554-1706	2845	18538	E42 S13	A, surges & bombs
		2847	18543	E79 S06	A, surge on limb
21 Aug.	1701-1739	2845	18538	E26 S13	A
23 Aug.	1635-1742	2845	18538	E01 S12	A
	1743-1750			East limb	quiescent prom.
30 Aug.	1704-1736	2845	18538	West limb	A, surges
1 Sept.	1351-1456	2851			A
3 Oct.	1821-1830	2876	18575	E11 N11	manual run

19 Oct.	1955-2049	2886	18594	E26 N08	A, surges
20 Oct.	1418-1538	2886	18594	E17 N08	A, surges
	1916-2030	2886	18594	E15 N08	A, surges
21 Oct.	1345-1455	2886	18594	E03 N08	A, surges
22 Oct.	1431-1511	2886	18594	W10 N08	A
23 Oct.	1347-1431	2886	18594	W24 N08	A
	1900-2054	2886	18594	W24 N08	A, 16 mm, large surges and bombs in EMS
24 Oct.	1432-1520	2886	18594	W35 N08	A, small surges
26 Oct.	1416-1457	2886	18594	W50 N08	A, very poor seeing
27 Oct.	1403-1526	2886	18594	near west limb	A, surges, poor seeing

[a] All observations refer to Hα filtergrams on 35 mm SO-392 film with passband of $\frac{1}{4}$ Å.

[b] Sequences used λ= Hα-2 Å, -1 3/8, -7/8, -5/8, ±0, +5/8, +7/8, +1 3/8 is referred as A;

λ= Hα-2 Å, -7/8, -5/8, $-\frac{1}{4}$, ±0, $+\frac{1}{4}$, +5/8, +7/8 is referred as B.

'16 mm' indicates that a movie has been made from the original 35 mm film.

BIBLIOGRAPHY

Alfvén, H. and Carlqvist, P.: 1967, Solar Phys. 1, 220

Altschuler, M. D., Lilliequist, C. G. and Nakagawa, Y.: 1968, Solar Phys. 5, 366

Baum, P. J.: 1971, A Laboratory Model of Solar Flares, Ph. D. Dissertation, U of California (Riverside)

Becker, M.: 1959, Z. Astrophys. 48, 189

Beckers, J.M. and Schröter, E. H.: 1969, Solar Phys. 10, 384

Bruzek, A.: 1969, COSPAR Symp. on Solar Flares and Space Research, North-Holland Pub. Co., p. 61

_____: 1972, Solar Phys. 26, 94

_____ and Kuperus, M.: 1972, Solar Phys. 24, 3

Carlqvist, P.: 1968, in Y. Ohman (ed.) 'Mass Motions in Solar Flares and Related Phenomena', Nobel Symp. 9, 193

_____: 1969, Solar Phys. 7, 377

Dravins, D.: 1972, Big Bear Solar Obs. preprint

Dungey, J. W.: 1958, in B. Lehnert (ed.) 'Electromagnetic Phenomena in Cosmical Physics', IAU Symp. 6 135

Dunn, R. B.: 1964, Applied Optics 3, 1353

_____: 1969, Sky and Tel. 38, 368

_____: 1971a, in Seddon and Smyth (eds.) 'Automation in Optical Astrophysics', IAU Coll., p. 37

Dunn, R. B.: 1971b, The Menzel Symposium on Solar Physics, Atomic Spectra and Gaseous Nebulae, NBS Washington, p. 71

_____: 1971c, in R. Howard (ed.) 'Solar Magnetic Fields', IAU Symp. 43, 65

Ellerman, F.: 1917, Ap. J. 46, 298

Ellison, M. A.: 1942, M.N.R.A.S. 109, 3

Elliot, H.: 1969, COSPAR Symp. on Solar Flares and Space Research, North-Holland Pub. Co., p. 356

Evans, J. W.: 1949, J. Opt. Soc. Amer. 39, 229

_____: 1953, in The Sun, U of Chicago Press, p. 626

_____: 1966, in Atti del Convegno Sui Campi Magnetici Solari, Firenze (Italy)

_____: 1967, Solar Phys. 1, 157

Friedman, M. and Hamberger, S. M.: 1969, Solar Phys. 8, 104

Giovanelli, R. G.: 1946, Nature 158, 81

_____: 1947, M.N.R.A.S., 107, 338

_____: 1948, M.N.R.A.S., 108, 163

_____ and McCabe, M. K.: 1958, Austr. J. of Phys. 11, 191

Gold, T. and Hoyle, F.: 1960, M.N.R.A.S. 120, 89

Gopasyuk, S. I.: 1964, Izv. Krymsk. Astrofiz. Obs. 33, 100

_____, Ogir, M. B. and Tsap, T. T.: 1963, Izv. Krymsk. Astrofiz. Obs. 30, 148

Haase, M. Gaenswein, P.: 1967, Zeiss Information, #65, p. 75

Harvey, J. W.: 1969, Magnetic Fields Associated with Active Region Prominences, Ph. D. Dissertation, U of Colorado

_____ and Livingston, W.: 1969, Solar Phys. 10, 283

Howard, R. (ed.): 1971, 'Solar Magnetic Fields', IAU Symp. 43

Imshennik, V. S. and Syrovatsky, S. I.: 1967, Zh. Exper. Teoret. Fisik 52, 990

Jefferies, J. T. and Orrall, F. Q.: 1965, Ap. J. 141, 519

Kirshner, R. P. and Noyes, R. W.: 1971, Solar Phys. 20, 428

Kleczek, J. and Krivsky, L.: 1960, Nature 186, 1035

Koval, A. N.: 1964, Izv. Krymsk. Astrofiz. Obs. 32, 132

_____: 1965a, Izv. Krymsk. Astrofiz. Obs. 33, 138

_____: 1965b, Izv. Krymsk. Astrofiz. Obs. 34, 278

_____: 1967, Izv. Krymsk. Astrofiz. Obs. 37, 62

_____ and Severny, A. B.: 1970, Solar Phys. 11, 276

Lilliequist, C. G., Altschuler, M. D. and Nakagawa, Y.: 1971, Solar Phys. 20, 348

Livshits, M. A. and Pikel'ner, S. B.: 1964, Soviet AJ 8, 368

Lyot, B.: 1944, Ann. Astrophys. 7, 48

Malville, J. M.: 1962, Ap. J. 135, 834

Martres, M. J., Pick, M. and Soru-Escaut, I.: 1972, Nature Physical Sciences 236, 25

_____ and Soru-Escaut, I.: 1971, Solar Phys. 21, 137

McCabe, M. K.: 1971, Solar Phys. 19, 451

McMath, R. R., Mohler, O. C. and Dodson, H. W.: 1960, Proc. Natl. Acad. Sci. US 46, 165

Michard, R.: 1971, in R. Howard (ed.) 'Solar Magnetic Fields', IAU Symp. 43, 359

Moreton, G. E. and Severny, A. B.: 1968, Solar Phys. 3, 282

Noyes, R. W., Dupree, A. K., Huber, M. C. E., Parkinson, W., Reeves, E. M., Withbroe, G. L.: 1972, Ap. J. 178, 515

Ohman, Y. (ed.): 1968, ' Mass Motions in Solar Flares and Related Phenomena', Nobel Symp. 9

Parker, E. N.: 1955, Ap. J. 121, 491

_____: 1963, Ap. J. Suppl. 8, 177

Petschek, H. E.: 1964, AAS-NASA Symp. on 'The Physics of Solar Flares, NASA SP-50, 425

Piddington, J. H.: 1954, M.N.R.A.S. 114, 651

Pikel'ner, S. B.: 1969, Soviet AJ 13, 259

Poland, A. and Anzer, U.: 1971, Solar Phys. 19, 401

Ribes, E.: 1969, Astron. Astrophys. 2, 316

Roy, J.-R.: 1971, 'Magnetic Fields Above Active Region in the Solar Corona', M. Sc. Thesis, U of Western Ontario, 86 p.

_____: 1972, Solar Phys. 26, 418

_____: 1973, Solar Phys. in press

Rust, D.M.: 1966, 'Measurements of the Magnetic Fields in Quiescent Solar Prominences', Ph. D. Dissertation U of Colorado, 183 p.

_____: 1968, in K. O. Kiepenheuer (ed.) 'Structure and Development of Solar Active Regions', IAU Symp. 35, 77

Rust, D. M.: 1970, Ap. J. 160, 315

_____: 1972, Solar Phys. 25, 141

_____ and Roy, J.-R.: 1971, in R. Howard (ed.) 'Solar Magnetic Fields', IAU Symp. 43, 569

Schmidt, H. U.: 1964, AAS-NASA Symp. on 'The Physics of Solar Flares', NASA SP-50, p. 107

_____: 1969, COSPAR Symp. on Solar Flares and Space Research, North-Holland Pub. Co., p. 331

Severny, A. B.: 1964a, Ann. Rev. Astron. Astrophys. 2, 363

_____: 1964b, Izv. Krymsk. Astrofiz. Obs. 31, 159

_____: 1965, Astron. Zh. 42, 217

_____: 1968, in Y. Ohman (ed.) 'Mass Motions in Solar Flares and Related Phenomena, Nobel Symp. 9, 71

_____ and Koval, A. N.: 1961, Izv. Krymsk. Astrofiz. Obs. 26, 3

Stevenson, J. C.: 1971, J. Plasma Phys. 6, 125

_____: 1972, J. Plasma Phys. 7, 293

Syrovatsky, S. I.: 1966, Soviet AJ 10, 270

_____: 1967, Izv. Akad. Nauk SSSR, ser. fis. 31, 1303

_____: 1969a, Trudy Mezh. Seminare, Leningrad, p. 7

_____: 1969b, COSPAR Symp. on Solar Flares and Space Research, North-Holland Pub. Co., p. 346

Syrovatsky, S. I.: 1970, in Dyer (ed.) 'Solar Terrestrial Physics', p. 119, D. Reidel Publ. 1972

Smith, E. V. P.: 1968, in Y Ohman (ed.) 'Mass Motions in Solar Flares and Related Phenomena', Nobel Symp. 9,137

Stenflo, J.: 1971, in R. Howard (ed.) 'Solar Magnetic Fields' IAU Symp. 43, 101

_____: 1968, Acta Univ. Lund II, no 2

Sturrock, P.: 1968, in K. O. Kiepenheuer (ed.) 'Structure and Development of Solar Active Regions', IAU Symp. 35, 77

Swarup, G., Stone, P. H. and Maxwell, A.: 1960, Ap. J. 131, 725

Sweet, P.: 1958, in B. Lehnert (ed.) 'Electromagnetic Phenomena in Cosmical Physics', IAU Symp. 6, 123

_____: 1969, Ann. Rev. Astr. Astrophys. 7, 149

_____: 1971, in R. Howard (ed.) 'Solar Magnetic Fields' IAU Symp. 43, 457

Tandberg-Hanssen, E.: 1959, Ap. J. 130, 202

_____: 1963, Ap. J. 137, 26

_____: 1967, Solar Activity, Blaisdell Pub. Co., 464 p.

Teske, R. G.: 1971, Solar Phys. 21, 146

Teryaeva, M. S.: 1960, Solnechnye Dannye, no 9

Uchida, Y.: 1969, Pub. Astr. Soc. Japan 21, 128

Vorpahl, J. and Pope, T.: 1972, Solar Phys. 25, 347

Westin, H.: 1969, Solar Phys. 7, 393

Young, A. T.: 1971, Sky and Tel. 42, 139

Zvereva, A. M. and Severny, A. B.: 1970, Izv. Krymsk. Astrofiz. Obs. 41-42, 97